

PL-TR-96-2079

ATMOSPHERIC SCENE SIMULATION MODELING AND VISUALIZATION

Maureen E. Cianciolo
Mark E. Raffensberger
Eric O. Schmidt
John R. Stearns

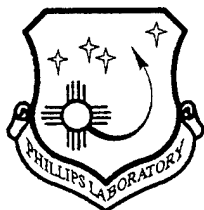
TASC
55 Walkers Brook Drive
Reading, Massachusetts 01867-3297

15 April 1996

Final Report
24 September 1993-23 March 1996

19960819 134


APPROVED FOR PUBLIC RELEASE; DISTRIBUTION UNLIMITED

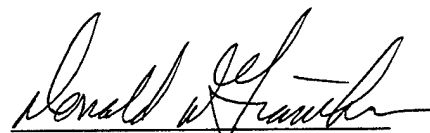


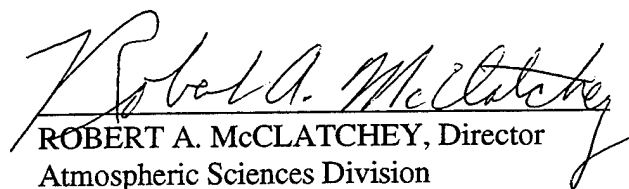
PHILLIPS LABORATORY
Directorate of Geophysics
AIR FORCE MATERIEL COMMAND
HANSCOM AFB, MA 01731-3010

DTIC QUALITY INSPECTED 1

"This technical report has been reviewed and is approved for publication"


THOMAS CAUDILL
Contract Manager


DONALD D. GRANTHAM
Branch Chief


ROBERT A. McCLATCHEY, Director
Atmospheric Sciences Division

This report has been reviewed by the ESC Public Affairs Office (PA) and is releasable to the National Technical Information Service (NTIS).

Qualified requestors may obtain additional copies from the Defense Technical Information Center (DTIC). All others should apply to the National Technical Information Service (NTIS).

If your address has changed, if you wish to be removed from the mailing list, or if this addressee is no longer employed by your organization, please notify PL/IM, 29 Randolph Road, Hanscom AFB, MA 01731-3010. This will assist us in maintaining a current mailing list.

Do not return copies of this report unless contractual obligations or notices on a specific document require that it be returned.

REPORT DOCUMENTATION PAGE

Form Approved
OMB No. 0704-0188

Public reporting burden for this collection of information is estimated to average one hour per response, including the time for reviewing instructions, searching existing data sources, gathering and maintaining the data needed, and completing and reviewing the collection of information. Send comments regarding this burden estimate or any other aspect of this collection of information, including suggestions for reducing this burden, to Washington Headquarters Services, Directorate for Information Operations and Reports, 1215 Jefferson Davis Highway, Suite 1204, Arlington, VA 22202-4302, and to the Office of Management and Budget, Paperwork Reduction Project (0704-0188), Washington, DC 20503.

1. AGENCY USE ONLY (Leave blank)		2. REPORT DATE 15 April 1996		3. REPORT TYPE AND DATES COVERED Final - 24 September 1993 - 23 March 1996	
4. TITLE AND SUBTITLE Atmospheric Scene Simulation Modeling and Visualization				5. FUNDING NUMBERS PE 62101F PR 4238 TA GS WU AD Contract F19628-93-C-0203	
6. AUTHOR(S) Maureen E. Cianciolo, Eric O. Schmidt, Mark E. Raffensberger, John R. Stearns					
7. PERFORMING ORGANIZATION NAME(S) AND ADDRESS(ES) TASC 55 Walkers Brook Drive Reading, MA 01867				8. PERFORMING ORGANIZATION REPORT NUMBER TR-07169-1	
9. SPONSORING/MONITORING AGENCY NAME(S) AND ADDRESS(ES) Phillips Laboratory 29 Randolph Road Hanscom AFB, MA 01731-3010 Contract Manager: Thomas R. Caudill/GPAA				10. SPONSORING/MONITORING AGENCY REPORT NUMBER PL-TR-96-2079	
11. SUPPLEMENTARY NOTES					
12a. DISTRIBUTION/AVAILABILITY STATEMENT Approved for public release; distribution unlimited				12b. DISTRIBUTION CODE	
13. ABSTRACT (Maximum 200 words) This report provides a review of the <i>Cloud Scene Simulation Model (CSSM)</i> , an empirical cloud model developed to support high-fidelity training and simulation applications. TASC and the U.S. Air Force Phillips Laboratory have developed the CSSM to simulate realistic high-resolution cloud and precipitation features within domains defined by larger-scale weather conditions. The current version of the cloud model is built upon the CSSM developed previously for the Smart Weapons Operability Enhancement Program (Ref. 1). It contains several key additions and enhancements to satisfy modeling and simulation requirements of the Distributed Interactive Simulation (DIS) community. The model generates four-dimensional (three spatial and time) cloud and precipitation fields using a combination of stochastic field generation techniques and a simple convection model. Internal model parameters have been tuned to fit observed cloud data.					
14. SUBJECT TERMS cloud model, rain model, modeling and simulation, distributed interactive simulation, visualization, cloud water content, atmospheric model, scene generation, orographic clouds, optical properties, radiative properties, graphical quantities, transmittance, optical depth, transparency, diffusivity, absorptivity				15. NUMBER OF PAGES 118	
				16. PRICE CODE	
17. SECURITY CLASSIFICATION OF REPORT UNCLASSIFIED	18. SECURITY CLASSIFICATION OF THIS PAGE UNCLASSIFIED	19. SECURITY CLASSIFICATION OF ABSTRACT UNCLASSIFIED	20. LIMITATION OF ABSTRACT SAR		

TABLE OF CONTENTS

	Page
1. INTRODUCTION	1
2. THE CLOUD SCENE SIMULATION MODEL	6
2.1 The Cloud Model	7
2.1.1 Motivation	7
2.1.2 Typical Scenarios	7
2.1.3 Overall Methodology	8
2.1.4 Primary Procedures	9
2.1.5 Cloud Model Results	37
2.2 The Rain Model	40
2.2.1 Overview	41
2.2.2 Development of Precipitation Rate Algorithms	41
2.2.3 In-Cloud Precipitation Rates	46
2.2.4 Surface Precipitation Rate Algorithm	50
2.2.5 Conclusions	51
2.3 Parameter Estimation and Cumulus Model Validation	52
2.3.1 Cloud Liquid Water Content Data Collection and Analysis	52
2.3.2 Parameter Estimation	66
2.3.3 Cumulus Model Validation	75
2.3.4 Conclusion	85
3. CLOUD SCENE VISUALIZATION	87
3.1 Quick-Look Cloudviewer	87
3.2 "Fast-map" for Water Clouds	89
3.2.1 Approach	89
3.2.2 Theoretical Discussion	90
3.2.3 Summary	103
3.2.4 Future Work	104
4. SUMMARY AND RECOMMENDATIONS	105
REFERENCES	109

LIST OF FIGURES

Figure		Page
1	Grid Domains Used in the CSSM	12
2	RSA Field (scaled to 8 bits)	14
3	RSA Field After Transformation to Uniform Distribution (scaled to 8 bits)	15
4	RSA Field After Thresholding Process (scaled to 8 bits)	16
5	Cloud Base Perturbation Field (scaled to 8 bits)	18
6	Cloud Top Height Field (scaled to 8 bits)	19
7	Vertical Cloud Profile Valid for Sc, Ns, and Ac Cloud Types (from Ref. 9)	21
8	Schematic Showing Variables Used to Calculate $pab_{overall}$ and pab_{local} at the Dashed Location	22
9	First Step in Cirriform Model, Horizontal Non-Isotropic Pre-Cloud Distribution (scaled to 8 bits)	25
10	Cirriform Horizontal Cloud Distribution After Fractal Perturbation (scaled to 8 bits)	26
11	One Slice through a 3-d Cirrus Cloud Field (scaled to 8 bits)	27
12	Cloud Street Scene	35
13	Schematic Showing Orographic Wave Processing Geometry	36
14	Orographic Wave Cloud Scene	38
15	Stratus Cloud Scene	39
16	Layered Cloud Scene With Cirrus Over Cloud Streets	39
17	Cumulus Cloud Scene	40
18	Cross-section of Model Output of Simulated Cumulus Cloud LWC Values. Dashed Contour Denotes Cloud Edge. Solid Contour Surrounds LWC Values Greater Than the Cutoff Value of 0.9 g/m^3 . Both Axes Are Labeled in Kilometers.	48
19	Precipitation Rates (Contoured Every 2 mm/hr Starting at 0 mm/hr) Derived from LWC Cross-section Shown in Figure 18. Both Axes are Labeled in Kilometers.	49
20	Cross-section of Model Output of Simulated Nimobstratus Cloud LWC Values. Dashed Contour Denotes Cloud Edge. Solid Contour Surrounds LWC Values Greater Than the Cutoff of 1.0 g/m^3 . Both Axes Are Labeled in Kilometers	49
21	Precipitation Rates (Contoured Every 2mm/hr Starting a 0 mm/hr) Derived from LWC Cross-section Shown in Figure 20. Both Axes are Labeled in Kilometers.	50

22	Time Series of LWC in g/m^3 (Panel A) and Autocorrelation Function (Panel B) for Observed Path E9 through Montana Cumulus Cloud	60
23	Time Series of LWC in g/m^3 (Panel A) and Autocorrelation Function (Panel B) for Observed Path I9 through South Africa Cumulus Cloud	61
24	Time Series of LWC in g/m^3 (Panel A) and Autocorrelation Function (Panel B) for Observed Path W3 through Nova Scotia Stratus Cloud	62
25	Time Series of LWC in g/m^3 (Panel A) and Autocorrelation Function (Panel B) for Observed Path Y2 through Nova Scotia Stratus Cloud	63
26	Time Series of LWC in g/m^3 (Panel A) and Autocorrelation Function (Panel B) for Simulated Path MON8 through Montana Cumulus Cloud ..	68
27	Time Series of LWC in g/m^3 (Panel A) and Autocorrelation Function (Panel B) for Simulated Path BET3 through South Africa Cumulus Cloud	69
28	Path Water Content Statistics for Montana Cumulus Clouds. Dark/Light Columns Depict Water Content Mean/Standard Deviation (Expressed in g/m^3). Black dots Represent Correlation Length in Seconds. Panels A Are Statistics for Observed Paths at Indicated Heights Above Cloud Base. Panels B are Statistics for Simulated Paths.	71
29	Path Water Content Statistics for France Cumulus Clouds. Dark/Light Columns Depict Water Content Mean/Standard Deviation (Expressed in g/m^3). Black dots Represent Correlation Length in Seconds. Panels A Are Statistics for Observed Paths at Indicated Heights Above Cloud Base. Panels B are Statistics for Simulated Paths	72
30	Path Water Content Statistics for South Africa Cumulus Clouds. Dark/Light Columns Depict Water Content Mean/Standard Deviation (Expressed in g/m^3). Black dots Represent Correlation Length in Seconds. Panels A Are Statistics for Observed Paths at Indicated Heights Above Cloud Base. Panels B are Statistics for Simulated Paths ..	73
31	Time Series of LWC in g/m^3 (Panel A) and Autocorrelation Function (Panel B) for Simulated Path HAL5 through Nova Scotia Stratus Cloud ..	76
32	Time Series of LWC in g/m^3 (Panel A) and Autocorrelation Function (Panel B) for Simulated Path HAL2 through Nova Scotia Stratus Cloud ..	77
33	Path Water Content Statistics for Nova Scotia Stratus Cloud. Dark/Light Columns Depict Water Content Mean/Standard Deviation (Expressed in g/m^3). Black dots Represent Correlation Length in Seconds. Panels A Are Statistics for Observed Paths at Indicated Heights Above Cloud Base. Panel B are Statistics for Simulated Paths ...	78
34	Time Series of LWC in g/m^3 (Panel A) and Autocorrelation Function (Panel B) for Observed Path P4 through Montana Cumulus Cloud	79
35	Time Series of LWC in g/m^3 (Panel A) and Autocorrelation Function (Panel B) for Observed Path P1 through Montana Cumulus Cloud	80
36	Time Series of LWC in g/m^3 (Panel A) and Autocorrelation Function (Panel B) for Simulated Path MONV06 through Simulated Montana Cumulus Cloud	82

37	Time Series of LWC in g/m^3 (Panel A) and Autocorrelation Function (Panel B) for Simulated Path MONV02 through Simulated Montana Cumulus Cloud	83
38	Path Water Content Statistics for Montana Validation Case Cumulus Clouds. Dark/Light Columns Depict Water Content Mean/Standard Deviation (Expressed in g/m^3). Black dots Represent Correlation Length in Seconds. Panels A Are Statistics for Observed Paths at Indicated Heights Above Cloud Base. Panels B are Statistics for Simulated Paths .	84
39	Validation Simulation Cloud Scene	86
40	Schematic Representation of Data Flow through Fast-Map Driver	90
41	Typical Modified Gamma Particle Size Distribution Broken into Discrete Size Bins	91
42	Translation of the 3-D Cloud Water Content Grid into a 2-D Table of Number Densities for Discrete Size Bins	94
43	Transformtaion of 2-D Table of Microphysical Properties into Tables of Optical, Radiative, and Graphical Properties.	98
44	Radiative, Optical, and Microphysical Properties of Volumes are Identical in These Two Equivalent Scenarios. The Intensities Incident on the Volume Elements and Sensors are Different, but the $(\tau, \epsilon, \rho, \alpha)$ are the same	98
45	Translation of Number of Density to Optical Depth and Transmittance Through a Particle Size Dependent Interpolation.	100
46	3-D Grid Reconstruction from 2-D Table	101

LIST OF TABLES

Table	Page
1 Cloud Types Simulated With the CSSM	6
2 RSA Parameters Used in Horizontal Cloud Distribution	13
3 RSA Parameters Used in Cloud Base Generation	17
4 Maximum Condensed Moisture (in g/m^3) as a Function of Cloud Type and Temperature (From Ref. 9)	20
5 RSA Parameters Used in Internal Water Content Generation	24
6 Standard Deviation of Internal Water Content Values as a Percentage of the Average Water Content for the CSSM Cloud Types	24
7 Synoptic Weather Types for Which Observations Were Obtained	44
8 Rain Rates as a Function of LWC	45
9 Sample Computed LWC "Sounding"	47
10 Sample Surface Rain Rate Calculation (Values in mm/hr)	51
11 Summary of Datasets Used in This Study	55
12 Selected Paths	56
13 LWC Statistics for Observed Paths Used in Parameter Estimation	64
14 Atmospheric Profiles Used to Initialize Cumulus Simulations	67
15 Final Cumulus Model Parameters	70
16 LWC Statistics for Simulated Paths Used in Cumulus Model Parameter Estimation	70
17 Atmospheric Profile Used to Initialize Stratus Simulations	74
18 Final Stratus Model Parameters	74
19 LWC Statistics for Simulated Paths Used in Stratus Model Parameter Estimation	75
20 LWC Statistics for Observed Paths Used in Cumulus Validation	81
21 LWC Statistics for Simulated Paths Used in Cumulus Validation	81
22 Parameters for Fog and Cloud Size Distribution Models Used in LOWTRAN & FASCODE (From Ref. 4)	92

1.

INTRODUCTION

This document provides the science behind the suite of tools developed under the Atmospheric Modeling and Visualization program at TASC. These tools include:

- the Cloud Scene Simulation Model (CSSM)
- the cloudviewer visualization tool
- the Fast-Map visualization processor.

Part of the development of the Fast-Map processor was funded through and performed under a separate contract, Contract Number F19628-91-C-0117.

Program Objective

The Atmospheric Modeling and Visualization Program at TASC supports the modeling and simulation of weather sensitive systems by building models that simulate the natural cloud environment that these systems operate within. With the support of the U.S. Air Force Phillips Laboratory, TASC has developed the Cloud Scene Simulation Model and associated post-processors which simulate the natural cloud and precipitation environment for a range of applications in the DoD modeling and simulation community. These applications include, but are not limited to

- scene visualization
- sensor test and evaluation
- image degradation
- signal attenuation
- ground temperature modification (due to cloud shadows)
- ground mobility modification (due to precipitation).

These applications are typical of the types of simulations being discussed and developed by the DoD modeling and simulation community. All of these applications require or could benefit from a high resolution realistic natural environment. The CSSM is one of many support models that will be used to support the characterization of that environment.

Atmospheric Modeling and Visualization Program Overview

The Atmospheric Modeling and Visualization program effort was broken down into seven major tasks outlined below:

Task 1 — Requirements Analysis and Software Design

Through discussions with the customer, DIS developers, and system users, determine detailed requirements for the atmospheric models and visualization software. Refine the existing model design to account for those requirements along with changes in the programming language (FORTRAN77 to ANSI C) and additional model functionality.

Task 2 — Cumulus Cloud Model Enhancements

Modify the existing cumulus model to include a more sophisticated treatment of water. Refine the model physics to handle interacting parcels, time- and location-dependent rates of entrainment, diffusion, and precipitation. Add terrain-driven heating along with general orographic effects mentioned in the following task. Develop a model for rain processes within cumuliform clouds based on analysis of precipitation data (see Task 4).

Task 3 — General Model Enhancements

Develop a model for rain processes within stratiform clouds based on analysis of precipitation data (see Task 4). Modify the model to accept and use higher-resolution environmental input data such as gridded cloud cover amount, cloud type, and ground elevation data. Develop models for orographic and other structured cloud types (e.g., cloud streets and wave clouds downwind of elevated terrain).

Task 4 — Data Analysis (Parameter Estimation and Model Validation)

Obtain and analyze atmospheric data to use in parameter estimation and model validation. If necessary, modify current model algorithms or select new algorithms to better match the empirical data. Validate specific elements of the cloud model for which we have obtained sufficient observations to support statistical validation.

Task 5 — Scene Visualization

Develop a computationally-efficient (quick-look) visualization capability to render model output. Provide SGI-oriented user interface for quick-look tool.

Task 6 — Wavelength-Dependent Visualization

Develop a physics-based visualization tool that enables rapid generation of cloud scenes at different wavelengths (e.g., long wave infrared versus visible wavelengths). Use climatological assumptions (e.g., cloud droplet distributions) and parametric radiometric computations in tool development. Develop a method to produce real-time visualization of infrared images of stratus clouds (i.e. "Fast-Map"). Assist Loral with developing visualization techniques within a DIS environment.

Task 7 — Documentation

Prepare progress and technical reports. Prepare user guides to accompany model and visualization software.

Fast-Map Extension for Water Clouds Task Overview

The Fast-Map Extension for Water Clouds was performed with support from Philips Laboratory as a task under a separate contract, Contract Number F19628-91-C-0117. The AMV program developed software (the Fast-Map processor) to support real-time infrared (IR) visualization of stratus clouds only. The Fast-Map extension task added the capability to support visualization of other water clouds (such as cumulus and stratocumulus) in visible as well as IR wavelengths.

CSSM Overview

The Cloud Scene Simulation Model is an empirical cloud model developed to support high-fidelity scene simulation in general, and DIS-compatible simulation in particular. The CSSM simulates realistic high-resolution cloud and precipitation features, defined by larger-scale weather conditions (including wind, temperature, and dewpoint temperature profiles) and coincident cloud layer inputs (cloud amount, base and top heights). The model relies on stochastic field generation techniques and convection physics to convert these weather data into cloud and precipitation fields to be rendered in the simulation domain.

This version of the model is built upon the CSSM developed previously for the Smart Weapons Operability Enhancement (SWOE) Program (Ref. 1). That model was written entirely in FORTRAN 77. It supported multi-layer cloud field generation for all of the major cloud types (including cirriform, cumuliform, and stratiform types).

This latest version of the CSSM employs many of the same techniques developed for the SWOE version of the model. However, it is written in ANSI C and is intended to support larger-scale cloud simulations (in space and time) in addition to the smaller-scale simulations supported previously. It has been modified to satisfy demands for interoperability (i.e., fair play) between disparate simulation participants. It also includes many enhancements to the SWOE version including a precipitation model, initialization with spatially- and temporally-varying input fields, additional structured cloud types, an enhanced cumulus model, improved estimates for internal model parameters, a movable simulation domain, terrain-effects on cloud formation, etc.

Cloudviewer Overview

The cloudviewer is a visualization tool to examine water content files generated by the CSSM. It was originally built to aid model developers by offering a quick means to view the CSSM output cloud fields. It was developed for Silicon Graphics, Inc. workstations running the IRIX operating system and uses the GL graphics libraries. The cloudviewer provides visualizations of cloud model output using relatively simple volume rendering techniques. It renders a cloud field by randomly placing a number of small “points” within each output volume gridpoint (voxel). The opacity of the point particles is a function of the water content at each voxel. The color, or intensity, of the points is determined using one of two shading algorithms. Depth shading colors the points as a function of their vertical position within the cloud layer. Gradient shading computes the brightness of a voxel based on surface effects, where the curvature of the surface is defined by the gradient of the water content field at every gridpoint.

The cloudviewer is an interactive tool that allows the user to rotate the cloud volume and zoom in and out of the scene. This enables the user to better analyze the three-dimensional structure of the cloud fields. In addition, a graphical user interface provides the tools to vary several visualization parameters (e.g., the number of points per voxel) to achieve a visual representation that best matches the type and characteristics of a given cloud field.

Fast-Map Overview

The “Fast-Map” post-processor is a tool developed to speed the creation of visible and infrared (IR) images of 3-D water clouds, such as stratus and cumulus, by providing physics-based optical, radiative and graphical quantities for rendering. The approach is based on the conversion of water content into graphical quantities, such as transparency, absorptivity, and diffusivity, through a series of analytic processes.

The heart of the Fast-Map approach is the construction of a database of 2-D tables relating cloud water content to cloud type, particle size, optical properties (single-scatter albedo), radiative properties (transmittance), and graphical quantities. Look-up tables are utilized, with links between the key entries of each table.

Fast-Map is *not* designed to generate or render scenes. Instead, it is designed to produce a 3-D grid of graphical quantities based on the physics of clouds, removing that burden from the software used by a rendering engine.

Organization of this Report

This section describes the organization of this report. Section 2 provides information on the CSSM. It includes a brief discussion on the motivation for the CSSM and typical scenarios for its use. Next, we describe the CSSM methodology for generating various cloud types and results. Section 2 concludes with discussions of the CSSM rain model and the cloud model parameter estimation and cumulus model validation results.

Section 3 addresses the visualization tools developed as part of the Atmospheric Modeling and Visualization effort. First we discuss the cloudviewer visualization tool. Next we describe the Fast-Map post-processor to generate graphical quantities from CSSM output. Chapter 4 provides a summary and recommendations.

2. THE CLOUD SCENE SIMULATION MODEL

The Cloud Scene Simulation Model consists of both a cloud water model and a precipitation model. The cloud model generates cloud water density values (grams/m³) at each grid-point within a three-dimensional output domain defined by the user. It is capable of simulating multi-layer cloud scenes composed of any of the cloud types listed in Table 1.

Table 1 Cloud Types Simulated With the CSSM

CLOUD TYPE ABBREVIATION	CLOUD TYPE NAME
ci	cirrus
cc	cirrocumulus
cs	cirrostratus
st	stratus
as	altostratus
ns	nimbostratus
sc	stratocumulus
ac	altocumulus
cu	cumulus
cp	precipitating cumulus
scs	stratocumulus cloud streets
stw	stratus wave clouds

The precipitation model simulates rain rate values (mm/hour) within the nimbostratus and precipitating cumulus cloud types. These rain rates produced with the precipitation model, along with the water content values generated with the cloud model, define the cloud environment for use in a variety of simulation applications. These two models are described in the Sections 2.1 and 2.2.

2.1 THE CLOUD MODEL

2.1.1 Motivation

Advanced simulation applications, now under development by members of the DoD community, will require high-fidelity atmospheric descriptions to enhance the realism of the training environment. Many systems used in the battlefield environment are affected by cloud water. The cloud model provides the underlying data fields that can be used as input to these systems for training purposes to degrade visibility on the field, modify ground temperature, obscure targets, and introduce background clutter.

All cloud fields are built for consistency with user-supplied input weather conditions. Note, that the motivation for the cloud model is not to recreate the exact cloud conditions present on any given day. Rather, the motivation is to generate a cloud field that is representative of a given weather state. Thus, the model supports the typical "what if?" scenarios posed by the simulation community. For example, the model can help answer the following types of questions

- "What if it's a partly cloudy day with stratus ceilings at 1000 meters? How will myIRST system perform?"
- "What if scattered cirrus is present at 8000 meters? How will my millimeter wave system respond?"
- "What if a fast moving rain system passes through the region of interest? How will tank mobility be affected?"
- "What if fair weather cumulus clouds are present? How will visual air-to-ground targeting be affected?"

Obviously, the cloud model only answers one part of these questions; it simulates the environmental cloud information. Other simulators must use that information to derive sensor-specific quantities or other physical properties to determine the effects of the clouds on various weather-sensitive systems.

2.1.2 Typical Scenarios

As mentioned previously, the CSSM is being developed to support a wide variety of applications. However, its primary use is in providing an efficient tool to simulate the natural environment in DoD training and simulation applications. Specifically, the CSSM development has been funded by the U. S. Air Force Phillips Laboratory, the Defense Modeling and Simulation Office, and the U.S. Army Topographic Engineering Center as part of the Dynamic Environment and Terrain Modeling in DIS Program which

seeks to develop enhanced environmental representation for use in future large-scale DIS exercises such as those planned under the Synthetic Theater of War (STOW) Program.

These planned large-scale simulations will run for days and cover large spatial areas. A typical scenario may require cloud scenes every 5 minutes for several days in variable size domains scattered over a 600×800 km domain. Interoperability among all simulation participants will be required. Multiple layered cloud scenes with precipitation will be generated. Output domains will move as the simulation progresses. Gridded meteorological data will be available from a numerical weather prediction model, and high-resolution terrain elevation data will be available everywhere in the domain. Cloud scenes will be used to augment the realism of the overall training experience as well as providing the physical variables used to derive atmospheric effects for “scene visualization” using electro-optical sensors.

In contrast, another scenario that is typical of a sensor test and evaluation study will use the CSSM in stand-alone mode. In this type of application, the CSSM will be used to generate a wide variety of cloud conditions to “stress” a sensor’s response to variability in cloud structures (edges, etc.), water content values, cloud types, altitudes, etc. Such a scenario will require a cloud fields over a relatively small area (5×5 km). Interoperability with other simulators will not be required. The position of the output domain will be fixed. Single-valued inputs will be used to drive cloud simulation including soundings and coincident cloud observations sampled from a climatological data base or weather station history. Real-time data initialization will not be required. Cloud scenes will be used as inputs to radiometric calculations of atmospheric effects on sensor performance. Monte Carlo simulations may be run in which large numbers of cloud scenes are generated to test the effects of slight variations in cloud distributions on the sensor system.

The two scenarios described here represent the two most distinct modes of operation for the CSSM. The model has been built to satisfy both of these modes as well as the broad range of applications in between.

2.1.3 Overall Methodology

The cloud model is an empirical model that generates high-resolution, four-dimensional (three spatial and time), multi-layer cloud fields consistent with larger-scale cloud conditions. That is, it simulates realistic structure (typical resolutions of 10–100 meters) within a domain defined by general meteorological characteristics. A key characteristic of the model is its computational speed. The CSSM is **not** a physics-based numerical cloud

model. Instead, it relies on efficient stochastic field generation techniques to simulate realistic cloud and precipitation structure.

One output field is generated by the cloud model for each specified output time and contains cloud water density values arranged on a regular volumetric grid. The CSSM simulates a variety of cloud types including cirriform (high, thin cloud streaks), stratiform (low, homogeneous cloud layers), and cumuliform (puffy, vertically-developed convective clouds). Two structured cloud types are also included: stratocumulus cloud streets and stratiform orographic wave clouds.

The model uses a fractal algorithm (the Rescale and Add algorithm, Ref. 4) to specify the horizontal distribution of cloud elements across the user-specified model domain, where parameters within the fractal algorithm are tuned to fit observed cloud data (e.g. the variability of liquid water density within cloud elements of differing types is controlled by a "length" parameter within the algorithm which was selected by an analysis of aircraft-based cloud measurements). The vertical growth of the clouds is modeled using convection physics (cumuliform types) and heuristics (stratiform and cirriform types). Comparisons with real data have shown that the model captures the characteristically complex internal and external structure of cloud fields observed in nature.

2.1.4 Primary Procedures

The cloud model is composed of a series of procedures that take the user from a general input field description (i.e., partly cloudy day, with stratocumulus layer at 2000 meters) to a specific synthetic scene that is representative of the general inputs. The following sections describe the process of going from the general to the specific. Many procedures in the CSSM are cloud type independent. Those are described first. Cloud-type-dependent procedures (i.e., stratiform, cirriform, and cumuliform procedures) are presented later in this section. All procedures are presented in roughly chronological order as they occur in the model software. The emphasis in this report is on the science behind each of the procedures. Software implementation details can be found in the accompanying User's Guide (Ref. 2).

2.1.4.1 Procedures Common to All Cloud Types

Process Inputs

The CSSM begins by processing the user-supplied input sources. Four input data sources are required: a user-generated parameter file, coarse-resolution meteorological (met) conditions (winds, temperature, dewpoint temperature, geopotential height), coarse-resolution cloud layer information (amount, base and top heights), and terrain-elevation

across the simulation domain. The met, cloud, and terrain data can be specified as single-valued inputs (homogeneous across the simulation domain) or gridded inputs (variable across the domain). See Ref. 2 for detailed information on input data formats.

Interpolate Met and Cloud Data in Time

The meteorological and cloud layer data can vary in time. The CSSM interpolates both data types with a frequency defined by the TUPDATE parameter (set to 5 minutes). Temporal interpolation consists of two components; advection and linear interpolation (where advection is the movement of large-scale features across the simulation domain). First, average winds are determined at the given time by linearly interpolating u and v wind components between the two bounding input data times. The resulting average wind field is used to determine advection distances for the two input data times. The advection distance is the distance that the met or cloud structures travel during the time period between the input data time and the valid time. For example, to build a cloud field at time t , we use available cloud fields at times t_1 and t_2 . For each position in the field at time t , the model finds the corresponding position in the field at time t_1 where the large-scale features would be “advected from” and the corresponding position in the field at time t_2 where the large-scale features would be “advected to” assuming that met and cloud features move with the average wind field. The advection positions at times t_1 and t_2 are computed as follows

$$\begin{aligned} dt_1 &= t - t_1 \\ dt_2 &= t - t_2 \\ x_1 &= x - u * dt_1 \\ y_1 &= y - v * dt_1 \\ x_2 &= x - u * dt_2 \\ y_2 &= y - v * dt_2 \end{aligned}$$

where

- dt_1 and dt_2 are the time differences between the bounding input times (t_1 and t_2) and the valid model time (t), respectively
- x and y are the Cartesian coordinates of the gridpoint being processed at time t
- x_1 and y_1 are the Cartesian coordinates of the “advected from” gridpoint at time t_1
- x_2 and y_2 are the Cartesian coordinates of the “advected to” gridpoint at time t_2
- u and v are the average wind components linearly interpolated from the bounding met data files.

The met and cloud variables at these positions within the t_1 and t_2 input fields are retrieved. The model then linearly interpolates from these values to determine the met and cloud variables at the time t . This procedure ensures that the weather conditions used in the model at any time are smoothly varying in time and continuous across input time boundaries.

Temporal and spatial variability in the cloud fields is added later using a fractal algorithm. Advection and linear interpolation as described above is performed only on the relatively coarse-resolution input fields.

Initialize the Advection Field (Model Spin-Up)

One way in which the CSSM ensures interoperability is by ensuring that all participants start with the same cloud history. That is, since the model relies on advection for large-scale cloud motion, it must ensure that all participants are working with the same advection field at any given time. To generate a history of advection values, the model calculates the coarse-resolution advection field (in time steps equal to TUPDATE) from the beginning of the overall simulation through the time that the individual simulator joins. This process involves reading all necessary input met data fields, performing temporal interpolation, and computing advection distances based on average wind components. This process is part of the model spin-up period when an individual simulator joins an ongoing simulation. It is not necessary for a stand-alone simulator. This process can be lengthy for simulators joining very late in an exercise and needs to be accounted for when starting a simulation.

Define Working Domain

After model spin-up is complete, the internal working domain must be defined. The size of the CSSM working domain is larger than the user-specified output domain to account for two factors: advection into the output domain and continuity across domain boundaries (i.e., interoperability). First, the domain is expanded along the wind direction by an amount equal to the advection distance. The advection distance is calculated for a time period equal to TUPDATE and assumes a wind speed equal to the average wind speed at the cloud base height.

Second, the domain is expanded to ensure interoperability. Several key variables in the CSSM are generated on a grid box by grid box basis (a grid box is defined to be an input cloud gridpoint). These variables are then interpolated to the high resolution output

grid. To ensure that all participants in a simulation reproduce the identical cloud field, the domain is enlarged by at least 1/2 grid box so that the interpolated values near the border of the domain are computed identically. Figure 1 shows how the output domain is expanded first to account for advection, and second to ensure interoperability near the borders.

Once the overall working domain is defined, the CSSM steps through each input grid box contained within the working domain and simulates the cloud field within each box. Grid boxes are processed one-by-one to reduce the amount of data that needs to be stored in computer memory at any one time. All model procedures have been implemented to ensure that data fields are continuous across all grid box boundaries.

Interpolate Met, Cloud, Advection, and Terrain Data in Space

In those cases in which gridded inputs are supplied to initialize the cloud model (rather than single-valued inputs), the CSSM linearly interpolates from the coarse-resolution input values to the finer-resolution output grid resolution for each grid box that is processed. The resulting high-resolution fields are used throughout the cloud generation process. We implemented a two-pass Barnes analysis scheme to handle the interpolation at the early stages of the model implementation, but later determined that the more efficient simple bilinear interpolation method would be adequate given the regular structure of the gridded input fields.

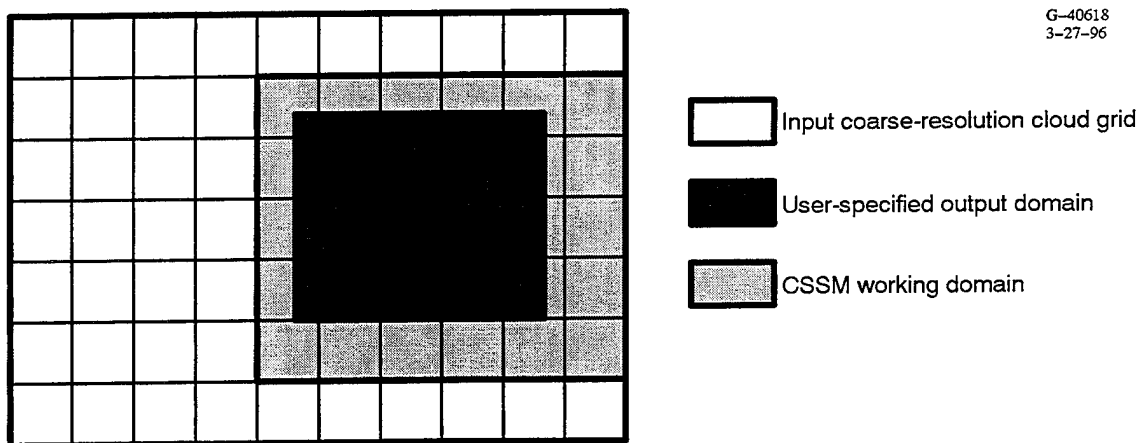


Figure 1 Grid Domains Used in the CSSM

Generate Horizontal Fractal Field

Beginning with Lovejoy's 1982 paper (Ref. 5) in which he made the case that cloud and rain fields behave as scaling fractals over scales ranging from 1–1000 km, and continuing with Cahalan's analysis of fair weather cumulus, ITCZ clouds, and marine stratocumulus (Refs. 6, 7), there is significant evidence that fractal models of cloud structures are appropriate and that many cloud types adhere to either single or multi-fractal scaling laws. The CSSM relies heavily on a fractal field generation algorithm to create synthetic cloud scenes. The model employs the Rescale and Add (RSA) fractal algorithm (Ref. 4) in several processes including the generation of the horizontal cloud distribution. The RSA algorithm provides an efficient point-wise evaluation of the fractal function at every grid-point in the working domain. It was used in a previous version of the CSSM and was documented in a previous technical report (Ref. 1). The RSA model, as implemented in the CSSM, approximates fractional Brownian motion in four dimensions (x, y, z, time) as the sum of individual "frequencies" sampled from a four-dimensional lattice of random numbers. The lower frequencies provide large-scale structure in the cloud field and the higher frequencies provide texture within the cloud elements. We control the character of the resulting cloud field by controlling two key parameters in the RSA model; the Hurst parameter and the lattice resolution. A list of the values used for each cloud type is included in Table 2. Many of these values have been updated since the last version of the CSSM was released based on continued analysis of cloud model output fields.

Table 2 RSA Parameters Used in Horizontal Cloud Distribution

CLOUD TYPE	HURST PARAMETER	LATTICE RESOLUTION
cirrus	0.3	5, 20
cirrocumulus	0.2	3, 9
cirrostratus	0.3	10, 30
stratus	0.5	20
altostratus	0.5	20
nimbostratus	0.7	15
stratocumulus	0.3	6
altocumulus	0.3	6
cumulus	0.2	2
precipitating cumulus	0.2	2
stratocumulus cloud streets	0.3	1
stratus wave clouds	0.3	8

The CSSM generates a new horizontal cloud distribution every TUPDATE (300) seconds. For each update time, the CSSM loops through each input grid box and cloud layer and builds a horizontal fractal field at the cloud base level for each layer. The four-dimensional fractal lattice is evaluated at each gridpoint in the grid box at the local cloud base level and valid time. The result is a two-dimensional field of RSA field values with variability determined by the cloud-type-dependent RSA parameters. Figure 2 shows an example of such a field where the RSA values have been scaled to 256 gray levels. The brightest areas correspond to the highest RSA values and the darkest areas correspond to the lowest RSA values. Over large regions (large with respect to the size of any individual cloud element), the fractal field values are approximately Gaussian-distributed, with a mean of 0.0 and a standard deviation of slightly less than 1.0. These RSA field values are later transformed to a horizontal cloud map as described in the next procedure.

Convert Fractal Field to Horizontal Cloud Distribution

The RSA field generated in the previous step forms the basis for the horizontal cloud distribution (the same field is used again in a later procedure to define the vertical cloud structure). To create the horizontal cloud distribution, the Gaussian-distributed RSA field values are transformed to a uniform distribution using the standard error function routines provided in Ref. 8. Figure 3 shows the RSA field displayed previously in Figure 2 after being transformed to a uniform distribution.

After the RSA field is transformed to a uniform distribution, a histogram of the field values is generated and a threshold value is determined for the grid box which produces the desired amount of cloud cover in the box. A threshold value is identified for each



Figure 2 RSA Field (scaled to 8 bits)



Figure 3 RSA Field After Transformation to Uniform Distribution
(scaled to 8 bits)

grid box in a first pass through the overall working domain. The resulting threshold values are interpolated (using bi-linear interpolation) across all input grid boxes that cover the working domain. (Smoothing the threshold values is necessary to ensure continuity across grid box boundaries of very different cloud amounts.)

During the second computational pass through the working domain, the RSA field values are regenerated, transformed to uniform distribution, and then compared one-by-one to the smoothed threshold field. At each gridpoint, the transformed RSA value is compared to the corresponding threshold. The gridpoint value is set to zero if it falls below the threshold value (i.e., no cloud present). All gridpoint values equal to or above the threshold value are determined to be cloud filled. Figure 4 shows the sample RSA field presented previously after the thresholding process. All black areas are cloud free. All other gridpoints are determined to contain cloud, with the brightest colors corresponding to the highest RSA field values.

The horizontal RSA field which is produced by this process defines the horizontal distribution of cloud elements across the working domain. It is also used in one of two ways depending on the cloud type:

- stratiform/cirriiform – RSA field is transformed to cloud top heights
- cumuliform – RSA field is transformed to heating field to drive parcel convection.

Each of these processes is described later in this section.



Figure 4 RSA Field After Thresholding Process
(scaled to 8 bits)

2.1.4.2 Stratiform Procedures

Build Cloud Base

Once the horizontal distribution of cloud features is defined using the RSA model, the stratiform model updates the cloud base field at all cloud-filled gridpoints. The RSA model is used again to generate a two-dimensional stochastic perturbation field that is added to the input cloud base field (smoothed by interpolating user-specified input cloud base heights to the working domain). The updated base height is computed as follows

$$\text{base} = \text{base} + \text{base}_{\text{perturbation}} \quad (2-1)$$

where

- base is the updated cloud base height including fractal “bumpiness”
- base is the nominal cloud base height interpolated from user-specified inputs to the working grid
- $\text{base}_{\text{perturbation}}$ is a stochastic height perturbation added to introduce variability in the cloud base structure.

The 4-d RSA lattice is evaluated at every cloud-filled gridpoint in the working domain using the same procedures described above in the section titled “generate horizontal cloud distribution.” The RSA values are then transformed to cloud base perturbations. The RSA field generation procedures are called with parameters tuned for cloud base generation. Again, we vary only the Hurst parameter and lattice resolution to capture varying levels of “bumpiness” in the cloud base structure for the twelve different cloud types. The parameters used in cloud base generation are listed in Table 3.

Table 3 RSA Parameters Used in Cloud Base Generation

CLOUD TYPE	HURST PARAMETER	LATTICE RESOLUTION
cirrus	0.3	1.5,1.5
cirrocumulus	0.3	1, 1
cirrostratus	0.3	2,2
stratus	0.5	1
altostratus	0.3	1
nimbostratus	0.3	1
stratocumulus	0.3	1
altocumulus	0.3	1
cumulus	N/A	N/A
precipitating cumulus	N/A	N/A
stratocumulus cloud streets	0.3	0.5
stratus wave clouds	0.3	0.5

The RSA field values (typical RSA field distributions have mean of approximately 0, standard deviation slightly less than 1, and a range of -5 to +5) are transformed to cloud base perturbations as follows

$$\text{base}_{\text{perturbation}} = \text{rsa} / 5.0 * \text{base_percent} * (\text{top} - \text{base}) \quad (2-2)$$

where

- rsa is the fractal field value generated with the RSA algorithm
- base_percent is a parameter which controls the overall amount of cloud base variations (0.5 in the current version of the model)
- top is the nominal cloud top height interpolated from user-specified inputs to the working grid
- base is the nominal cloud base height interpolated from user-specified inputs to the working grid.

Figure 5 shows a gray-scale image of a cloud base perturbation field for a stratocumulus cloud layer.

Build Cloud Top

The stratiform model updates the cloud top field at all cloud filled gridpoints. The RSA field values that were produced by the procedures described above in the section titled “generate horizontal cloud distribution” are used here. These values were transformed to a uniform distribution, and thresholded to achieve the correct cloud amount. The updated cloud top height is computed as follows

$$\text{top} = \text{base} + (\text{top} - \text{base}) * ((\text{rsa} - \text{threshold}) / (1.0 - \text{threshold}))^{1.5} \quad (2-3)$$

where

- top is the updated cloud top height including fractal “bumpiness”
- top is the nominal cloud top height interpolated from user-specified inputs to the working grid
- base is the nominal cloud base height interpolated from user-specified inputs to the working grid
- rsa is the fractal field value generated with the RSA algorithm and transformed to uniform distribution
- threshold is the threshold value valid at the gridpoint of interest
- the exponent 1.5 was selected based on an analysis of stratiform cloud data (see Section 2.3).

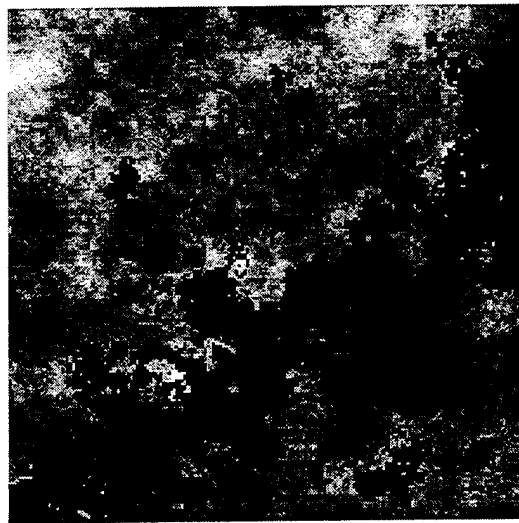


Figure 5 Cloud Base Perturbation Field
(scaled to 8 bits)

The resulting cloud tops vary from the nominal cloud base height up to a maximum of the user-input cloud top height. Figure 6 shows a gray-scale image of a cloud top field for a stratocumulus cloud layer.

The character of the resulting cloud top surface is a function of the RSA model parameters used in the generation of the horizontal cloud distribution, which are themselves functions of cloud type. Thus, the cloud top surface is more or less variable (or "bumpy") depending on cloud type. Our selection of RSA model parameters results in smoother cloud surface for a stratus cloud than an altocumulus, for example. Also, the height of the cloud top is a function of the horizontal field value. This produces higher cloud tops toward the center of the cloud elements where the RSA field values are higher than the edges of the cloud elements where the RSA field values tend to be lower.

Generate Internal Water Content

Once the cloud base and top are defined for each gridpoint in the working domain, the CSSM determines the internal water content everywhere within the cloud boundaries. The water content at each gridpoint is defined in the model as

$$WC = WC_{avg} + WC_{perturbation} \quad (2-4)$$

where

- wc is the water content at the current gridpoint
- wc_{avg} is the average water content
- $wc_{perturbation}$ is a small perturbation generated with the four-dimensional RSA model.

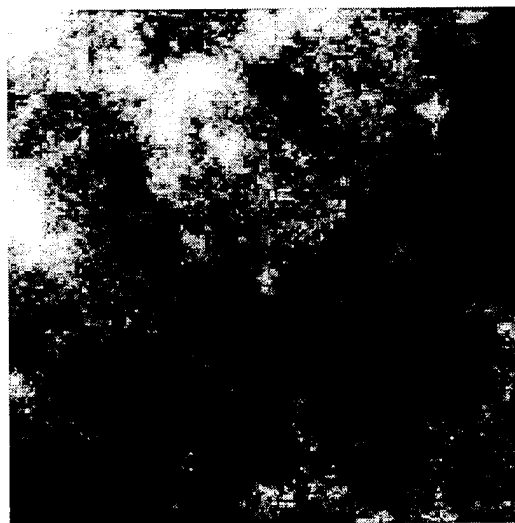


Figure 6 Cloud Top Height Field (scaled to 8 bits)

The remainder of this section describes how to calculate the average and perturbation water content values.

Compute the Average Water Content, $w_{c_{avg}}$

Following Feddes (Ref. 9), the average water content is a function of cloud type, cloud temperature, and vertical position within the cloud layer. First, for a given cloud type and temperature, the maximum condensed moisture content (in g/m^3) in the layer is retrieved from a look-up table. (That table is reproduced here in Table 4).

Table 4 Maximum Condensed Moisture (in g/m^3) as a Function of Cloud Type and Temperature (From Ref. 9)

CLOUD TYPE	<-25	≥ -25 and < -20	≥ -20 and < -15	≥ -15 and < -10	≥ -10 and < -5	≥ -5 and < -10	≥ 0 and < +5	$\geq +5$ and < +10	$\geq +10$ and < +15	$\geq +15$
ci	.10	.10	.10	.10	.15	.15	.15	.20	.20	.20
cc	.05	.05	.05	.05	.10	.10	.10	.15	.15	.15
cs	.15	.15	.15	.20	.20	.20	.25	.25	.25	.25
st	.10	.15	.20	.25	.30	.35	.40	.45	.50	.50
as	.15	.20	.25	.30	.30	.35	.40	.50	.50	.50
ns	.35	.40	.45	.50	.60	.60	.75	.90	.90	.90
sc	.20	.30	.40	.45	.50	.55	.60	.70	.70	.70
ac	.25	.30	.35	.40	.40	.45	.60	.70	.70	.70
cu	3.0	3.0	3.0	3.0	3.0	3.0	3.0	3.0	3.0	3.0
cp	3.0	3.0	3.0	3.0	3.0	3.0	3.0	3.0	3.0	3.0
scs	.20	.30	.40	.45	.50	.55	.60	.70	.70	.70
stw	.10	.15	.20	.25	.30	.35	.40	.45	.50	.50

The actual water content at any point within a cloud layer is then computed as some fraction of the maximum condensed moisture based on position above the cloud base level. It can be given by the following

$$w_{c_{avg}}(z) = w_{c_{max}} * (\%cover) * F \quad (2-5)$$

where $w_{c_{max}}$ is the maximum condensed moisture (from Table 4), %cover is the fractional cloud cover at the gridpoint, and F is a function of the vertical location within the cloud layer. The fraction F, is determined from empirically-derived curves presented in Ref. 9. One of those curves has been included here as an example (Figure 7) and relates percent height above cloud base to the fraction of maximum condensed moisture.

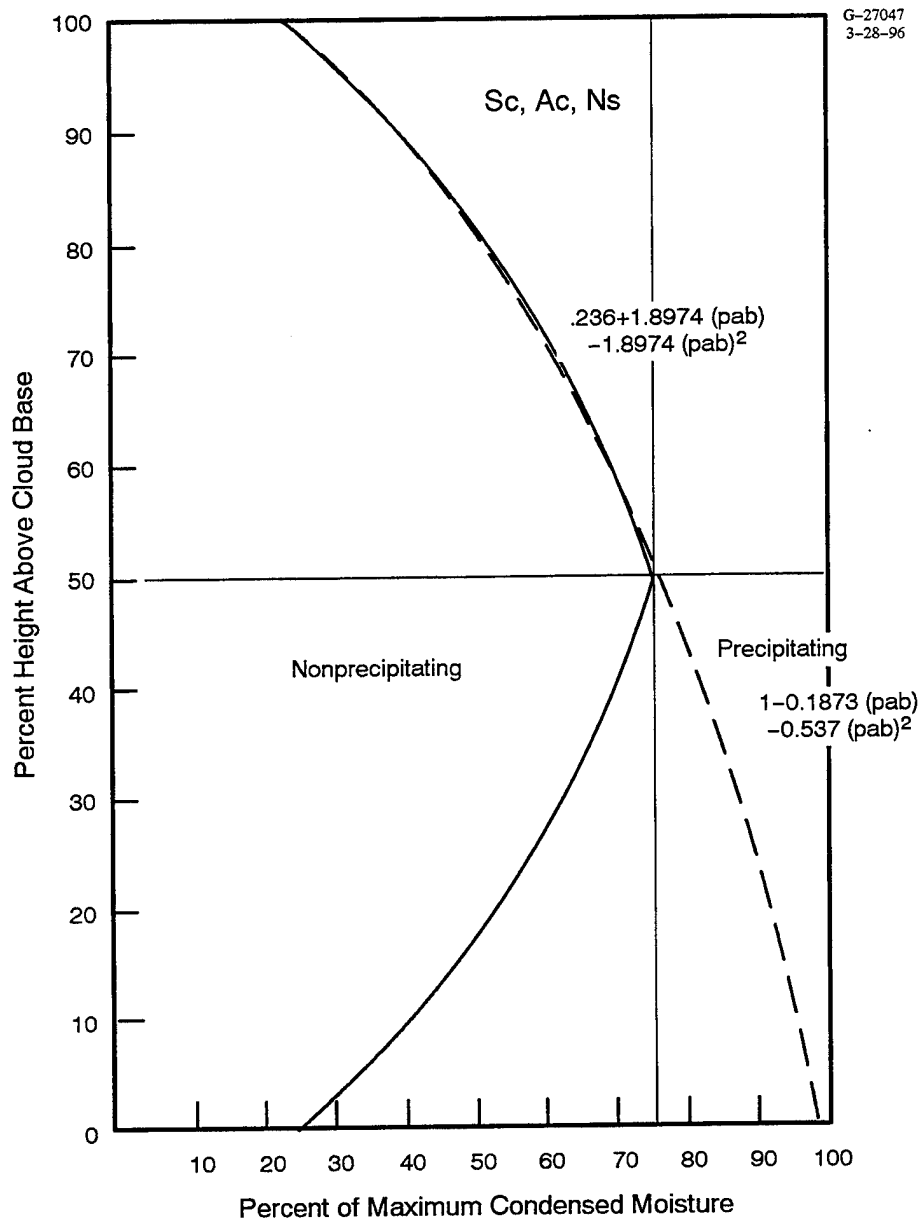


Figure 7 Vertical Cloud Profile Valid for Sc, Ns, and Ac Cloud Types (from Ref. 9)

To determine the percent height above cloud base, the CSSM first determines the percent height above the overall cloud base (that is, defined by the minimum cloud base height and the maximum cloud top height) for the layer, and then finds the percent height above the local cloud base. A weighted average of these two variables is then used. Figure 8 shows a schematic definition of the variables used to compute the percent height above cloud base.

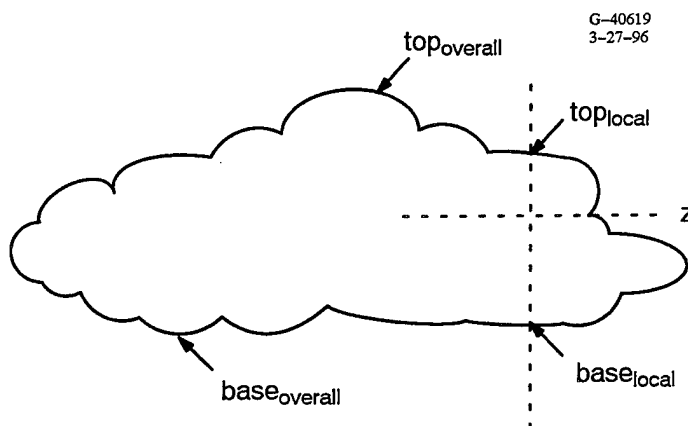


Figure 8 Schematic Showing Variables Used to Calculate $pab_{overall}$ and pab_{local} at the Dashed Location

The percent height above cloud base with respect to the overall cloud layer is defined as

$$pab_{overall} = (z - base_{overall}) / (top_{overall} - base_{overall}) \quad (2-6)$$

where z is the altitude of the gridpoint that is being processed.

The percent height above cloud base with respect to the local cloud layer is defined as

$$pab_{local} = (z - base_{local}) / (top_{local} - base_{local}). \quad (2-7)$$

These two values are combined to determine a weighted “average” position within the cloud layer

$$pab = pab_{weight} * pab_{local} + (1.0 - pab_{weight}) * pab_{overall} \quad (2-8)$$

where $pab_{weight} = 0.5$ in the CSSM.

As an example, the percent height above cloud base for the point defined as the intersection of the two dashed lines shown in Figure 8 is computed as follows, where we assume the following

$z = 2000$ meters (where z is the height of the shaded gridpoint)
 $base_{overall} = 1000$ meters
 $base_{local} = 1200$ meters
 $top_{local} = 2200$ meters
 $top_{overall} = 2600$ meters.

The percent height above cloud base is

$$pab_{\text{local}} = (2000 - 1200) / (2200 - 1200) = 0.8$$

$$pab_{\text{overall}} = (2000 - 1000) / (2600 - 1000) = 0.625$$

$$pab = 0.7125.$$

Given the resulting position within the cloud layer, the function, F , is computed from the curves presented in Ref. 9 Finally, the average water content is determined using Eqn. (2-5).

Compute the Perturbation Water Content, $w_{c_{\text{perturbation}}}$

Perturbations to the average water content field predicted by the Feddes model are added to reproduce the small scale variability in water content observed in data. The Rescale and Add model is used in the CSSM to build a perturbation field everywhere within the cloud boundaries. RSA model parameters are selected based on comparison with observed data and qualitative appearance (see Section 2.3 for details). The current values for parameters are included in Table 5. We expect these values to change as we continue to evaluate additional observations. The 4-d RSA lattice is evaluated at every point in space using the same procedures described above in the section titled “generate horizontal cloud distribution.”

The RSA values are transformed to water content perturbations by scaling the RSA field distribution by the ratio of the standard deviations of the RSA field and an assumed standard deviation of the water content. We assume the following standard deviations in water content, where all values are shown as a percentage of the average water content (see Table 6). These values were selected by analysis of cloud water observations. Unfortunately, we were unable to obtain and evaluate observations for all 12 cloud types as discussed in Section 2.3. For those cloud types where no data were available, we estimated the standard deviation based on general knowledge of the cloud characteristics. As more data become available, we plan to estimate these parameters using a more rigorous approach.

Table 5 RSA Parameters Used in Internal Water Content Generation

CLOUD TYPE	HURST PARAMETER	LATTICE RESOLUTION
cirrus	0.3	2, 10
cirrocumulus	0.3	0.5, 5
cirrostratus	0.3	2, 15
stratus	0.5	1
altostratus	0.5	1
nimbostratus	0.5	1
stratocumulus	0.3	1
altocumulus	0.3	1
cumulus	N/A	N/A
precipitating cumulus	N/A	N/A
stratocumulus cloud streets	0.3	1
stratus wave clouds	0.3	1

Table 6 Standard Deviation of Internal Water Content Values as a Percentage of the Average Water Content for the CSSM Cloud Types

CLOUD TYPE	ci	cc	cs	st	as	ns	sc	ac	cu	cp	scs	stw
Standard deviation	0.5	0.5	0.5	0.3	0.3	0.3	0.4	0.4	N/A	N/A	0.3	0.2

The transformation from RSA field value to water content perturbation value is simply

$$wc_{\text{perturbation}} = rsa * sdev_{wc} / sdev_{rsa} \quad (2-9)$$

where $sdev_{wc}$ and $sdev_{rsa}$ are the standard deviations of the water content and rsa fields, respectively.

In a final step, after calculating the water content, we set all gridpoints with a value less than two standard deviations below the mean wc (estimated by the Feddes procedure) equal to zero. This introduces small “holes” inside the cloud field, which are frequently observed in nature.

2.1.4.3 Cirriform Procedures

The cirriform model is identical to the stratiform model with two additions. First, a non-isotropic horizontal cloud distribution is simulated and second, a non-isotropic internal water content distribution is generated. Both of these processes are presented below.

Generate Non-Isotropic Horizontal Cloud Distribution

First, to simulate a non-isotropic horizontal cloud field distribution, we use non-isotropic values for the lattice resolution parameter in the RSA algorithm (as listed previously in Table 2). The model assumes that the cirriform cloud bands line up preferentially with the local wind direction. By rotating coordinate systems within the cloud model so that the y axis lies along the wind vector at the cloud base level and using different values for the lattice resolution parameter in the RSA algorithm for the rotated x and y coordinate axes, we can achieve a banded effect. A sample two-dimensional image of a non-isotropic RSA field is shown in Figure 9. Notice the strict linearity of the field.

This first step gets us part way through our cirriform cloud generation. The second step builds on the process to generate a more *realistic* cloud distribution. After rotating the model coordinate system along the local wind direction at every gridpoint, the model perturbs the resulting x position based on the value of another RSA field evaluated at that point. The parameters used to generate this perturbation field are the same as those used in the generation of the initial horizontal field (see Table 2). The updated x position is then given by

$$x_{\text{rot}} = x_{\text{rot}} + \text{rsa} * DX \quad (2-10)$$

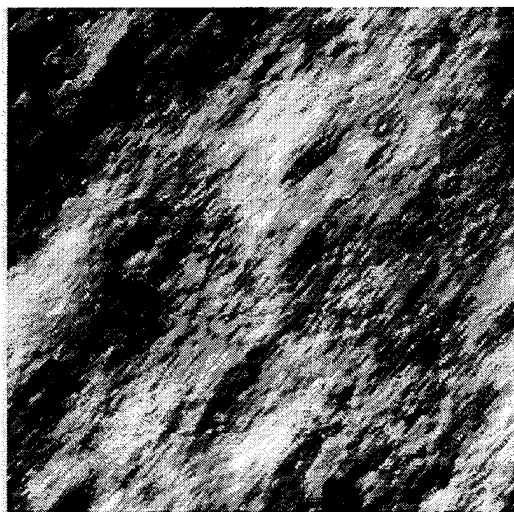


Figure 9 First Step in Cirriform Model, Horizontal Non-Isotropic Pre-Cloud Distribution (scaled to 8 bits)

where

- x_{rot} is the x position of the gridpoint with respect to the rotated coordinate system
- rsa is the value of the RSA field evaluated at $(x_{\text{rot}}, y_{\text{rot}}, z, t)$
- DX is a constant (400 meters).

By perturbing the x position before evaluating the RSA lattice for the cirriform cloud distribution, we introduce natural curves and variability into the otherwise linear field. A sample field that includes this variability is shown in Figure 10. Compare this field with that in Figure 9 which was generated over the same spatial region without this additional variability.

Generate Non-Isotropic Internal Water Content

Having built the cirriform cloud base and top structure in exactly the same way as described in Section 2.1.4.2 (stratiform procedures), the next step is to build the internal water content structure. The procedure here is nearly identical to that employed for the stratiform cloud types, however, we add one step; to build non-isotropic structure into the internal $w_{\text{c_perturbation}}$ field. We employ the same process as used to build non-isotropic structure into the horizontal cloud distribution field (see above). We rotate coordinate systems at each internal gridpoint so that the y axis lies along the wind vector, and perturb the x_{rot} position to introduce some variability into the field. We use different values for the

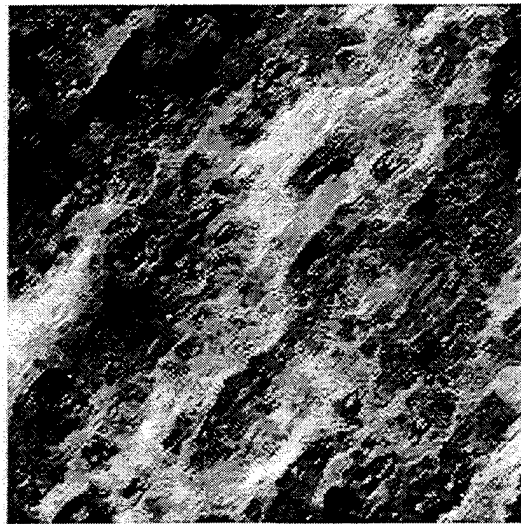


Figure 10 Cirriform Horizontal Cloud Distribution After Fractal Perturbation (scaled to 8 bits)

lattice resolution parameter in the RSA algorithm for the rotated x and y coordinate axes. This produces a naturally variable banded effect inside the cloud structure. The RSA parameters used to perturb the xrot position are the same as those listed in Table 2. As a final detail, we set all gridpoints with water content less than one standard deviation below the mean (estimated by the Feddes procedure) equal to zero. This introduces clear bands within the cloud field, which are frequently observed in nature. A slice through a sample cirrus cloud field, showing the non-isotropic external cloud shapes and non-isotropic internal moisture field is shown in Figure 11.

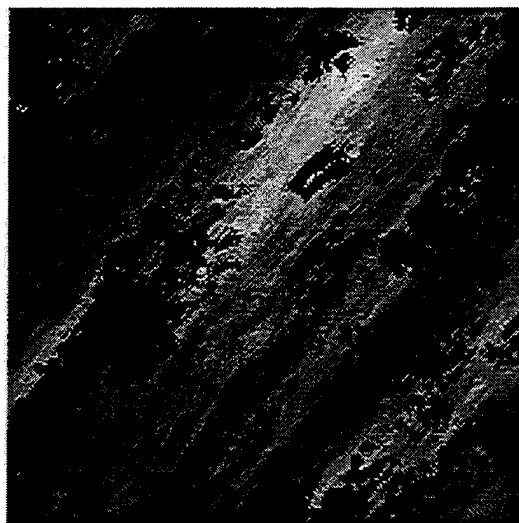


Figure 11 One Slice through a 3-d Cirrus Cloud Field
(scaled to 8 bits)

2.1.4.4 Cumuliform Procedures

The baseline convection model was described previously in Ref. 1. A brief review is included here, followed by a description of specific procedures added to or modified in the CSSM under this development effort.

The cumuliform model starts with the same horizontal fractal field used in the stratiform/cirriiform model, but rather than converting the field values to cloud top heights, it converts the field values to a heating field which is used to initialize the cumulus parcel convection model. The horizontal fractal field is evaluated at the lifting condensation level (LCL). (The LCL is the level at which parcels lifted adiabatically from the surface become saturated.) Field values are converted to perturbation temperatures, where the perturbation is defined with respect to the ambient temperature. The variability of the heating field is defined by the internal RSA model parameters. Parcels are released at

random locations across the working domain with a buoyancy determined by the local perturbation temperature. A central finite difference solution to the differential equations that control parcel motion is employed. Mixing with the environmental air is accounted for (where entrainment rates vary as a function of position within the cloud), the water balance is evaluated at each time step, and water content is computed for each parcel. Finally, the collection of parcels is evaluated and the water content at each output gridpoint is computed as the average of all overlapping parcels.

Convert Fractal Field to Temperature Perturbation Field

The cumulus model starts with the horizontal RSA field which has been transformed to a uniform distribution and thresholded based on the cloud amount across the working domain. The resulting data field is converted to a temperature perturbation field using the following linear transformation

$$T_{\text{perturbation}} = (\text{rsa} - \text{threshold}) / (1 - \text{threshold}) * (T_{\text{max}} - T_{\text{min}}) + T_{\text{min}} \quad (2-11)$$

where

- rsa is the RSA field value (rsa=0 for clear gridpoints or threshold<rsa<1 for cloud-filled gridpoints)
- threshold is a cutoff value used to define cloud/no cloud regions and producing in the desired cloud fraction
- T_{max} is the maximum perturbation temperature (0.5 Kelvin in the current version of the CSSM)
- T_{min} is the minimum perturbation temperature (0.1 Kelvin in the current version of the CSSM).

The values of T_{min} and T_{max} were selected based on comparison of model-produced cumulus scenes with observed cloud data. We selected values that best reproduced the cloud base and top heights along with the magnitude of the water content inside the cloud structures.

Initialize Parcels

Parcels are released continuously throughout the model run. When initializing the CSSM with gridded cloud input data, each grid box is processed independently and parcels are released randomly across each box area. For single-valued cloud input data, the working domain is divided into boxes the size of “release_box_size” (5 km on a side in the current model). Both of these geometries ensure reproducible results which is required for

interoperability. The number of parcels released is a function of the size of the release box and the cloud amount in the layer. Thus, cloud layers with higher fractional cloud cover use a greater number of parcels for coverage.

At each time step in the model, we loop through all release boxes and determine a number seed that will control the position of the parcels within the box. The number seed is calculated from the box position and the model time. Thus, interoperability is ensured as individual simulators will start with the same number seed for the same position and time. To initialize the (x, y) position of each parcel, two random numbers are derived from the initial number seed. All parcels start with $z=lcl_{local}$.

From this (x, y, z, t) position, the four-dimensional RSA field is evaluated and the perturbation temperature is retrieved. The perturbation temperature is added to the ambient air temperature at that point, making the parcel positively buoyant. The size of the parcel is defined as a linear function of the perturbation temperature, where more buoyant parcels are larger, and less buoyant parcels are smaller.

Update Parcels

(Much of this section is taken directly from the cumulus model discussion presented in our previous technical report, Ref. 1. It is included here for completeness.)

During each time step in the cumulus model, after a set of new parcels is released as described above, the physical attributes of every parcel (newly- and previously-released) are updated. First, the instantaneous vertical parcel acceleration is computed (derived from Newton's second law and the equation of state for an ideal gas) as follows

$$a = g (Tv_p - Tv_a) / Tv_a \quad (2-12)$$

where

- we use the subscript "p" to denote parcel and "a" to denote ambient conditions
- g is the gravitational acceleration (a function of altitude)
- Tv is the virtual temperature.

It is important to use virtual temperature to account for the variation in air density due to humidity. Virtual temperature is given by

$$Tv \cong (1 + 0.61w)T \quad (2-13)$$

where

- w is the mixing ratio (kg water vapor/kg dry air)
- T is the temperature of the parcel
- the approximation is due to the fact that we use mixing ratio instead of specific humidity as a measure of water vapor content.

Using a central finite difference scheme, the model solves for the vertical position of the parcel at the end of each time step. The horizontal wind components are used to update the horizontal position of the parcel. Parcel temperature is updated by solving for the wet or dry adiabatic lapse rates depending on whether the parcel is saturated or unsaturated, respectively. The dry adiabatic lapse rate is

$$\Gamma_{\text{dry}} = -(dt/dZ)_{\text{unsat}} = g/c_p \quad (2-14)$$

where

- g , the gravitational acceleration, is a function of height
- c_p is the specific heat at constant pressure.

This equation assumes that there is no heat transfer between the parcel and the surrounding environment and that the parcel is in equilibrium with its surroundings.

The saturated adiabatic lapse rate accounts for the release of latent heat which accompanies condensation as the saturated parcel rises through the atmosphere. (Likewise, absorption of latent heat during evaporation on descent.) The saturation lapse rate can be stated approximately (Ref. 10) as a function of temperature, T , and saturation mixing ratio, w_s , from the following

$$\Gamma_{\text{wet}} = -(dt/dZ)_{\text{sat}} \cong g/c_p [1 + Lw_s/R_{\text{ma}}T] [1 + L^2w_s/c_p R_{\text{mw}}T^2]^{-1} \quad (2-15)$$

where

L is the latent heat of vaporization (a slowly varying function of temperature)

R_{ma} is the specific gas constant for dry air

R_{mw} is the specific gas constant for water vapor.

In addition to updating the parcel conditions at each time step, the model updates ambient conditions by interpolating directly from the input met data. After each parcel mixes with the ambient atmosphere (as described directly below), the model updates the parcel mixing ratio using the following

$$w_p = w_p + (w_{old} - w_{new}) \quad (2-16)$$

where

- w_p is the mixing ratio of the parcel
- w_{old} is the mixing ratio of the parcel at the previous time step
- w_{new} is the mixing ratio of the parcel at the current time step.

Finally, water content is calculated just before writing the parcels to the output array by multiplying the parcel mixing ratio by the density of dry air for a final value in units of g/m^3 .

Entrain Ambient Air

Up to this point we have not considered the effects of mixing with the environment on parcel convection. Mixing with the cooler drier environmental air reduces the parcel buoyancy and the maximum cloud top height. The first step required to mix cloud and ambient air parcels (as a part of the "update parcels" procedure) is to define the rate at which they mix. The CSSM calculates a two-dimensional field of entrainment rates using the two-dimensional horizontal cloud distribution. This procedure counts up all cloud filled gridpoints within a distance given by the "entrainment radius parameter" surrounding a gridpoint. The ratio of cloud-filled gridpoints to total gridpoints is a measure of how close or far the gridpoint of interest is to a cloud edge.

The CSSM uses a linear ramp from a minimum entrainment rate of 0.5 (50% turnover per 100mb) deep within the cloud to a maximum value of 2.5 (250% per 100 mb) at the cloud edge. The values of the maximum and minimum entrainment rates were estimated from an analysis of cumulus data (see Section 2-3). Of course, as with all parameter values in the model, these values are subject to change with continued data analysis.

Both temperature and mixing ratio are updated to account for the effects of entrainment. Both are calculated as the weighted average of the parcel and ambient air conditions as follows

$$T_p = (m_p T_p + m_a T_a) / (m_p + m_a) \quad (2-17)$$

$$w_p = (m_p w_p + m_a w_a) / (m_p + m_a) \quad (2-18)$$

where

T_p is the temperature of the parcel after entrainment

T_p is the temperature of the parcel before entrainment

w_p is the mixing ratio of the parcel after entrainment

w_p is the mixing ratio of the parcel after entrainment

m_p and m_a are the mass of the parcel and the entrained air, respectively.

After the parcel “dries out” by this entrainment process, more water must evaporate to keep the parcel saturated. The evaporation serves to cool the parcel even further through absorption of latent heat. Thus, entrainment has a double effect on decreasing the temperature (and thus the buoyancy) of a parcel: first, the parcel cools due to mixing with cooler air and second, the parcel cools due to resaturation.

Evaluate Parcel Field

For each output time, the CSSM evaluates all saturated parcels on the output grid. Parcel position is converted to the output grid domain and the model then loops through all gridpoints falling within each parcel’s boundaries. The final water content value at each output gridpoint is defined to be the average of all overlapping parcels.

In a previous version of the model, we calculated a Gaussian mass distribution within each parcel and the resulting drop-off in water content from the center of the parcel to the edge. This technique resulted in only slightly different final results at significantly greater processing effort, and we therefore decided to implement the more efficient averaging scheme in this version of the model.

2.1.4.5 Structured Cloud Types

Structured cloud features such as cloud streets and mountain and lee wave orographic clouds are generated in the CSSM by modifying the underlying RSA field for the cloud type of interest with parameterized wave functions that create the desired structure. The algorithms employed make use of the input atmospheric profile and climatological values to determine the wave function parameters such as wavelength, amplitude, and damping.

2.1.4.5.1 Cloud Streets

Cloud streets develop in nature under conditions of relatively strong winds and neutral stability and commonly consist of stratocumulus cloud types aligned in the direction of the mean wind. Feteris (Ref. 11) examined the spacing between cloud streets and between cloud elements by using LANDSAT observations with Kuettner's (Ref. 12) theory of banded clouds. Feteris et al. (Ref. 11) reported the following relationship between the spacing between cloud streets (λ_x) and the cloud depth (H):

$$\lambda_x = \varepsilon * H; 0 < \varepsilon < 3.0 \quad (2-19)$$

They also found that the ratio of the distance between streets to the spacing between cloud elements within a street (λ_y) is:

$$1.2 < \lambda_x / \lambda_y < 4.0 \quad (2-20)$$

Choosing a typical case with $H = 2.0$ km and $\varepsilon = 1.5$ yields a street spacing, λ_x , of 5 km and an element spacing, λ_y , of 3 km.

The algorithm employed to generate cloud streets makes use of the above characteristics of cloud streets. Cloud streets are generated by adding a combination of sine and cosine waves to an initial RSA field generated for stratocumulus clouds. The sine wave determines the position and structure of the cloud streets, and the cosine wave determines the position and structure of the cloud elements within the streets. We use the typical "wavelengths" of 5 km and 3 km described above for the sine (street) and cosine (element) waves, respectively.

To simplify the geometry of the problem, the calculations are performed on a grid system rotated so that the abscissa is perpendicular to the mean wind direction. That is:

$$\begin{aligned} x' &= x \cos(\alpha) + y \sin(\alpha) \\ y' &= -x \sin(\alpha) + y \cos(\alpha) \end{aligned} \quad (2-21)$$

where (x,y) are the gridpoint coordinates in the original coordinate system
(x',y') are the gridpoint coordinates in the rotated coordinate system
 α is the angle of rotation determined by the mean wind direction, dd, and is given by:

$$\alpha = \begin{aligned} &180 - dd; dd \leq 180^\circ \\ &360 - dd; dd > 180^\circ \end{aligned}$$

The cloud street generating function is expressed in the rotated coordinate system by the following formula:

$$S = -1 + [\sin(2\pi x'/\lambda_x) + 0.4 \cos(2\pi y'/\lambda_y + P_s)] \quad (2-22)$$

The parameters are:

λ_x – inter-street wavelength (5000 m as described above)

λ_y – inter-element wavelength (3000 m as described above)

P_s – a randomly generated phase shift ($-\pi < P_s < \pi$) incorporated to vary cloud element positions between cloud streets.

The resultant RSA field used to generate the cloud streets is then given by:

$$RSA_s = RSA + S \quad (2-23)$$

where

- RSA_s is the modified RSA field used to generate cloud streets
- RSA is the original RSA field for stratocumulus clouds
- S is the street generating function described above.

Figure 12 shows a cloud street scene for a scenario with a southeasterly mean wind direction.

2.1.4.5.2 Orographic Clouds

Orographic clouds develop when air is lifted above the lifting condensation level by direct lifting over a topographic barrier or by wave motions downwind from such a barrier. Orographic clouds often form in relatively stable conditions and as a result are frequently laminar or stratiform in appearance.

Orographic cloud features are generated in the CSSM by adding a damped sinusoidal wave function to an initial RSA field generated for stratiform clouds. The generation of orographic clouds requires two steps. The first step processes user-provided information about the position of the ridge axis and the height of the ridge. The second step uses the processed ridge information in conjunction with meteorological information to generate the damped sinusoidal wave function used to generate the orographic clouds.

Ridge Information Processing

The user provides a few coordinates along the ridge axis as input if orographic clouds are desired. The user-defined ridge axis is used to construct a new set of ridge axis

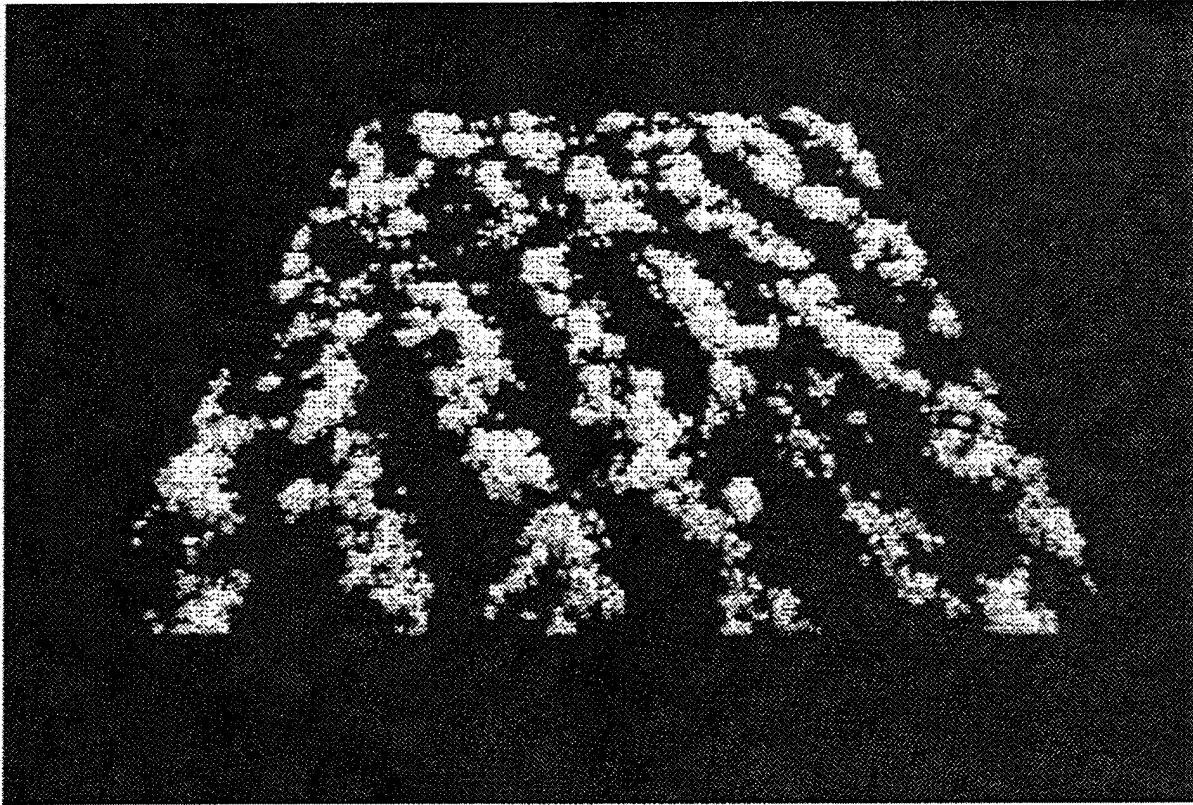


Figure 12 Cloud Street Scene

locations at a resolution 10 times greater than that input. This high-resolution ridge axis is then smoothed using a seven-point smoothing operator. The resultant smoothed, high-resolution ridge axis is used in the generation of the orographic clouds. The height of the ridge is taken to be the mean of the user supplied ridge heights at each ridge axis location.

Wave Function

The modulating function is calculated at each grid point and is expressed by the following formula:

$$W = A \sin(2\pi d/\lambda) \exp(-(1 - F)d/\lambda) \quad (2-24)$$

The parameters are described below after introducing a few definitions. (Refer to Figure 13).

g - acceleration of gravity

Γ_d - dry adiabatic lapse rate ($9.767 \cdot 10^{-3}$ K/m)

H - mean ridge height

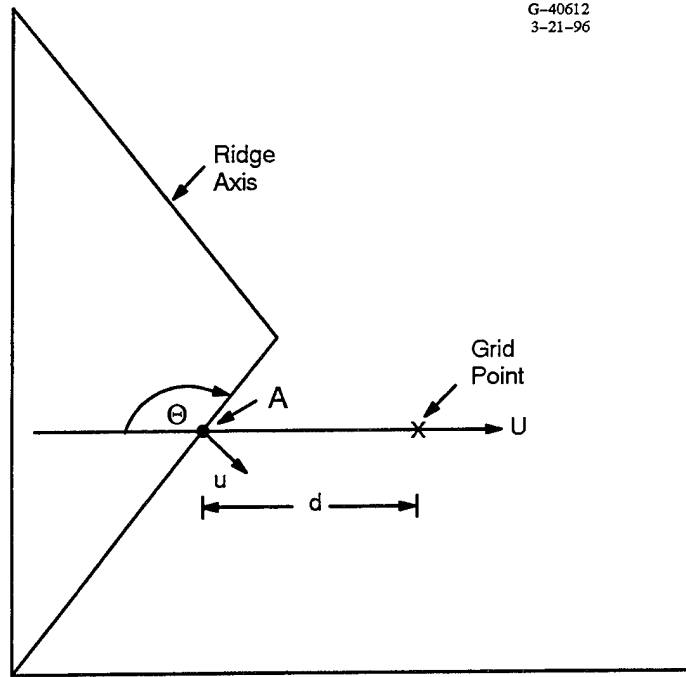


Figure 13 Schematic Showing Orographic Wave Processing Geometry

Γ_e – environmental lapse rate between $z=0$ and $z=H$

Γ_e' – environmental lapse rate between $z=H$ and $z=1.5*H$

U – mean wind averaged between $z=0$ and $z=H$

d – distance between grid point and ridge measured along the mean wind vector U

u – component of mean wind perpendicular to the ridge axis at point where mean wind vector through grid point intersects ridge axis (Point A in Figure 13)

θ – angle between the mean wind vector and ridge axis

The wave amplitude, A , defined by the following parametric relationship:

$$A = 4.0(H/10000)^{1/3} \sin(\theta) \quad (2-25)$$

This relationship produces wave amplitudes that are directly related to ridge height and the wind incidence angle as is observed in nature.

λ is the wavelength defined by the following relationship:

$$\lambda = 2\pi u / N \quad (2-26)$$

Where N is the Brunt-Vaisala frequency defined as:

$$N = \{(g/TBAR) (\Gamma_d - \Gamma_e)\} \quad (2-27)$$

$TBAR$ and Γ_e , the average temperature and environmental lapse rate, respectively, are calculated using the temperatures at $z=0$ and $z = H$.

We impose a minimum wavelength of 2000 m to eliminate spurious, unrealistic ripples that result when the wind is nearly parallel to the ridge axis.

F is a stability factor defined as:

$$F = \Gamma_e' / (6.5 \cdot 10^{-3} \text{ K/m}) \quad (2-28)$$

Γ_e' is calculated using the temperatures at $z=H$ and $z=1.5H$, the layer in which upward wave motions will be damped.

For stable atmospheric conditions (i.e. $F < 0$) we limit the orographic cloud structures to cap clouds by adjusting the amplitude to 6, and by setting F to -10 to produce the damping necessary to eliminate downstream waves.

The resultant RSA field used to generate the orographic clouds is then given by:

$$RSA_w = RSA + W \quad (2-29)$$

where

- RSA_w is the modified RSA field used to generate orographic clouds
- RSA is the original RSA field for stratocumulus clouds
- W is the street generating function described above.

Figure 14 shows a sample orographic cloud scene for a scenario with a north-south oriented V-shaped ridge with a westerly wind flow.

2.1.5 Cloud Model Results

In this section, we present several examples of CSSM cloud model results as visualized with the Quick-Look cloudviewer. The purpose of these scenes is to demonstrate some

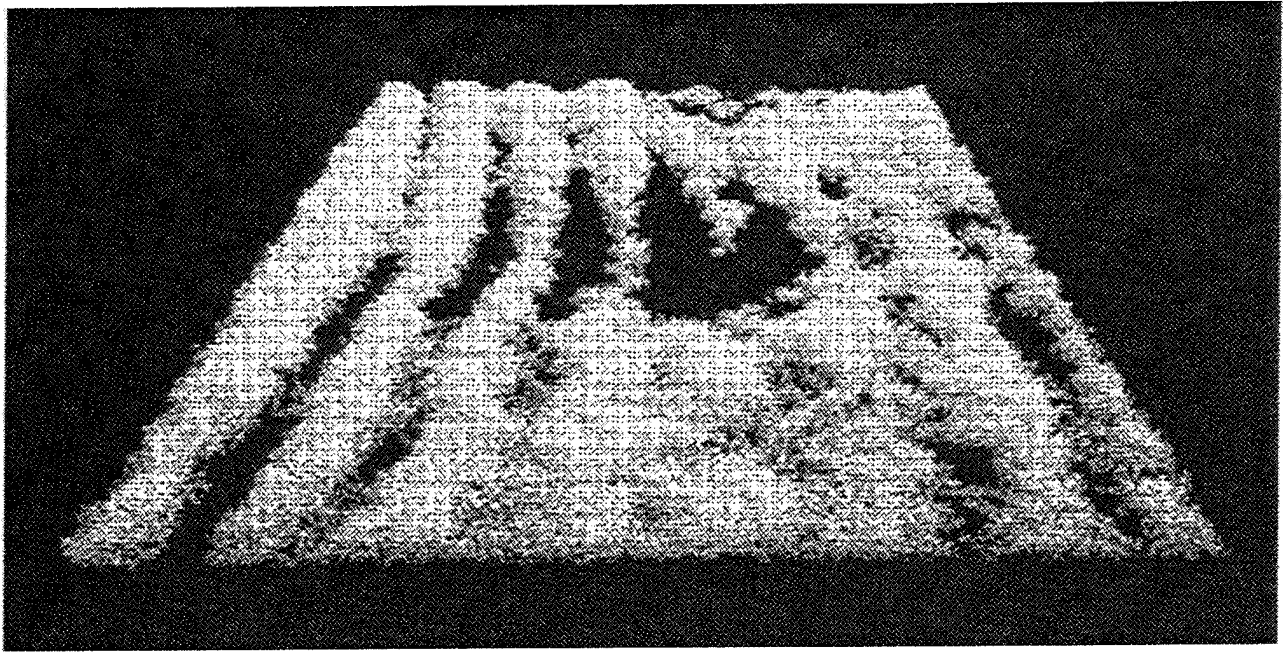


Figure 14 Orographic Wave Cloud Scene

of the model's capabilities to simulate a wide variety of cloud types and scenes. Two examples of CSSM output were presented in the previous section — a cloud street scene and an orographic wave cloud scene.

Figure 15 presents a stratus cloud scene. The model resolution for the simulation which produced this scene was 100 m. The model domain was set at 10 km x 10 km in the horizontal and 3 km in the vertical. The imposed large-scale cloud input for this simulation specified a 70% stratus cloud cover between 1000 m and 1500 m.

Figure 16 demonstrates the CSSM's ability to simulate multiple cloud layers. In this simulation the large-scale cloud input specified two cloud layers — a 45% stratocumulus streets cloud cover between 2000 m and 2600 m and an 80% cirrus cloud cover between 8000 and 9000 m. The resolution for this simulation was 200 m with a horizontal domain of 30 km × 30 km. The vertical domain extended to 10 km.

Figure 17 shows a cumulus cloud scene generated during the parameter estimation and tuning effort described in Section 2.3. In this case, the simulation was conducted with an input sounding representative of the area near Bethlehem, South Africa in late December. The input cloud information specified 70 % coverage of cumulus clouds. The resolution for the simulation was 100 m with a horizontal domain of 10 km x 10 km. The vertical domain extended to 8 km.

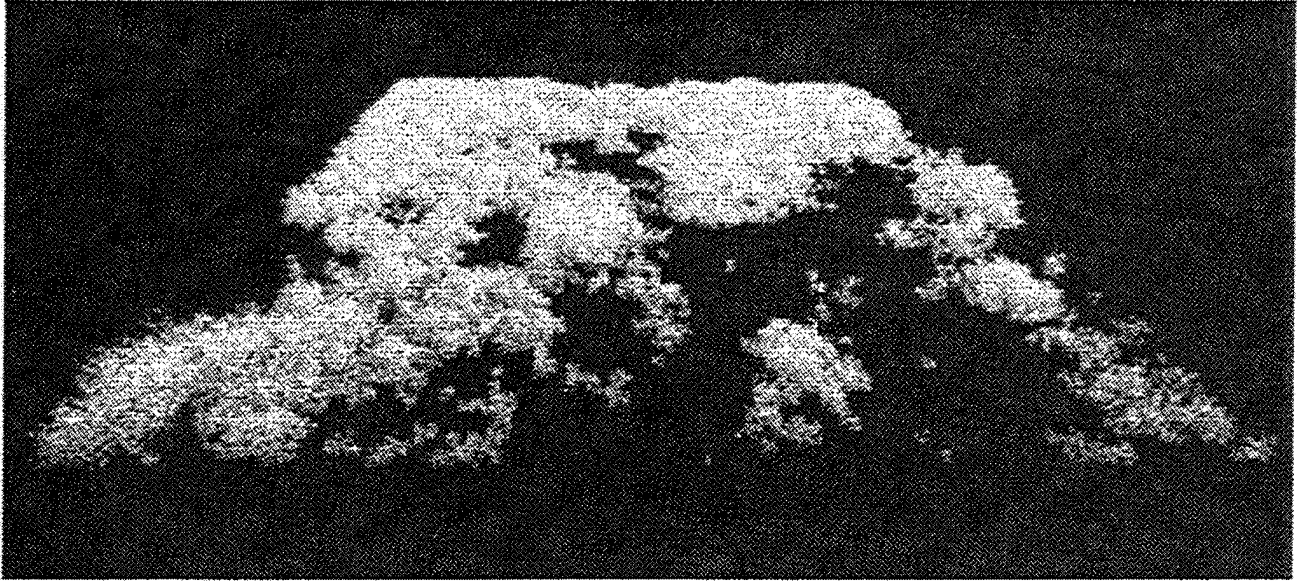


Figure 15 Stratus Cloud Scene

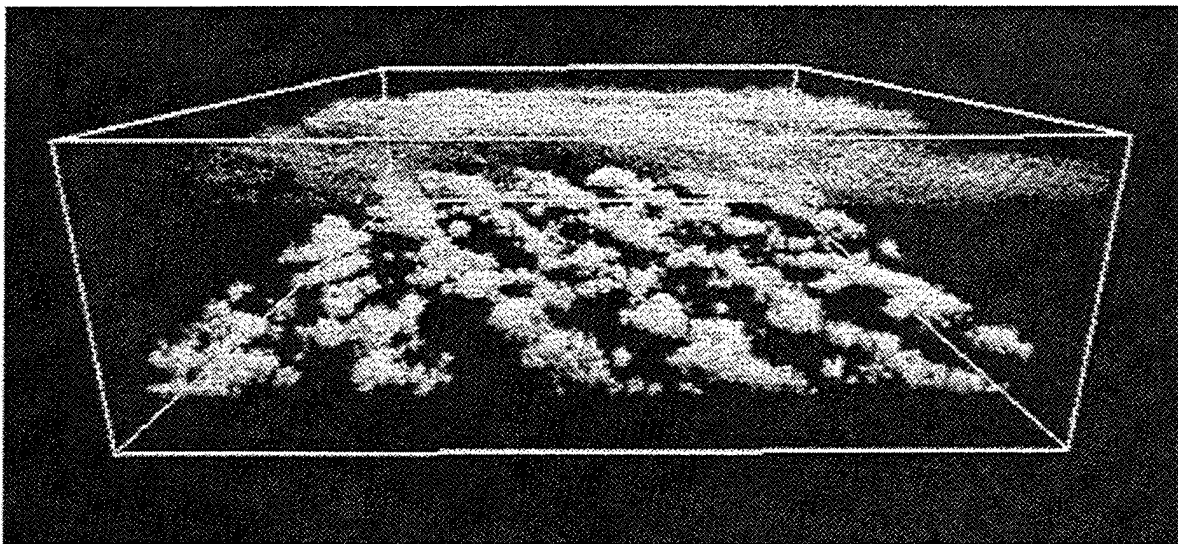


Figure 16 Layered Cloud Scene With Cirrus Over Cloud Streets

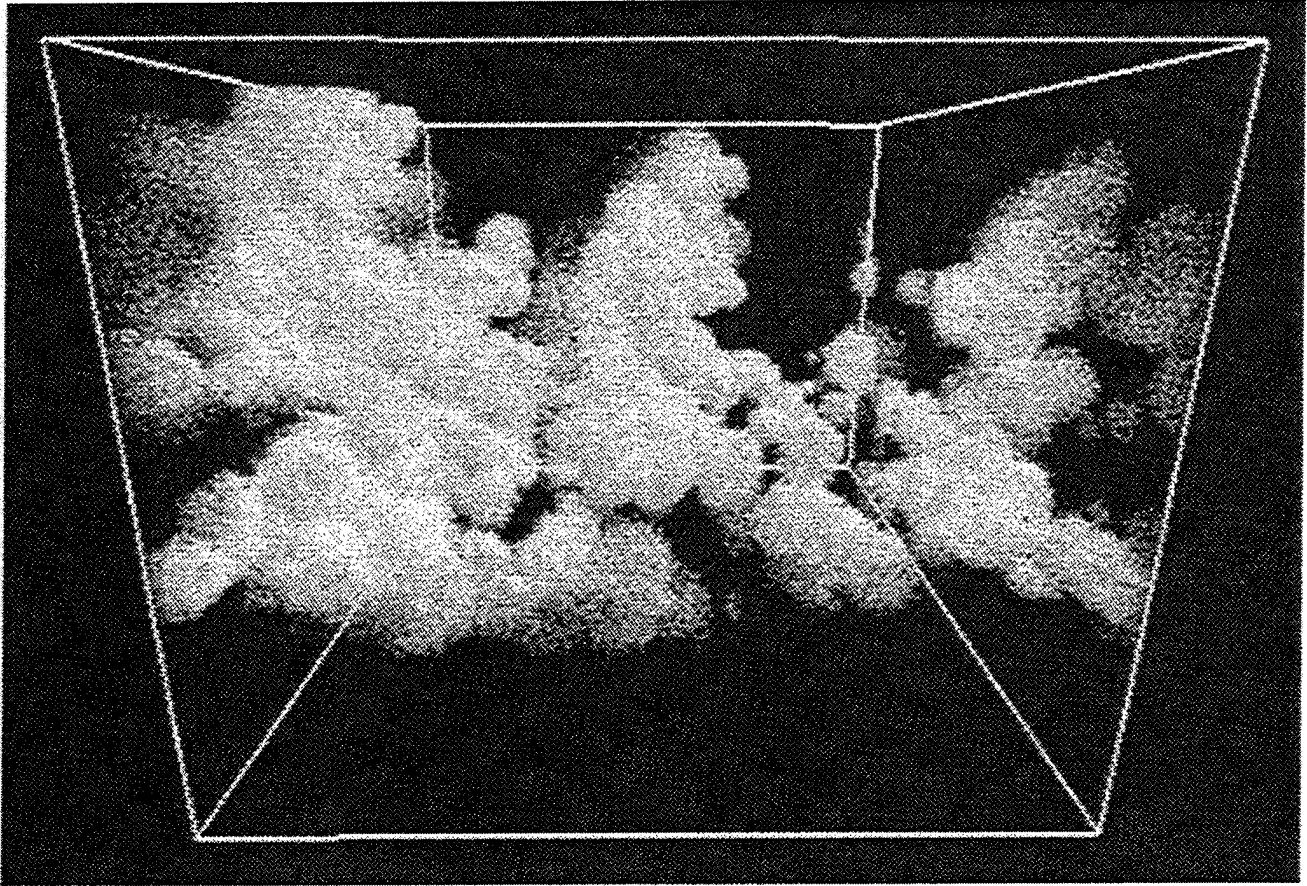


Figure 17 Cumulus Cloud Scene

2.2 THE RAIN MODEL

The precipitation model is used to simulate rain within the CSSM cloud fields. Precipitation in the CSSM currently refers to rain only, but snow, ice, and mixed precipitation models may be added in the future. Rain fields are generated for two different cloud types: nimbostratus and “precipitating cumulus.” We use the term precipitating cumulus instead of cumulonimbus to accentuate the fact that the model does **not** simulate thunderstorm-type clouds, including cumulonimbus. The stochastic methodology used in the CSSM is not appropriate for such dynamic cloud types. Therefore, the CSSM rain model should not be used for rain heavy storms.

2.2.1 Overview

Advanced simulation applications, now under development by members of the DoD community, will require high-fidelity atmospheric descriptions to enhance the realism of the training environment. Many systems used in the battlefield environment are affected by rain water that introduces background clutter, modifies ground mobility, decreases visibility, interferes with millimeter wave sensors, etc. The precipitation model described in this section takes a first step toward addressing these user requirements.

We've chosen a simple approach for this first implementation. The implementation allows for more complex techniques and algorithms to be added at a later date. The approach first separates liquid water content (LWC) into two portions, as outlined by Tattelman and Willis (Ref. 13). The first part is the cloud water content (CWC), made up of suspended water droplets with diameters up to 100 μm . The second part is the precipitation water content (PWC) that comprises the larger water droplets that fall out under the influence of gravity. Precipitation rates are derived from the PWC portion of the total LWC. The "rain_map" postprocessor determines the column-average in-cloud precipitation rates to provide the user with a gridded two-dimensional distribution of precipitation rates at the surface.

The first part of this section outlines the development of the algorithms used to convert the PWC to precipitation rate. The second part describes the generation of in-cloud precipitation rates for cumuliform and stratiform cloud types.

2.2.2 Development of Precipitation Rate Algorithms

There are two possible methods to derive precipitation rates from PWC. The first method is to convert the PWC to radar reflectivity, Z , and then use a Z - R relationship to convert the radar reflectivity to precipitation rate (R). The second method is to convert the PWC directly to precipitation rate.

The governing equations in finite differences form are:

$$Z = (\lambda^4/\pi^5 |K|^2) \sum_{i=1}^n \sigma(D_i) N(D_i) \Delta D_i, \quad (\text{mm}^6 \text{ m}^{-3}) \quad (2-30)$$

$$R = 6\pi \times 10^{-4} \sum_{i=1}^n D_i^3 v(d_i) N(d_i) \Delta D_i, \quad (\text{mm h}^{-1}) \quad (2-31)$$

$$PWC = ((\pi \times 10^{-3})/6) \sum_{i=1}^n D_i^3 N(D_i) \Delta D_i, \quad (\text{g m}^{-3}) \quad (2-32)$$

where

- i represents the drop size category
- D_i is the nominal drop size of the i^{th} category
- ΔD_i is the width of the i^{th} category
- $N(D_i) \Delta D_i$ is the number density of drops with $D_i - \Delta D_i/2 < D < D_i + \Delta D_i/2$.

In Eq. (2-30), $\sigma(D_i)$ is the backscattering cross section in mm^2 , λ (mm) is the radar wavelength, and $|K|^2$ is the refractory factor for water at the wavelength of the radar.

The drop size distributions can be measured by means of a disdrometer, which has a well defined cross-sectional sampling area capable of sorting drops into a finite number of size categories. The measurements obtained over a finite time interval can then be inserted into Eqs. (2-31) and (2-32) to obtain values for precipitation rate and PWC. To obtain a value of Z , knowledge of the radar wavelength and refractory factor for water at that wavelength is required.

Since the final goal is to obtain precipitation rates from PWC, it makes more sense to develop an empirical relationship between precipitation rate and PWC, instead of first converting PWC to Z values then using a Z -R relationship to obtain values of precipitation rates.

Data Sources

Most papers surveyed for this work emphasized development of either Z -R or Z -PWC relationships. Data sets to obtain a direct relationship between precipitation rate and LWC were found in two sets of works.

The first, much larger data set was obtained from four sites during the late 1950's and early 1960's (Refs. 14, 15, 16, 17). The second set of RR-PWC data was obtained in Illinois in 1982 (Ref. 18). In both sets of data, the PWC was exclusively liquid form only, and the measurements were made at the surface. There are other sources of data (Ref. 19) which deal with stratiform ice clouds done through airborne measurements.

The first data set was collected from four sites: Woody Island, Alaska; Long Beach, New Jersey; Franklin, North Carolina; and Miami, Florida. The data were obtained by a drop camera technique. Briefly, it consisted of a 70-mm camera and an optical system which sampled rainfall by taking photographs of the raindrops falling through a specific volume. A sample was collected once a minute during a precipitation event.

For measurement, the drop camera film was projected onto a translucent screen so that the drop images were twice their actual sizes. Two measurements were made of each drop image (the major and minor axes) by using electrical calipers designed specifically for this purpose. The measurements were translated into equivalent spherical diameter and were tabulated into a size frequency distribution for each cubic meter sample. The values for PWC, R, and Z are obtained using Eqs. (2-30) through (2-32) above.

The samples were classified by the synoptic weather type during which they were collected. Table 7 presents a brief description of each synoptic weather type during which samples were obtained and the data analyzed in this report.

The only drawback to this data set is the lack of detail beyond the broad synoptic descriptions of the weather during the sample taking. For example, air mass precipitation occurred many times during the almost 12-month period of data taking and the results were lumped together under one synoptic header. In actuality, there were differences in the conditions between each data set that have been lost in grouping the data.

The Illinois data set was obtained using a disdrometer. This is an electro-mechanical instrument developed by Joss and Waldvogel (Ref. 18). The instrument sorts drops into 20 size range bins from which the values for PWC, R, and Z are obtained using Eqs. (2-30) through (2-32). The entire data set was collected during one 3-hour interval under pre-cold frontal weather conditions.

**Table 7 Synoptic Weather Types for Which Observations
Were Obtained**

CODE	SYNOPTIC CONDITIONS	CLOUD DESCRIPTION
1	Air Mass	Precipitation that is produced by local convection within an unstable air mass. This precipitation is not associated with a front or instability line. The most frequent type is from well-developed cumulus clouds resulting from daytime heating. Thunderstorms were excluded wherever possible.
2	Pre-Cold Frontal	Precipitation is from a moist unstable air mass that is forcibly lifted. Precipitation is convective in nature and thunderstorms were included.
3	Post-Cold Frontal	Precipitation that is found behind a cold front and can be a combination of convective and stratiform types.
4	Overrunning	Precipitation is generally stratiform in nature. This condition usually associated with warm air ascending over a stationary front.
5	Warm Frontal	Precipitation is generally stratiform in nature. Obvious convective influences were discarded.
6	Warm Frontal Orographic	(Alaska) Precipitation occurred in warm frontal zone due to uplifting as well as being lifted orographically over hilly terrain.
7	Easterly Wave	Convective precipitation. Obvious thunderstorms were not included.
8	Cold Low	Precipitation associated with a mid latitude cyclone (not tropical in nature), characterized by stratiform precipitation.
9	Northeaster	(New Jersey) Stratiform precipitation associated with a synoptic scale low pressure (non tropical) area.

Results

The raw data from both data sets were sorted in a spread sheet program, by weather type and location and were analyzed using a statistical analysis package. Two different approaches were used in deriving a relationship between PWC and R. The first approach was to plot raw values of PWC and R for each synoptic type and obtain a best straight line fit relationship. The derived relationships were not sensitive to low values of PWC, creating large errors in the value of R. Since the values of R that will be encountered in the CSSM are typically associated with low values of PWC, these derived relationships are not satisfactory.

The second approach in deriving a relationship between PWC and R used the log values of PWC and R. The resulting derived relationships had the best fits for low values of R and PWC, making them more suitable for application to the CSSM. Also work done by Heysfield (Ref. 19) used log values to obtain relationships between small values of Ice Water Content (IWC) and R for stratiform ice clouds. The data set from Illinois was analyzed the same way. We noted in our analysis that the scatter of points in the Illinois set is less than the other sets.

There are two possible reasons for the larger scatter in the earlier data. First, the method used in collecting the earlier data was more manually intensive, requiring manual measurements of the drop sizes. This could be a possible source of errors in the results, since the collection of the Illinois data used a more sophisticated method of collecting data. The second reason for the larger scatter in the first data set may be due to the time intervals of the data sets. Data collection for the first set was over a period of up to 2 years, there would be some variations in same synoptic classes. Since the conditions are not identical each time that a particular synoptic feature was encountered, the slight differences added together would result in some scatter of points. The Illinois data has much less scatter because all the data was from one 3 hour period.

Table 8 lists the rain rate relationships as a function of PWC derived for each of the nine synoptic cases for both data sets. The Illinois data was collected for one synoptic case only, thus the single entry.

Conclusions

Since the results are very close between the two data sets for the pre-cold frontal synoptic case (#2), there is a high degree of confidence that the older data set gives good results. Therefore for cumuliform precipitation in the CSSM, the value for R obtained for the air mass synoptic case (#1 in the table) will be used to convert PWC to precipitation rates. For stratiform precipitation, the value for R for the warm frontal weather condition (#5 in the table) will be used.

Table 8 Rain Rates as a Function of LWC

SYNOPTIC CODE	DATASET #1	DATASET #2
1	$R = 19.86 * PWC^{1.298}$	
2	$R = 21.13 * PWC^{1.088}$	$R = 23.07 * PWC^{1.066}$
3	$R = 18.45 * PWC^{1.078}$	
4	$R = 20.94 * PWC^{1.129}$	
5	$R = 20.09 * PWC^{1.109}$	
6	$R = 29.24 * PWC^{1.308}$	
7	$R = 20.06 * PWC^{1.010}$	
8	$R = 21.63 * PWC^{1.149}$	
9	$R = 18.83 * PWC^{1.083}$	

2.2.3 In-Cloud Precipitation Rates

The CSSM produces three dimensional grids of LWC values which can be partitioned into CWC and PWC contributions. We seek a simple method to realistically separate the LWC into its components.

The most rigorous method would be to convert the LWC into a water droplet size distribution. Using a droplet diameter of 0.1 mm as the typical boundary between the two categories of hydrometeors (Ref. 13), the two quantities can be determined by integrating over droplet size on either side of the cutoff. Such a rigorous treatment is beyond the scope of the current project, but may be pursued at a later date.

A less rigorous solution is to use a constant threshold value to partition the LWC into its components. This method is a simplification of the Tattelman and Willis (Ref. 13) treatment where they vary the threshold by atmospheric height as well as by precipitation intensity.

Precipitating Cumulus Clouds

To show that using a constant threshold gives a reasonable result, consider the “sounding” of LWC values for a given x,y location from a CSSM LWC field shown in Table 9.

The first column is the height of the layer in meters, the second column is the simulated LWC value in g/m^3 , the third column is the PWC obtained by subtracting a value of 0.9 g/m^3 from the LWC. The choice of the value of 0.9 g/m^3 is discussed below. The fourth column is the precipitation rate in mm/hr computed using the algorithm for cumulus precipitation described in Section 2.2.2 with the value of PWC. The fifth column is the equivalent radar reflectivity in dBZ for the precipitation rate obtained in column four, using the Marshall-Palmer (Ref. 20) relationship, Eq. (2-33).

$$dBZ = 10[\log_{10} 200 * R^{1.6}] \quad (\text{mm}^6 \text{ m}^{-3}) \quad (2-33)$$

Table 9 Sample Computed LWC "Sounding"

HEIGHT (m)	LWC (g/m ³)	PWC (g/m ³)	R (mm/hr)	REFLECTIVITY (dBZ)
50	0.00	0.00	0.00	0
150	0.00	0.00	0.00	0
250	0.00	0.00	0.00	0
350	0.00	0.00	0.00	0
450	0.04	0.00	0.00	0
550	0.04	0.00	0.00	0
650	0.07	0.00	0.00	0
750	0.16	0.00	0.00	0
850	0.20	0.00	0.00	0
950	0.28	0.00	0.00	0
1050	0.51	0.00	0.00	0
1150	0.74	0.00	0.00	0
1250	0.74	0.00	0.00	0
1350	0.83	0.00	0.00	0
1450	0.87	0.00	0.00	0
1550	1.00	0.10	1.05	23
1650	1.02	0.12	1.28	25
1750	1.00	0.10	1.03	23
1850	1.03	0.13	1.46	26
1950	1.10	0.20	2.52	29
2050	1.16	0.26	3.53	32
2150	1.18	0.28	3.88	32
2250	0.00	0.00	0.00	0
2350	0.00	0.00	0.00	0

The choice of a threshold of 0.9 g/m^3 for splitting the LWC into the PWC and CWC was based on two factors. The first was based on the work by Tattelman and Willis (Ref. 13) on model liquid water content profiles. The second factor was comparisons to observational data. When the computed precipitation rates were converted into radar reflectivities, comparisons were made with actual radar reflectivity data obtained from cumulus clouds of the same height and structure (Ref. 21). By experimenting with different cutoff values, it was found that using the cutoff value of 0.9 g/m^3 when translated into radar reflectivities yielded values that were comparable to the observations.

An example of a cross-section through a volume of LWC values is shown in Figure 18. The outer contour in Figure 18 outlines the non-zero LWC values and has the shape typical of a cumuliform cloud. The inner contour surrounds areas of LWC values greater than the cutoff value of 0.9 g/m^3 . If that portion of the LWC greater than 0.9 g/m^3 ,

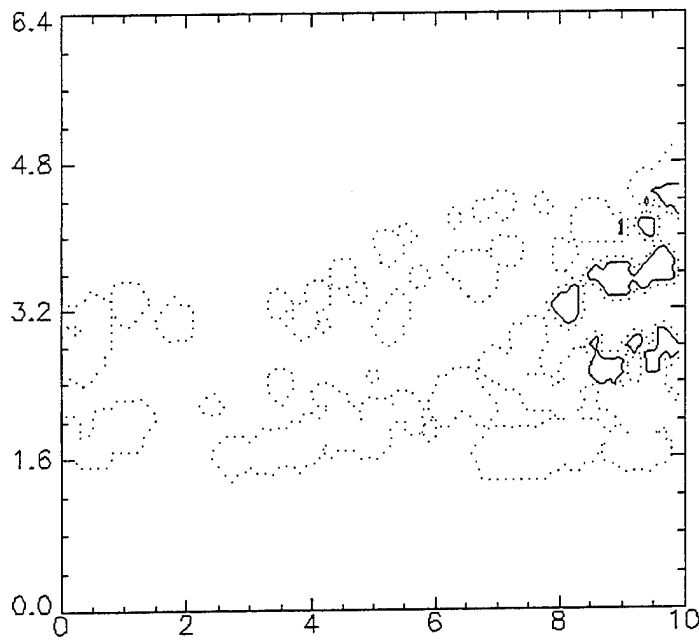


Figure 18 Cross-section of Model Output of Simulated Cumulus Cloud LWC Values. Dashed contour Denotes Cloud Edge. Solid Contour Surrounds LWC Values Greater Than the Cutoff Value of 0.9 g/m^3 . Both Axes Are Labeled in Kilometers.

denoting the PWC, is converted to precipitation rates, a spatial distribution of in-cloud precipitation rates can be constructed, Figure 19. The precipitation rates are contoured in increments of 2 mm/hr starting at 0 mm/hr .

Nimbostratus Clouds

The procedure outlined in the previous section for cumulus clouds is the same for stratus clouds, except for a different threshold value. The threshold value that partitions the LWC into CWC and PWC was obtained by trial and error. For each threshold value, the resulting PWC were converted first to precipitation rates then to radar reflectivities. The spatial distribution of these in-cloud radar reflectivities were then compared to actual radar reflectivity data of stratus clouds (Refs. 22, 23).

Figure 20 shows a slice through a simulated nimbostratus cloud LWC field. The outer contour outlines the non-zero values of LWC and has a shape characteristic of a stratiform cloud. The inner contour surrounds areas of LWC values greater than the cutoff value of 1.0 g/m^3 . When that portion of the LWC greater than 1.0 g/m^3 , denoting the PWC, is converted to precipitation rates, a spatial distribution of in-cloud precipitation rates can be constructed, Figure 21. The precipitation rates are contoured in increments of 2 mm/hr starting at 0 mm/hr .

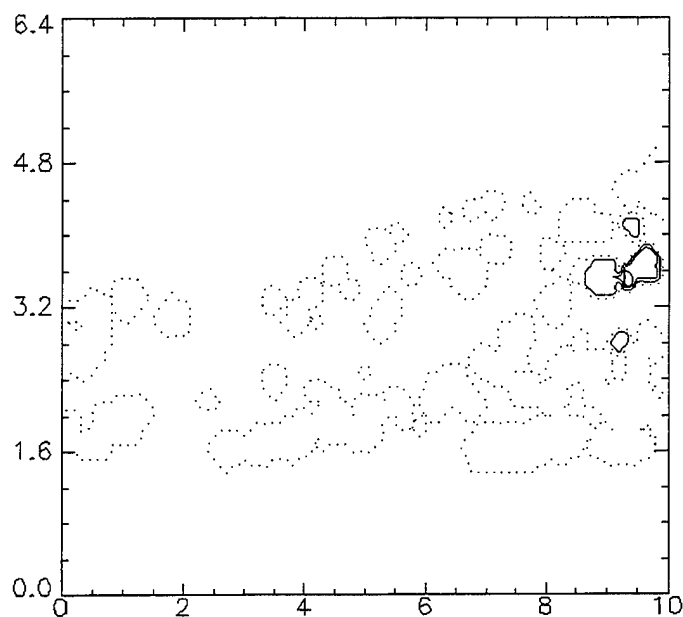


Figure 19 Precipitation Rates (Contoured Every 2 mm/hr Starting at 0 mm/hr) Derived from LWC Cross-section Shown in Figure 18. Both Axes are Labeled in Kilometers.

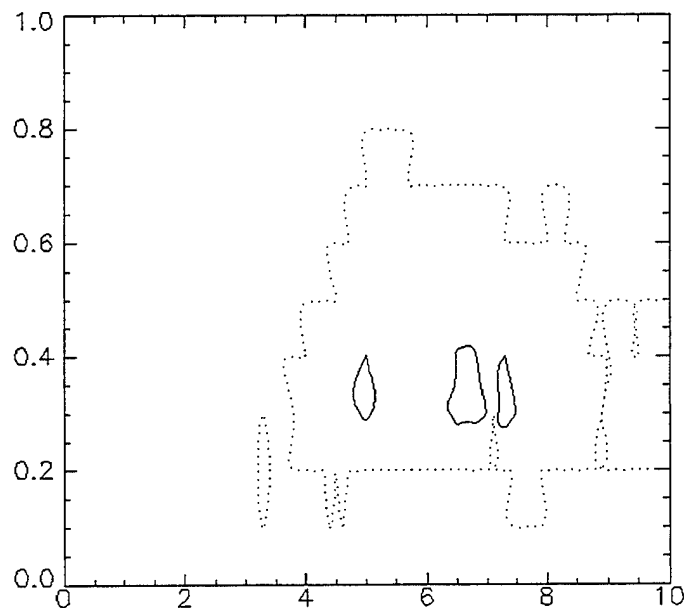


Figure 20 Cross-section of Model Output of Simulated Nimbostratus Cloud LWC Values. Dashed Contour Denotes Cloud Edge. Solid Contour Surrounds LWC Values Greater Than the Cutoff Value of 1.0 g/m^3 . Both Axes Are Labeled in Kilometers.

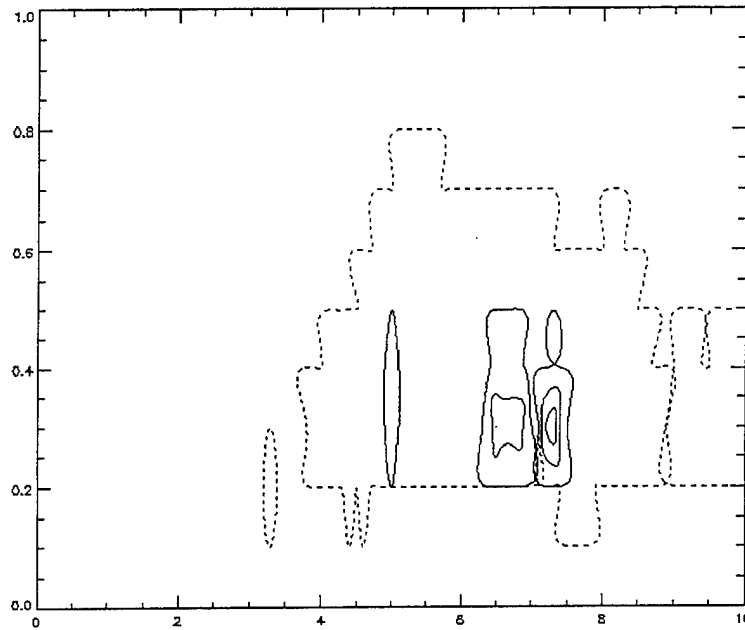


Figure 21 Precipitation Rates (Contoured Every 2mm/hr Starting a 0 mm/hr) Derived from LWC Cross-section Shown in Figure 20. Both Axes are Labeled in Kilometers.

2.2.4 Surface Precipitation Rate Algorithm

With the mechanism described above, the CSSM can convert LWC values into in-cloud precipitation rates. However, the above mechanism does not produce precipitation rates at the surface. We next discuss the technique used to estimate the surface precipitation rate from the in-cloud rates.

Our initial approach to estimate precipitation at the surface was the so-called “Cascade Model.” This model uses the in-cloud precipitation rates combined with an assumed terminal velocity to allow precipitation to fall to the surface. The “cascade” technique allows rain water to fall from cloud grid boxes into lower grid boxes during a succession of time steps. We discarded this technique because the prototype required a fixed model domain for all time steps. Since one of the major advances in this version of the CSSM is the option for moving domains, we felt it important to maintain that functionality. Modifying the “Cascade Model” to allow it to function properly with movable domains proved to be beyond the scope of this effort.

We chose instead to implement a simple scheme to estimate the surface precipitation rate. To simplify development, the scheme was implemented as a post-processor which operates on the CSSM precipitation rate output file. For each surface grid location,

we estimate the surface precipitation rate to be the average of the non-zero in-cloud precipitation rates in the column of grid boxes directly above the location. Table 10 illustrates the technique by showing a 2-D slice of in-cloud precipitation rates with the estimated surface precipitation rate shown along the bottom of the table.

We derived relationships between precipitation water content and precipitation rates from a variety of datasets. We found that the relationships were dependent upon the synoptic conditions under which the precipitation was produced.

Table 10 Sample Surface Rain Rate Calculation (Values in mm/hr)

We have developed a CSSM post-processor which uses the in-cloud precipitation rates to produce 2-D fields of surface precipitation rates. These rates can be used directly or integrated over time to produce accumulated precipitation values.

2.3 PARAMETER ESTIMATION AND CUMULUS MODEL VALIDATION

During the previous model development process for the PL/SWOE Cloud Scene Simulation Model we evaluated and estimated model parameters based on literature reviews and on visual comparison of model-produced and observed cloud fields for a limited number of cases. These comparisons provided base-line values for the various model parameters controlling the external cloud structure. In the current study, we use cloud liquid water content (LWC) measurements from several cloud types and locations to estimate internal LWC model parameter values. We also use an independent set of data to validate the selection of model internal LWC model parameters for cumulus cloud types.

This section describes our cloud LWC data collection effort and the data analysis methodology, the parameter estimation methodology and results, and the cumulus model validation methodology and results.

2.3.1 Cloud Liquid Water Content Data Collection and Analysis

Our literature search revealed three sources of cloud LWC and related information. We evaluated the FAA cloud database (formerly maintained by NRL) provided by Dr. Richard Jeck, a FIRE/ASTEX experiment dataset provided by Drs. Warren Wiscombe (NASA-Goddard) and Hermann Gerber, and the ECLIPS dataset containing LIDAR-derived cloud base and top information provided by Dr. David Winker (NASA-Langley).

The nature of our analysis required that any dataset we chose include at a minimum the following:

- High-resolution cloud LWC data (preferably one-second sampling)
- Information on cloud base height
- Information on temporal and spatial location of the sample.

The only data source that met all these criteria was the FAA cloud database. Based on this evaluation and on Dr. Jeck's willingness to provide us with data, we selected the FAA database as our data source.

All the evaluated data sources suffered from a lack of concurrent supporting meteorological data such as upper air soundings, surface observations, etc. We discuss in a later section our methodology to mitigate this weakness in the FAA data sets.

2.3.1.1 FAA Database Description

The FAA cloud database contains information on aircraft-based observations of cloud data obtained from various cloud measurement experiments. The database lists data sets containing a variety of cloud-related variables along with averaged cloud data based on those data sets. The information available from the database allowed us to select a number of data sets for use in the parameter estimation and cumulus model validation effort.

The database contains information about the mission flight, cloud systems, prevailing weather, and measurement-related factors for each available data set. Mission identifier variables include date, time, measuring agency, experiment name, geographical location, and surface elevation. The cloud information variables include cloud type, cloud group, cloud identification number, prevailing cloud distribution, cloud base and top heights, and temperatures of cloud base and top. Weather variables include air mass information and coded descriptions of the weather conditions associated with the clouds under study. Measurement-related variables include the time duration of the data set sample, the distance traveled by the aircraft, and the state of the cloud particles sampled (water droplets, ice crystals, or both). The database also contains averaged variables such as airspeed, altitude, air temperature, LWC (g/m^3) indicated by a hot-wire meter (Johnson-Williams [JW] or CSIRO-King), and/or the LWC computed from the droplet size distribution indicated by the FSSP (Forward Scattering Spectrometer Probe).

The FAA cloud database includes datasets of varying quality in a variety of formats (from paper copies to electronic data files in tabular ASCII text). Some datasets contain only time-averaged LWC values and many do not include the location or cloud base height information necessary for this study. None of the datasets in the database contain concurrent supporting meteorological data.

The datasets we considered for analysis met several criteria:

- Available in electronic format
- Provide actual one-second time series JW and FSSP LWC values
- Provide date, time, altitude, geographical location or aircraft heading, and airspeed

- Provide information on cloud base heights
- Contain long paths through clouds.

Midway through the data collection effort Dr. Jeck’s ability to provide data was substantially reduced by his commitment to high-priority FAA projects. As a result of this constraint, we chose to limit our parameter estimation effort to two cloud types: cumulus and stratus. We also chose to limit our validation effort to cumulus clouds. Our focus on cumulus clouds was driven by three factors. First, the most substantial changes to the CSSM since the PL/SWOE version’s release have been made in the cumulus model code. Second, the greatest LWC variability is expected in cumulus clouds. Finally, the FAA database contains more suitable datasets with greater geographical variability for cumulus clouds than for other cloud types.

We requested and processed 25 cloud datasets. Of these, ten contained usable paths through cumulus clouds, and three contained usable paths through stratus clouds. The remaining 12 datasets were excluded for several reasons including: insufficient path lengths, cloud types (e.g., cumulonimbus) not included in this study, and insufficient or inconsistent LWC data. Table 11 provides a summary of the 13 data sets used in this study. We labeled the datasets A through Y for internal tracking. This naming convention will be used through the following discussion.

2.3.1.2 Spatial Series Data Selection

The 13 sets of LWC and position data were analyzed to find uniform, continuous paths through clouds. Our analysis consisted of the following steps:

- Identify continuous time series (i.e. series with time gaps of less than 5 seconds) at least 45 seconds long
- Analyze aircraft altitude and horizontal position data to determine path type (e.g., straight and level, slant, curved and level, etc.)
- Evaluate LWC data quality.

Table 12 provides a summary of all the paths selected based on the first two criteria above. We eliminated the paths (labelled NOT USED) that contain insufficient LWC data, inadequate data quality, slant paths, or cloud types not appropriate for this study.

Table 11 Summary of Datasets Used in This Study

DATASET	EXPERIMENT	DATE	LOCATION	SENSORS	START TIME (GMT)	STOP TIME (GMT)
A	CCOPE	4 Jun 1981	MILES CITY MONTANA	F & J	2109	2142
C	CCOPE	11 Jul 1981	MILES CITY MONTANA	F & J	2132	2210
E	CCOPE	1 Jun 1981	MILES CITY MONTANA	F & J	2013	2302
F	CCOPE	15 Jun 1981	MILES CITY MONTANA	F & J	1933	2141
G	CCOPE	19 Jul 1981	MILES CITY MONTANA	F & J	2145	2354
H	BPRP	27 Nov 1984	BETHLEHEM S.AFRICA	J	1435	1440
I	BPRP	21 Feb 1986	BETHLEHEM S.AFRICA	J	1221	1640
K	LANDES FRONTS	5 Jun 1984	GASCOGNE PRV FRANCE	F & J	1412	1456
O	CCOPE	19 Jul 1981	MILES CITY MONTANA	F & J	1734	1840
P	CCOPE	20 Jun 1981	MILES CITY MONTANA	F & J	1814	1944
W	CASP:1986	18 Feb 1986	HALIFAX NOVA SCOTIA	F & J	1750	1803
X	CASP:1986	18 Feb 1986	HALIFAX NOVA SCOTIA	F & J	1805	1815
Y	CASP:1986	18 Feb 1986	HALIFAX NOVA SCOTIA	F & J	1815	1822

The excellent supplementary documentation (described in a later section) available for the 20 June 1981 dataset led us to select paths from dataset "P" for use in the cumulus model validation. The benefits provided by the supplementary documentation outweigh the limitations imposed by the fact that most of these "validation" paths do not meet the series length criteria described above.

Table 12 Selected Paths

DATA	LOCATION	DATASET	SERIES	CLOUD TYPE	LENGTH (SEC)	ALT (FT)	BASE (FT)	TOP (FT)
6/4/81	MILES CITY MT	A	1	TCU	48	16100	8300	18000
			2	TCU	61	15270	8300	18000
			3	NOT USED				
			4	TCU	65	15100	8300	18000
			5	NOT USED				
			6	TCU	80	15180	8900	18000
			7	TCU	105	15180	8900	18000
7/11/81	MILES CITY MT	C	1	CU	45	21130	15300	24000
			2	CU	71	19135	15300	24000
			3	CU	67	16060	15300	24000
			4	NOT USED				
6/1/81	MILES CITY MT	E	1	NOT USED				
			2	CU	86	13115	NA	15000
			3	TCU	48	13265	NA	NA
			4	TCU	73	13070	NA	NA
			5	NOT USED				
			6	NOT USED				
			7	TCU	106	12245	NA	NA
			8	NOT USED				
			9	TCU	78	13085	NA	NA
			10	NOT USED				
			11	TCU	80	13290	NA	NA
			12	TCU	87	13240	NA	NA
			13	TCU	80	13170	NA	NA
			14	TCU	94	13145	NA	NA
			15	NOT USED				
6/15/81	MILES CITY MT	F	1	NOT USED				
			2	CU CON	74	16240	NA	NA
			3	NOT USED				

Table 12 Selected Paths (continued)

DATA	LOCATION	DATASET	SERIES	CLOUD TYPE	LENGTH (SEC)	ALT (FT)	BASE (FT)	TOP (FT)
			4	CU CON	79	16250	NA	NA
			5	CU CON	117	16255	NA	NA
			6	CU CON	145	15230	NA	NA
			7	CU CON	86	15265	NA	NA
			8	NOT USED				
			9	NOT USED				
7/19/81	MILES CITY MT	G	1	CU	48	19250	NA	NA
			2	CU CON	46	19700	12800	NA
			3	CU	44	18195	NA	NA
			4	CU	48	18100	NA	NA
11/27/84	BETHLE-HEM SA	H	1	CU CON	53	20575	10000	NA
			2	CU CON	52	20685	10000	NA
2/21/86	BETHLE-HEM SA	I	1	TCU, CON	58	20135	NA	NA
			2	TCU, CON	51	20195	NA	NA
			3	TCU, CON	59	20030	NA	NA
			4	TCU, CON	55	20300	NA	NA
			5	TCU, CON	48	20220	NA	NA
			6	TCU, CON	72	20240	NA	NA
			7	TCU, CON	45	21555	NA	NA
			8	TCU, CON	52	21560	NA	NA
			9	TCU, CON	46	20670	NA	NA
			10	TCU, CON	56	20250	NA	NA
			11	TCU, CON	57	20630	NA	NA
			12	TCU, CON	73	20710	NA	NA
			13	TCU, CON	87	20740	NA	NA
6/5/84	GAS-COGNE PROV FR	K	1	CU CON	76	12610	3200	NA
			2	CU CON	172	8945	3200	NA
			3	NOT USED				
			4	NOT USED				
7/19/81	MILES CITY MT	O	1	NOT USED				
			2	CU	69	14080	11200	NA

Table 12 Selected Paths (continued)

DATA	LOCATION	DATASET	SERIES	CLOUD TYPE	LENGTH (SEC)	ALT (FT)	BASE (FT)	TOP (FT)
			3	CU	46	14085	11200	NA
			4	CU	54	14015	11200	NA
6/20/81	MILES CITY MT	P	1	CU	25	9300	NA	NA
			2	CU	31	9160	NA	NA
			3	CU	37	14150	NA	NA
			4	CU	29	19000	NA	NA
			5	CU	31	16190	NA	NA
			6	CU	25	18220	NA	NA
			7	CU	37	18990	NA	NA
			8	CU	27	17360	NA	NA
			9	CU	23	18270	NA	NA
			10	CU	23	16130	NA	NA
2/18/86	HALIFAX NS	W	1	ST	61	7200	3600	7400
	HALIFAX NS		2	ST	70	7101	3600	7400
	HALIFAX NS		3	ST	82	7101	3600	7400
	HALIFAX NS		4	ST	66	7118	3600	7400
	HALIFAX NS		5	ST	55	7052	3600	7400
	HALIFAX NS		6	ST	85	7052	3600	7400
2/18/86	HALIFAX NS	X	1	ST	271	7036	3600	7400
	HALIFAX NS		2	ST	208	7068	3600	7400
2/18/86	HALIFAX NS	Y	1	ST	208	7036	3600	7400
	HALIFAX NS		2	ST	208	7036	3600	7400

2.3.1.3 Cloud Model Test Cases

We first categorized the selected set of paths by cloud type. We categorized the cumulus cloud paths by their collection location: Miles City, Montana during the Cooperative Convective Precipitation Experiment (CCOPE); Bethlehem, South Africa during the Bethlehem Precipitation Research Project (BPRP); and Gascogne Province, France during the Landes Fronts Experiment. The stratus cloud paths were all collected near Halifax, Nova Scotia during the Canadian Atlantic Storms Project (CASP) experiment. The CASP data was provided to Dr. Jeck by the Atmospheric Environment Service (AES) of Canada. We based our final categorization of the cloud paths on the height of the observation above the cloud base. The heights were categorized in increments of 1000 meters above cloud base.

Basic statistics were calculated for the LWC observations in each of the paths. In addition to calculating statistics such as the mean LWC and standard deviation, we also estimated the correlation length in the following manner. First, the autocorrelation function was calculated for the LWC series in each path. The sample autocorrelation function is defined as:

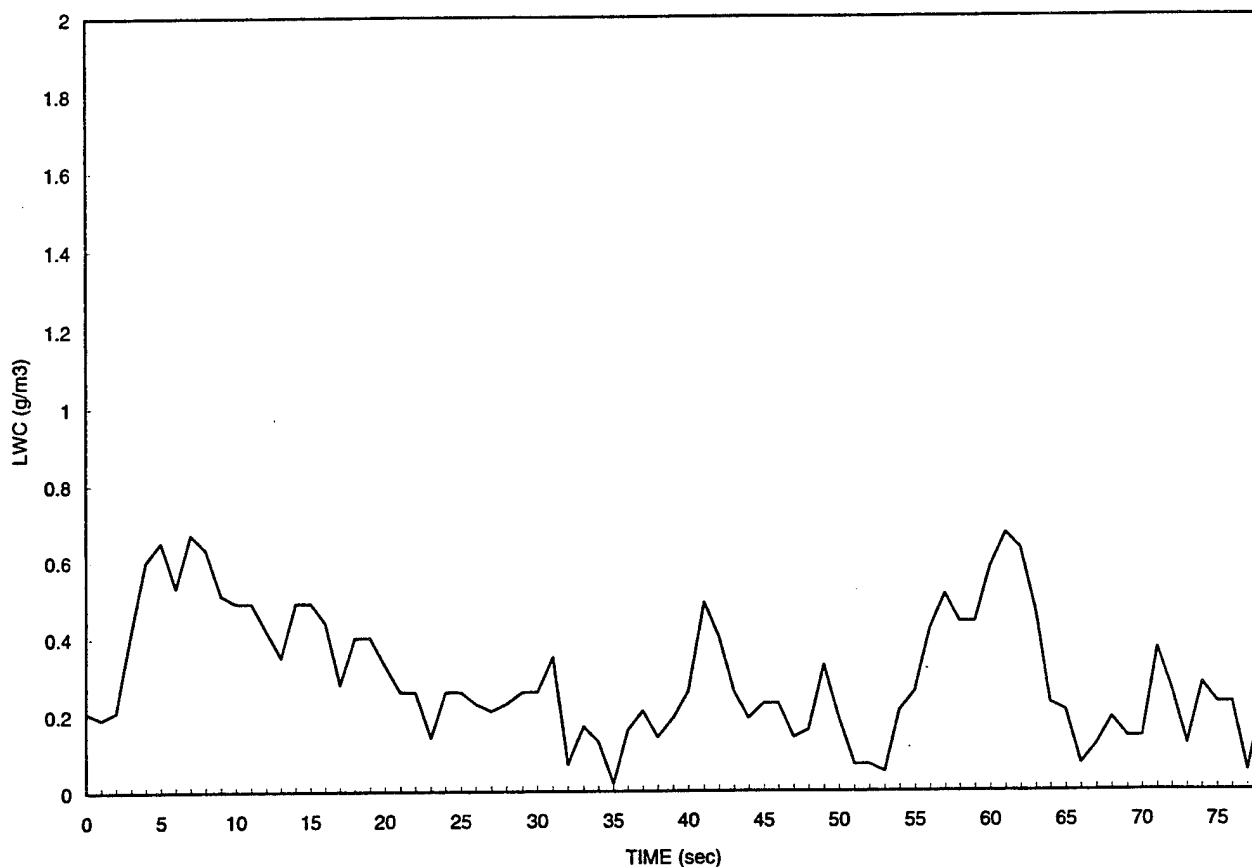
$$ACF(lag) = \frac{1}{\sigma^2} \frac{1}{N} \sum_{t=lag+1}^N (lwc_t - \langle lwc \rangle)(lwc_{t-lag} - \langle lwc \rangle) \quad (2-34)$$

where:

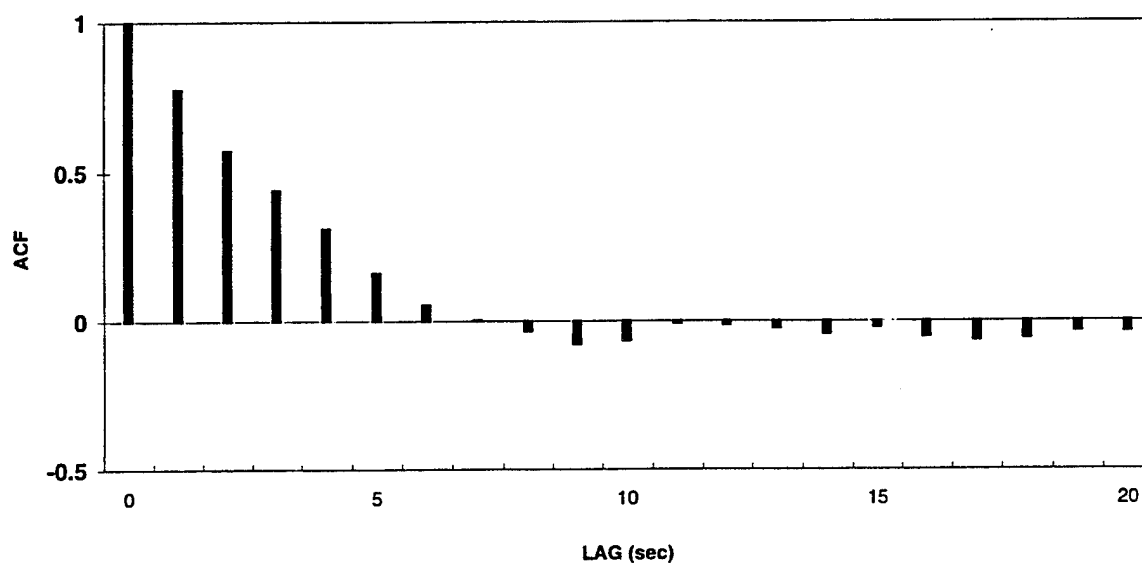
- σ^2 = variance in sample data
- N = number of data points in the series
- $\langle lwc \rangle$ = mean liquid water content
- t = time (space) index

We estimated the correlation length as the lag at which the autocorrelation function first becomes zero.

Figure 22, Figure 23, Figure 24 and Figure 25 show LWC time series and corresponding autocorrelation functions for several paths. Table 13 shows the LWC statistics calculated for each of the paths used in the parameter estimation effort (statistics for the "validation" paths are presented later).

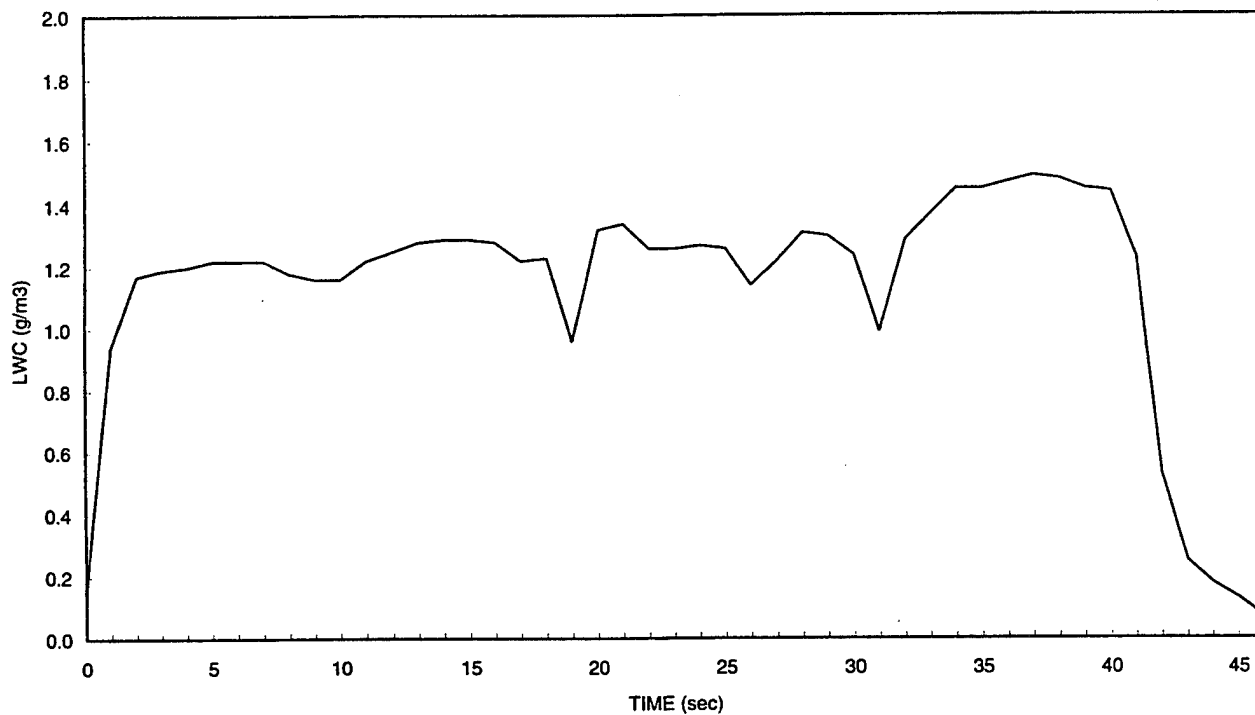


(a)

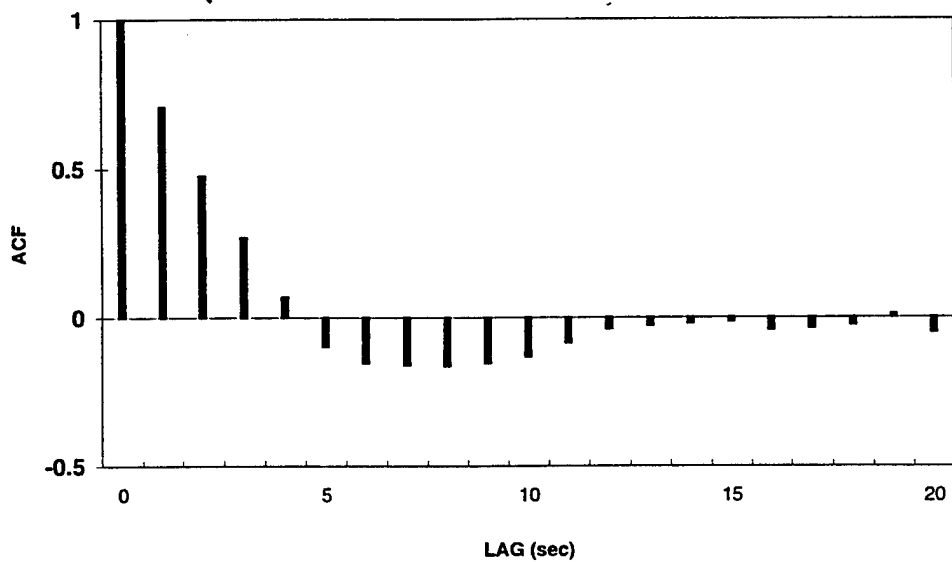


(b)

Figure 22 Time Series of LWC in g/m^3 (Panel A) and Autocorrelation Function (Panel B) for Observed Path E9 through Montana Cumulus Cloud

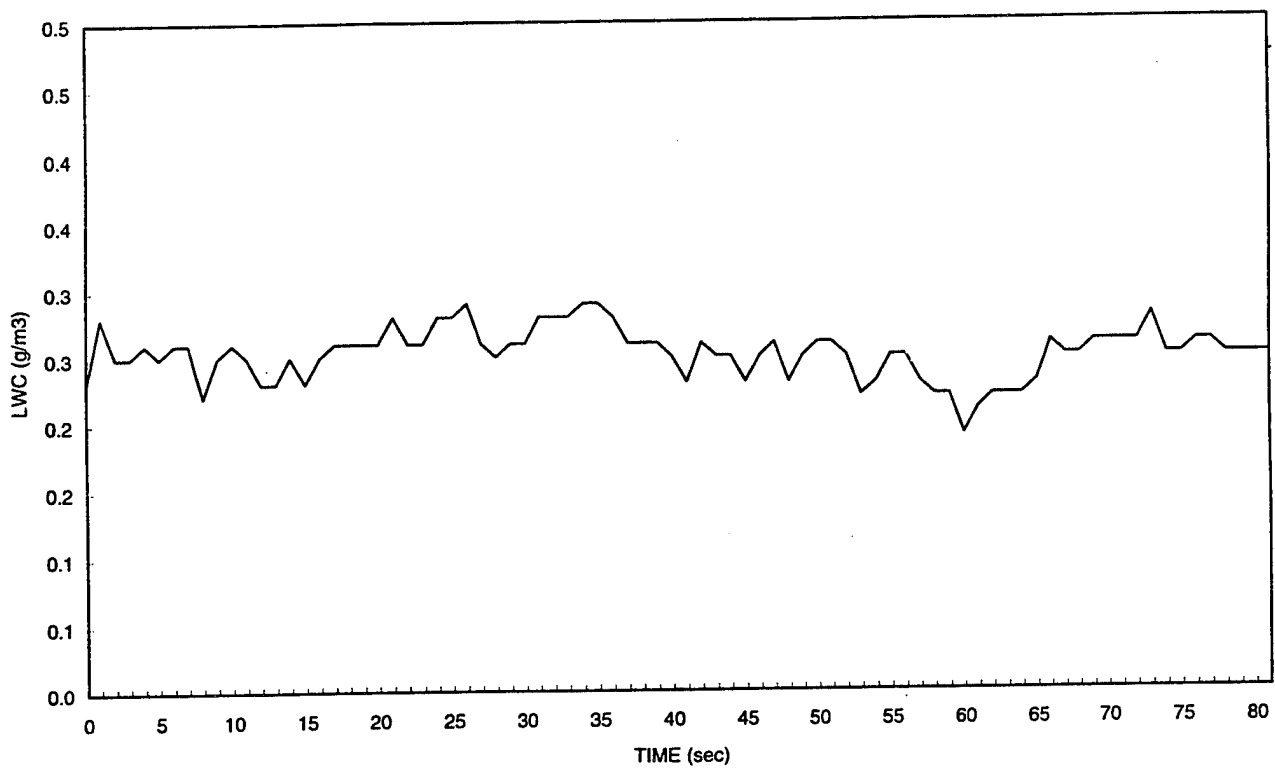


(a)

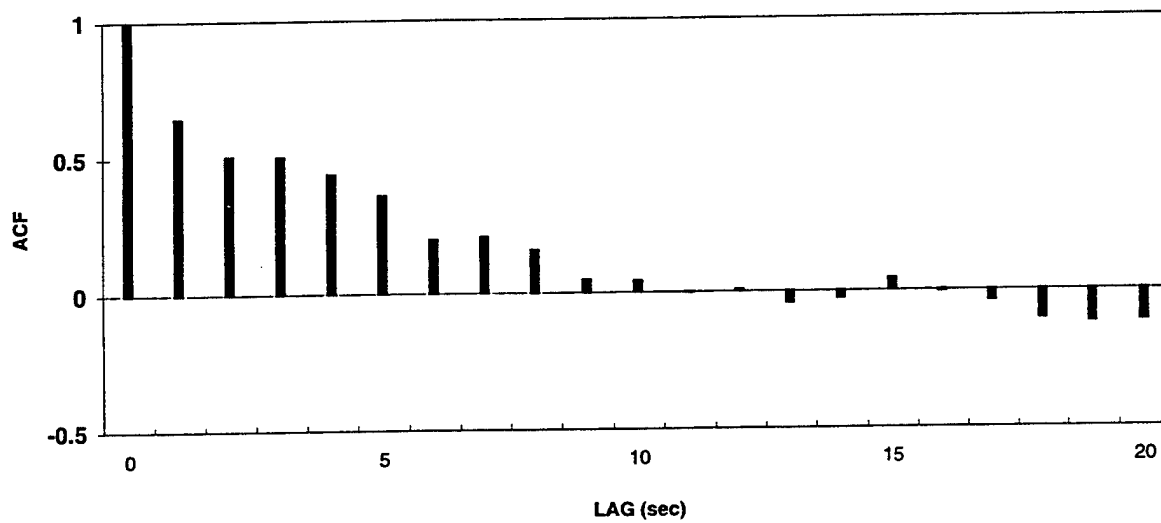


(b)

Figure 23 Time Series of LWC in g/m^3 (Panel A) and Autocorrelation Function (Panel B) for Observed Path I9 through South Africa Cumulus Cloud

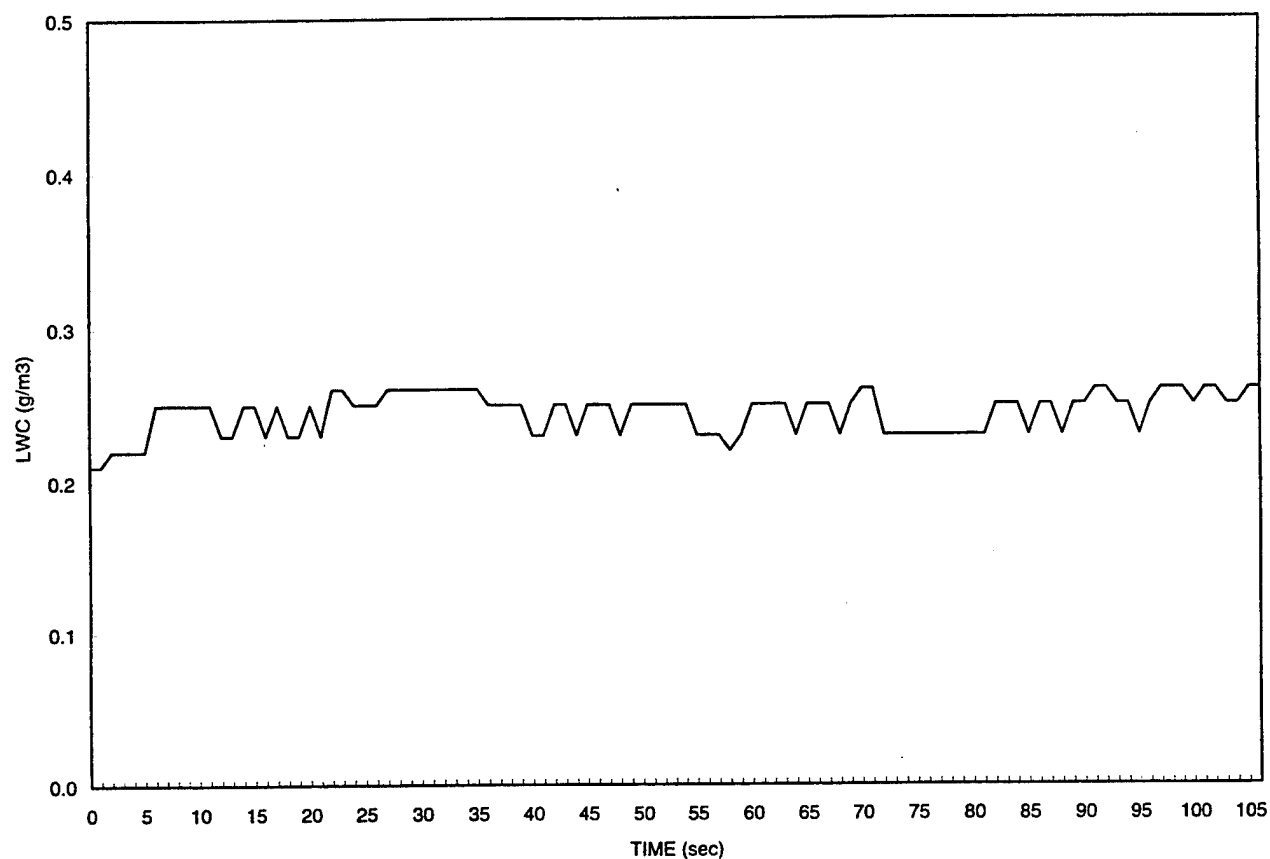


(a)

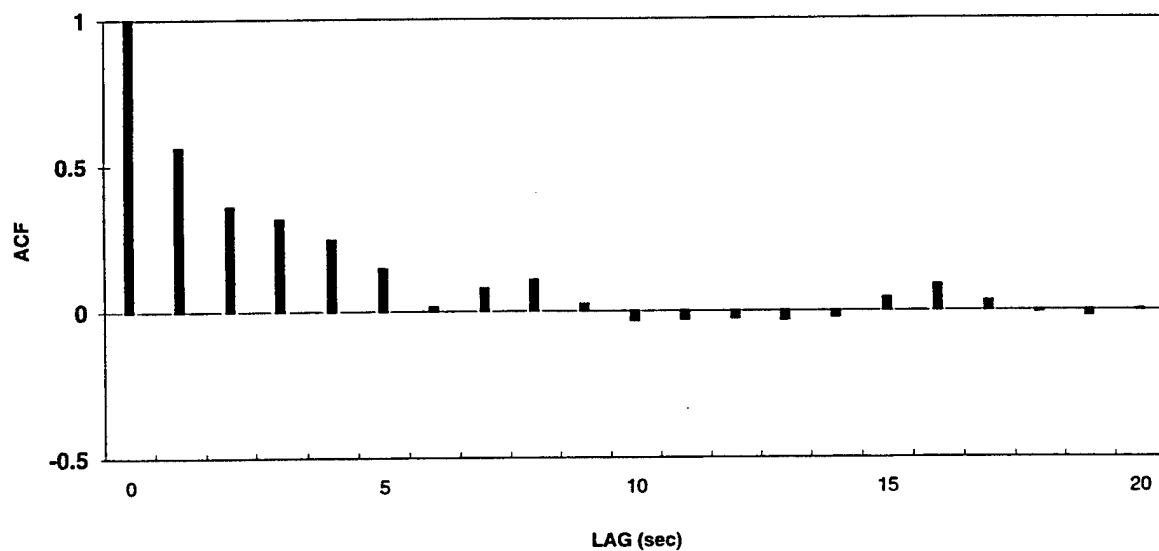


(b)

Figure 24 Time Series of LWC in g/m^3 (Panel A) and Autocorrelation Function (Panel B) for Observed Path W3 through Nova Scotia Stratus Cloud



(a)



(b)

Figure 25 Time Series of LWC in g/m^3 (Panel A) and Autocorrelation Function (Panel B) for Observed Path Y2 through Nova Scotia Stratus Cloud

**Table 13 LWC Statistics for Observed Paths Used in
Parameter Estimation**

DATASET	SERIES	MIN (g/m ³)	MAX (g/m ³)	MEAN (g/m ³)	STDEV (g/m ³)	CORR LENGTH (sec)
A	1	0	0.35	0.064	0.080	5
	2	0	0.35	0.129	0.077	15
	3	NOT USED				
	4	0	0.44	0.228	0.094	11
	5	NOT USED				
	6	0	0.28	0.124	0.065	7
	7	0	0.42	0.133	0.109	38
C	1	0	0.14	0.059	0.038	9
	2	0	0.79	0.169	0.230	23
	3	0	0.16	0.074	0.036	7
	4	NOT USED				
E	1	NOT USED				
	2	0	0.42	0.116	0.076	7
	3	0	0.4	0.090	0.108	11
	4	0	0.26	0.075	0.067	5
	5	NOT USED				
	6	NOT USED				
	7	0	0.37	0.066	0.095	30
	8	NOT USED				
	9	0.02	0.67	0.298	0.164	8
	10	NOT USED				
	11	0	0.47	0.195	0.118	26
	12	0	0.42	0.192	0.115	6
	13	0	0.77	0.362	0.187	11
	14	0	0.7	0.234	0.137	8
	15	NOT USED				
F	1	NOT USED				
	2	0	0.91	0.331	0.245	13
	3	NOT USED				
	4	0	0.51	0.075	0.098	29
	5	0.05	0.3	0.110	0.039	22
	6	0	0.58	0.052	0.098	19
	7	0	1.37	0.278	0.285	11
	8	NOT USED				
G	9	NOT USED				
	1	0	1.91	0.654	0.456	13

**Table 13 LWC Statistics for Observed Paths Used in
Parameter Estimation (continued)**

DATASET	SERIES	MIN (g/m ³)	MAX (g/m ³)	MEAN (g/m ³)	STDEV (g/m ³)	CORR LENGTH (sec)
	2	0	1	0.388	0.293	18
	3	0	0.93	0.213	0.220	9
	4	0	0.88	0.165	0.159	4
H	1	0	1.5	0.702	0.482	8
	2	0.03	2.12	0.531	0.679	16
I	1	0.02	1.96	0.691	0.523	5
	2	0.06	0.74	0.444	0.262	8
	3	0.09	1.49	0.555	0.542	13
	4	0.11	0.5	0.250	0.128	16
	5	0.12	0.67	0.157	0.094	12
	6	0.13	1.45	0.647	0.613	24
	7	0	0.39	0.136	0.118	19
	8	0.08	0.27	0.145	0.053	12
	9	0.07	1.49	1.128	0.375	5
	10	0.03	1.62	1.189	0.448	18
	11	0.01	1.87	1.257	0.545	13
	12	0.11	1.86	1.169	0.619	13
	13	0.06	1.96	1.018	0.628	20
K	1	0	1.58	0.514	0.472	7
	2	0	1.7	0.611	0.593	37
	3	NOT USED				
	4	NOT USED				
O	1	NOT USED				
	2	0	0.16	0.034	0.035	4
	3	0	0.28	0.095	0.072	16
	4	0	0.12	0.046	0.026	9
W	1	0.05	0.22	0.156	0.053	15
	2	0.16	0.32	0.245	0.037	NA
	3	0.19	0.29	0.252	0.019	11
	4	0.18	0.29	0.239	0.025	17
	5	0.19	0.28	0.233	0.016	9
	6	0.08	0.21	0.172	0.022	8
X	1	0.15	0.28	0.214	0.026	13
	2	0.16	0.3	0.237	0.033	63
Y	1	0.02	0.29	0.186	0.052	21
	2	0.21	0.26	0.244	0.013	10

2.3.2 Parameter Estimation

Numerous CSSM model parameters affect the final distribution of LWC within the simulated clouds. We used an iterative approach to estimate model parameters which produced simulated LWC paths with characteristics similar to those found in the observations described above. First, we initialized the model with single-point input meteorological profiles representative of conditions for the times and locations for which LWC paths were available. Since no supporting meteorological data (such as soundings) were available for the LWC datasets, we estimated the profiles based on climatological data and observed data collected under similar weather conditions. This lack of exact initial conditions made it impossible to “tune” the model to produce LWC paths with characteristics that exactly match those found in the observations. Instead, our goal was to tune the model to produce simulated paths which are generally consistent with those observed.

We chose not to modify the fractal parameters (Hurst and lacunarity parameters, lattice resolution, etc.) that were selected in the previous PL/SWOE effort. Those parameters were chosen based on values reported in the literature, and we saw little reason to change them at this time. To estimate the other model parameters, we started by running the model with the set of model parameters used in the PL/SWOE version of the CSSM. We next modified selected model parameters, one at a time, to determine the effect of each parameter on final LWC distribution and overall cloud structure. While this process was not an exhaustive sensitivity study, it focused our attention on those parameters most responsible for determining the final LWC distribution.

2.3.2.1 Cumulus Model

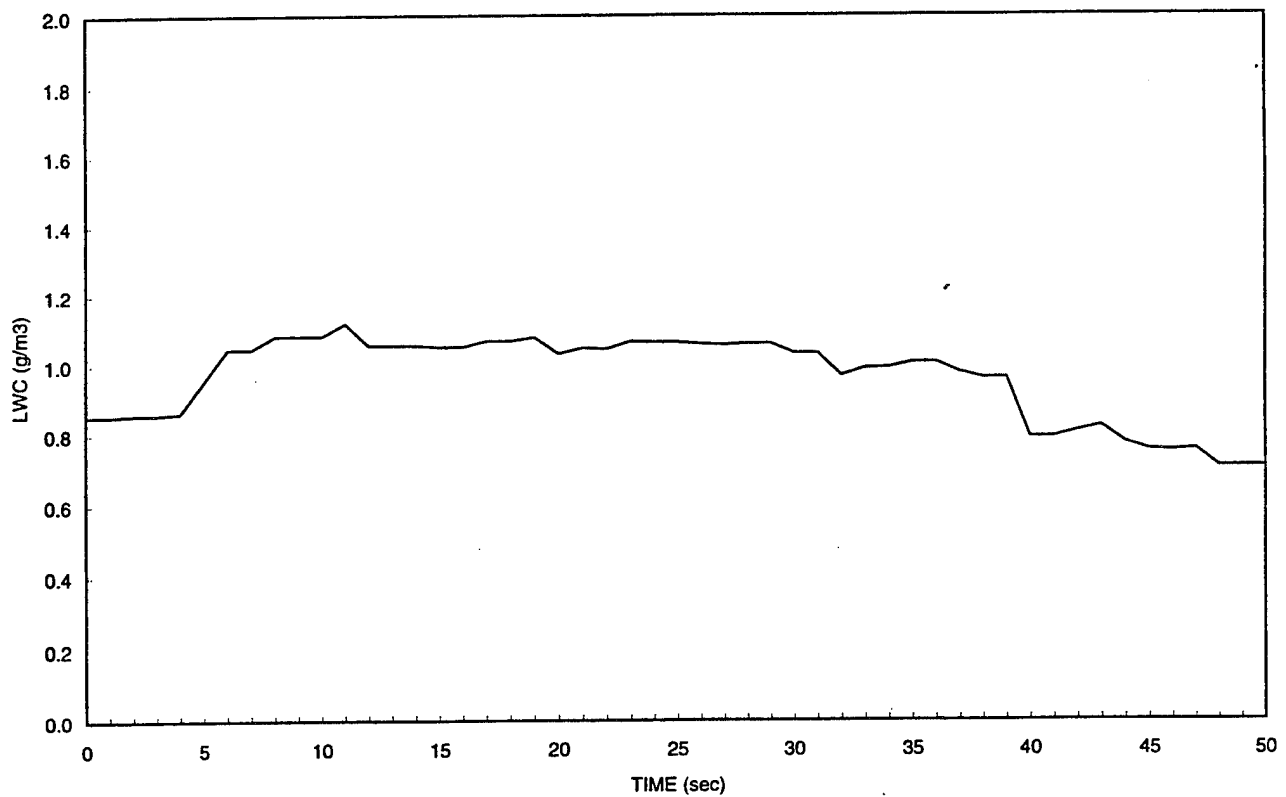
To estimate the cumulus model parameters, we initialized the model with atmospheric profiles representative of conditions for the times and locations of the cumulus paths shown in Table 13. Table 14 shows the profiles used for the three cumulus cases.

The complexity of the CSSM cumulus model and the number of model parameters required that we iterate several times to converge on a suitable set of model parameters. We focused our efforts on the parameters which affect entrainment, parcel size, and parcel buoyancy. The parameter estimation effort focused on tuning the cumulus model parameters to produce realistic LWC magnitudes and variability without producing simulated clouds of unrealistic heights. The final set of tuned parameters is shown in Table 15.

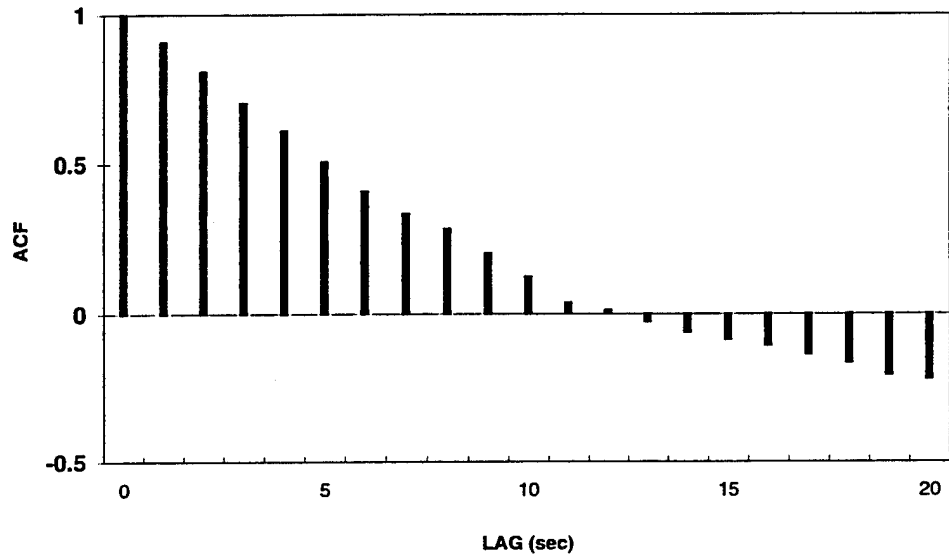
Table 14 Atmospheric Profiles Used to Initialize Cumulus Simulations

PRESSURE (MB)	HEIGHT (M)	TEMP (C)	DEWPOINT (C)	U WIND (M/S)	V WIND (M/S)
MONTANA					
100	16150	-51	-75	52	0
150	12600	-51	-75	52	0
200	11800	-51	-75	52	0
250	10300	-50.5	-75	52	0
300	9150	-45	-70	45	1.8
400	7150	-29.5	-38	30	0.5
500	5600	-16	-24	20	-0.7
600	4200	-7.5	-12	14.5	-2.2
700	3000	1	-3.2	11.5	-1.3
850	1500	14.2	6.2	7	1
930	667	21	10	3.5	1
FRANCE					
100	16465	-56.3	-86.3	5	0
150	13891	-56.6	-86.6	9	-2
200	12077	-56.5	-86.5	12	-2
300	9423	-40.5	-70.5	11	-4
500	5738	-13.7	-27.3	8	-1
700	3104	1.3	-9.8	5	0
850	1519	8	1.8	4	0
SOUTH AFRICA					
100	16560	-70	-100	15	0
200	12340	-55	-73	20	0
250	10890	-44	-64	1	3
300	9650	-34	-57	3	1
400	7570	-18	-42	8	2
500	5870	-7	-33	1	1
600	4230	1	-30	1	1
700	3170	8.5	-1	1	1
800	1950	18	-6	1	1
840	1681	23	15	1	1

After the final parameter estimation was completed, we extracted several LWC paths from the simulated cloud fields for comparison with the observations. The selected paths were extracted at heights above the simulated cloud bases that corresponded to the observed paths' heights above actual cloud bases. Figure 26 and Figure 27 show two representative LWC time series and associated autocorrelation functions from the simulations.

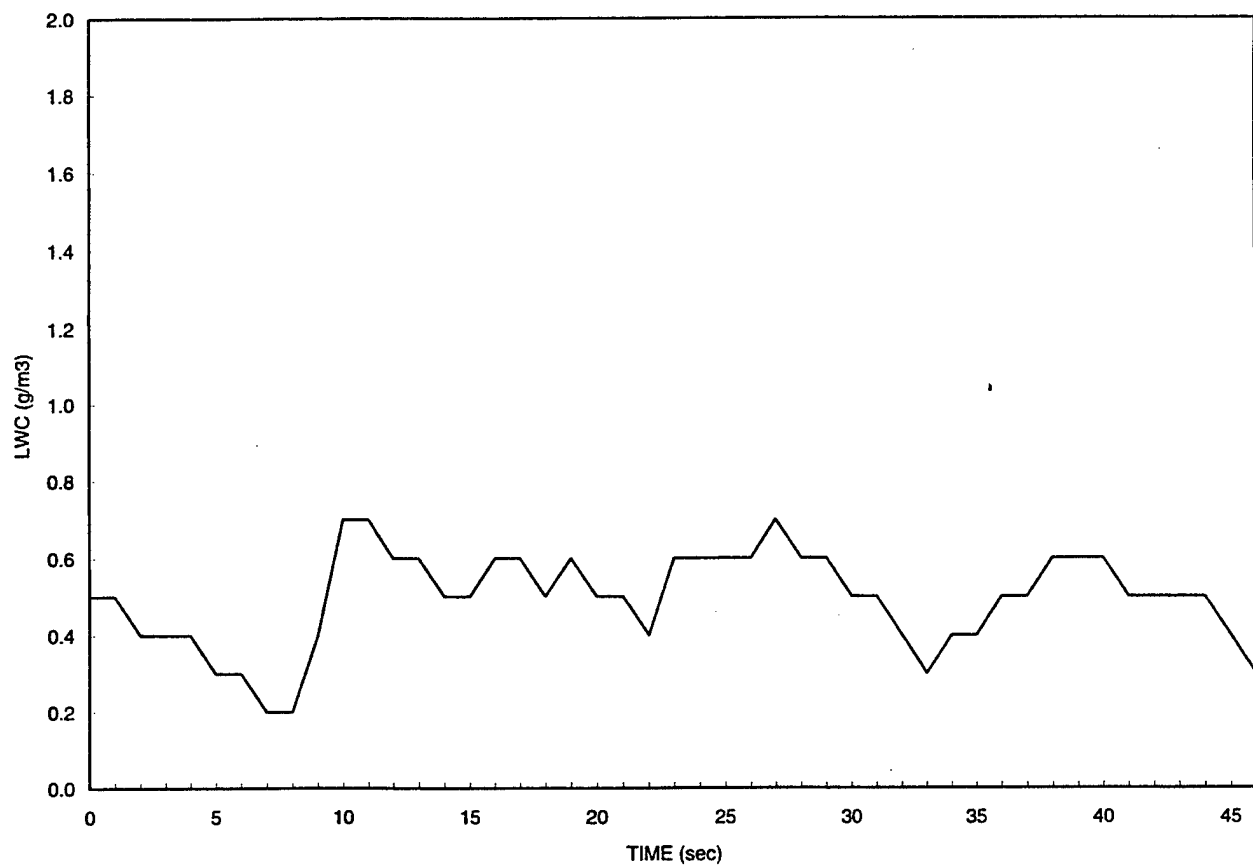


(a)

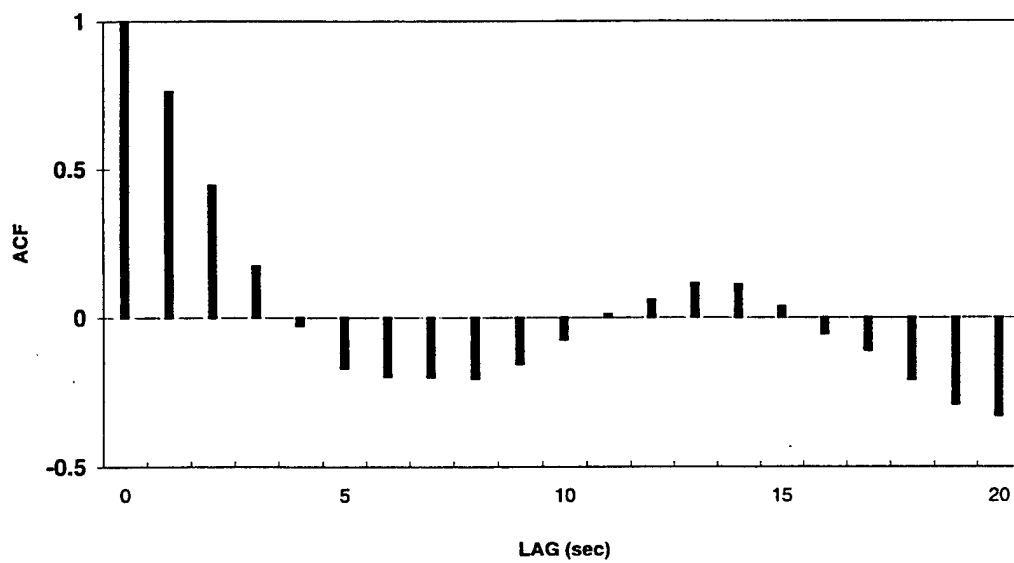


(b)

Figure 26 Time Series of LWC in g/m^3 (Panel A) and Autocorrelation Function (Panel B) for Simulated Path MON8 through Montana Cumulus Cloud



(a)



(b)

Figure 27 Time Series of LWC in g/m^3 (Panel A) and Autocorrelation Function (Panel B) for Simulated Path BET3 through South Africa Cumulus Cloud

Table 15 Final Cumulus Model Parameters

CUMULUS MODEL PARAMETER	VALUE
Hurst parameter	NA
Lattice resolution	NA
Maximum entrainment rate	250%/100 mb
Minimum entrainment rate	50%/100 mb
Entrainment radius	1000 m
Maximum parcel size	400 m
Minimum parcel size	100 m
Parcel lifetime	2000 sec
Maximum temperature perturbation	0.5 K
Minimum temperature perturbation	0.1 K

Table 16 shows the LWC statistics calculated for each of the simulation paths used in the parameter estimation effort (statistics for the “validation” paths are presented later). Figure 28, Figure 29, and Figure 30 graphically compare the statistics for all the simulated cumulus paths with those for the observed paths. These comparisons are categorized by location and height above cloud base.

Table 16 LWC Statistics for Simulated Paths Used in Cumulus Model Parameter Estimation

PATH	MIN (g/m ³)	MAX (g/m ³)	MEAN (g/m ³)	STDEV (g/m ³)	CORR LENGTH (sec)
MONTANA					
MON1	0.016	0.284	0.10	0.048	7
MON2	0.014	0.205	0.10	0.041	7
MON3	0.311	0.766	0.52	0.124	13
MON4	0.266	0.837	0.54	0.142	12
MON5	0.585	0.984	0.80	0.096	16
MON6	0	1.096	0.80	0.207	18
MON8	0.704	1.118	0.96	0.124	13
MON9	0.565	1.165	0.82	0.182	11
MON7	0.984	1.52	1.34	0.133	18
FRANCE					
BOR1	0.113	0.975	0.78	0.149	6
BOR2	0.335	0.737	0.52	0.092	8
BOR3	0.768	1.229	1.01	0.108	20
BOR4	0.412	1.187	0.90	0.136	10
BOR6	1.183	1.252	1.23	0.017	8
BOR5	1.18	1.271	1.23	0.021	4
SOUTH AFRICA					
BET1	0.38	0.997	0.74	0.151	10
BET2	0.526	1.017	0.84	0.096	7
BET3	0.172	0.671	0.49	0.114	4
BET4	0.357	0.7	0.59	0.089	7

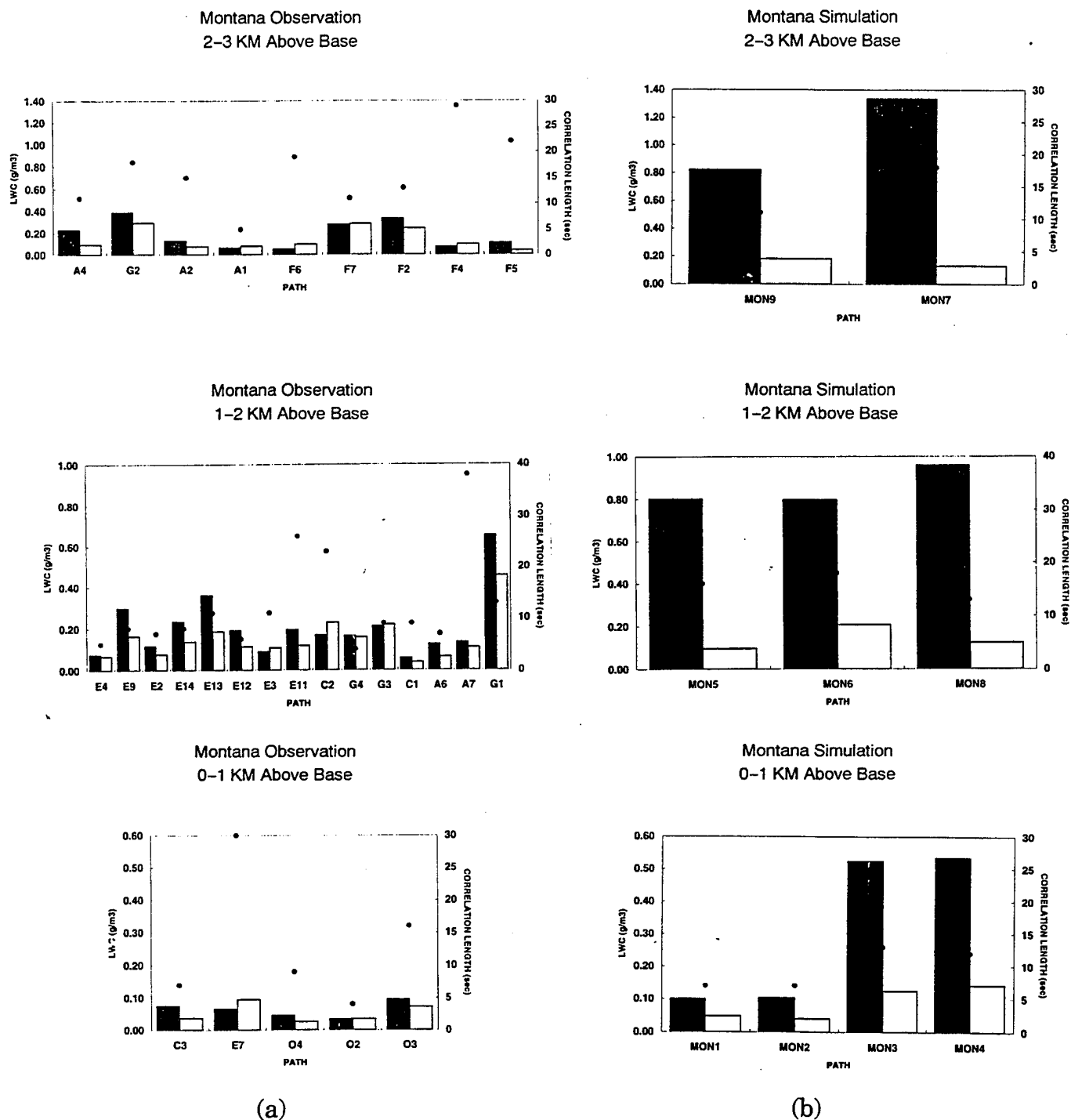


Figure 28 Path Water Content Statistics for Montana Cumulus Clouds. Dark/Light Columns Depict Water Content Mean/Standard Deviation (Expressed in g/m^3). Black dots Represent Correlation Length in Seconds. Panels A Are Statistics for Observed Paths at Indicated Heights Above Cloud Base. Panels B are Statistics for Simulated Paths.

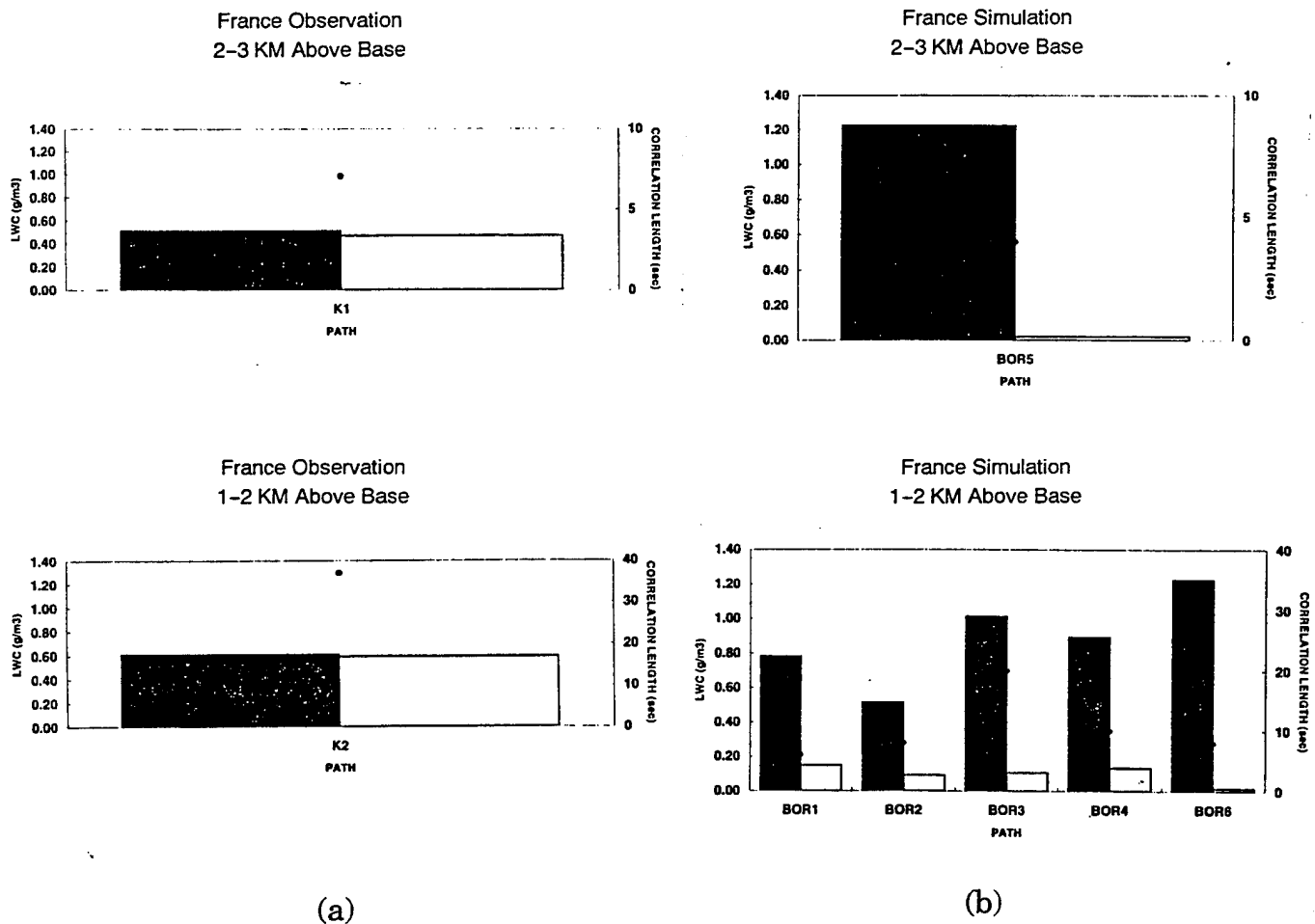


Figure 29 Path Water Content Statistics for France Cumulus Clouds. Dark/Light Columns Depict Water Content Mean/Standard Deviation (Expressed in g/m^3). Black dots Represent Correlation Length in Seconds. Panels A Are Statistics for Observed Paths at Indicated Heights Above Cloud Base. Panels B are Statistics for Simulated Paths.

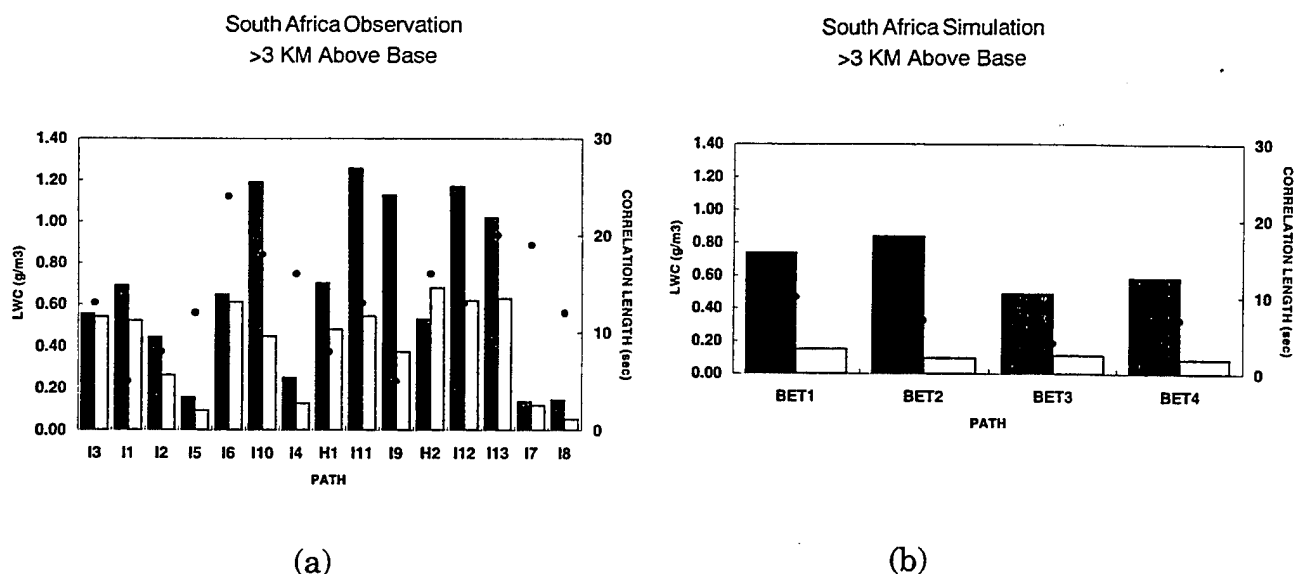


Figure 30 Path Water Content Statistics for South Africa Cumulus Clouds. Dark/Light Columns Depict Water Content Mean/Standard Deviation (Expressed in g/m^3). Black dots Represent Correlation Length in Seconds. Panels A Are Statistics for Observed Paths at Indicated Heights Above Cloud Base. Panels B are Statistics for Simulated Paths.

A comparison of the simulated path results with observed paths shows generally good agreement. The variability of the simulated LWC fields for all simulations (as expressed in the path LWC standard deviation and correlation lengths) agrees quite well with that seen in the corresponding observations. A comparison of the observed time series and corresponding autocorrelation functions (see Figure 22 and Figure 23) with the simulated time series and autocorrelation functions for similar heights above cloud base also shows good agreement in the LWC variability.

The mean LWC values from the Montana simulation generally exceeded those found in the Montana observations, while the mean LWC values for the South Africa simulation are generally lower than the corresponding observations. There were too few French observations to allow for a significant comparison.

These results demonstrated the model's ability to achieve reasonable LWC magnitudes and variability with the chosen model parameters. Since our tuning simulations used estimated soundings and the results were compared with observations from several days, some disparity between the simulations and the observations was expected. The variation in simulated LWC above and below the observed values (for the Montana and South Africa cases, respectively) show that on average our tuned parameters provide reasonable simulated LWC magnitudes.

2.3.2.2 Stratus Model

The methodology for parameter estimation for the stratus model was analogous to that used for the cumulus model. The process was simplified considerably, however, since fewer parameters control the stratus cloud development. For the stratus parameter estimation, we initialized the CSSM with atmospheric profiles representative of conditions for the time and location of the stratus paths shown in Table 13. Table 17 shows the profile used for the stratus simulations.

Table 17 Atmospheric Profile Used to Initialize Stratus Simulations

PRESSURE (MB)	HEIGHT (M)	TEMP (C)	DEW POINT (C)	U WIND (M/S)	V WIND (M/S)
NOVA SCOTIA					
100	16150	-58.1	-77.1	-1	4
150	13520	-53.5	-70.5	1	7
200	11620	-50.7	-64.7	-17	0
250	10130	-51.5	-63.5	-14	5
300	8930	-55.7	-66.7	-33	-19
400	6990	-39.7	-49.2	-18	-21
500	5390	-28	-35.2	-13	-7
700	2836	-10.5	-15	-15	-15
850	1299	-4.5	-5.5	-2	-14
925	618	-1.5	-4	2	-14
994	0	1	-4	2	-9

Our initial tests with the PL/SWOE model parameters produced satisfactory LWC magnitudes and variability. Based on these results and the uncertainty introduced by the lack of concurrent soundings and other meteorological data, we found no compelling reason to modify the original parameters. The final set of stratus parameters is shown in Table 18.

Table 18 Final Stratus Model Parameters

STRATUS MODEL PARAMETER	VALUE
Hurst parameter	0.5
Lattice resolution (x)	1.0 km
Lattice resolution (y)	1.0 km
Lattice resolution (z)	0.5 km
Lattice resolution (t)	300 sec
Water content standard deviation (sdevwc)	0.30
Stratiform cloud top generation power	1.5

We extracted several LWC paths from the simulated cloud fields using the same method as described above for the cumulus model. Figure 31 and Figure 32 show two representative LWC time series and associated autocorrelation functions from the simulation.

Table 19 shows the LWC statistics calculated for each of the simulated paths used in the parameter estimation effort. Figure 33 graphically compares the statistics for all the simulated stratus paths with those for the observed paths.

Table 19 LWC Statistics for Simulated Paths Used in Stratus Model Parameter Estimation

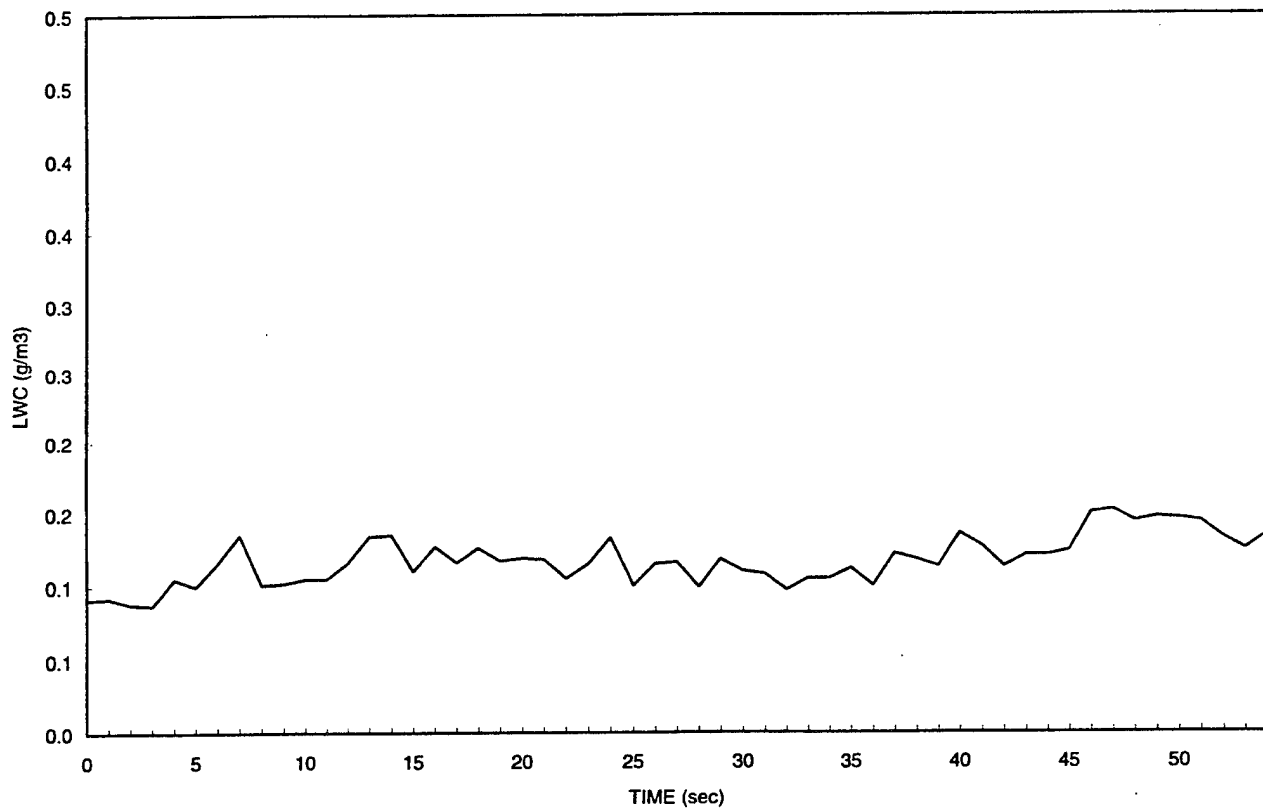
PATH	MIN (g/m ³)	MAX (g/m ³)	MEAN (g/m ³)	STDEV (g/m ³)	CORR LENGTH (sec)
HFX01	0.076	0.145	0.11	0.016	7
HFX02	0.07	0.158	0.12	0.022	15
HFX03	0.059	0.208	0.12	0.034	11
HFX04	0.056	0.174	0.10	0.028	10
HFX11	0.087	0.152	0.12	0.016	11
HFX12	0.073	0.147	0.11	0.016	10
HFX13	0.054	0.16	0.11	0.023	11

Comparison of the simulated path results with observed paths again shows generally good agreement. The simulated path LWC standard deviations and correlation lengths show that the variability of the simulated LWC fields agreed quite well with that seen in the observations. A comparison of the observed time series and corresponding autocorrelation functions (see Figure 24 and Figure 25) with the simulated time series and autocorrelation functions for similar heights above cloud base also shows good agreement in the LWC variability.

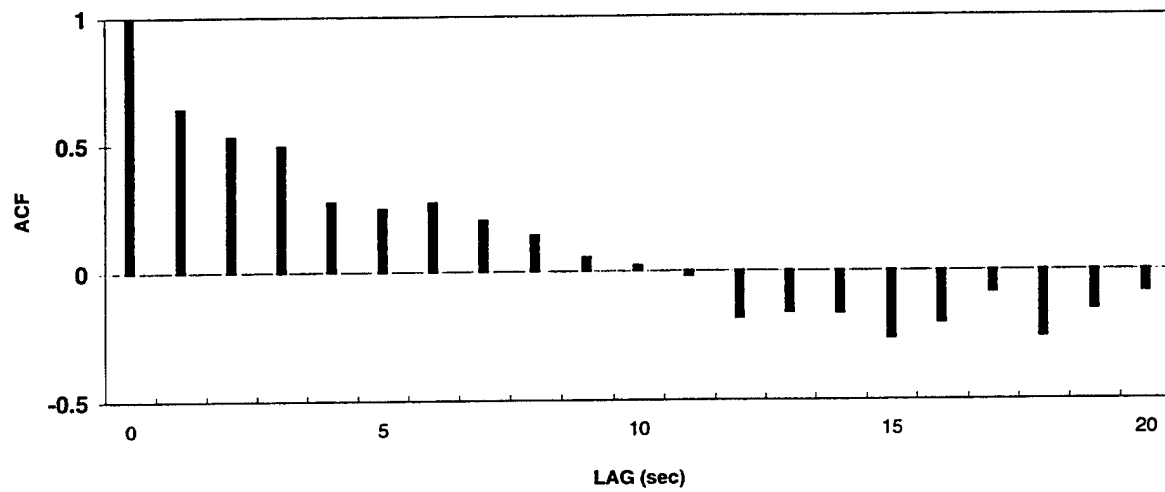
The simulated stratus mean path LWC magnitudes were approximately 25–50% lower than those found in the observations. We chose not to modify the stratus model parameters based on this comparison since our observations were limited to data collected on just one day.

2.3.3 Cumulus Model Validation

The cumulus model was validated using a technique similar to that described above. As mentioned previously, we chose the 20 June 1981 CCOPE dataset for our validation dataset. We chose this dataset not so much for the LWC observations available from that day, but for the supplementary documentation available from other sources. In their discussion of their 3-D numerical simulation of the clouds observed on 20 June, Smolar-kiewicz and Clark (Ref. 24) (S&C), provide excellent documentation of the meteorological

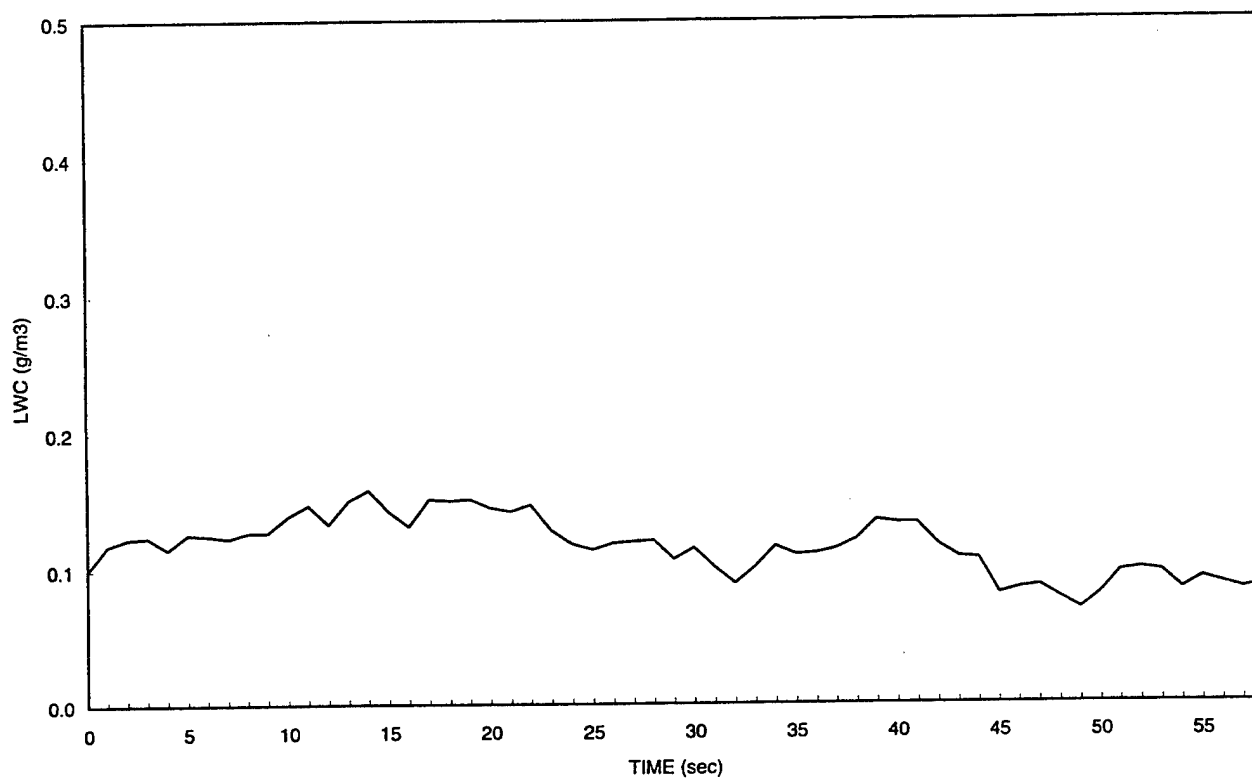


(a)

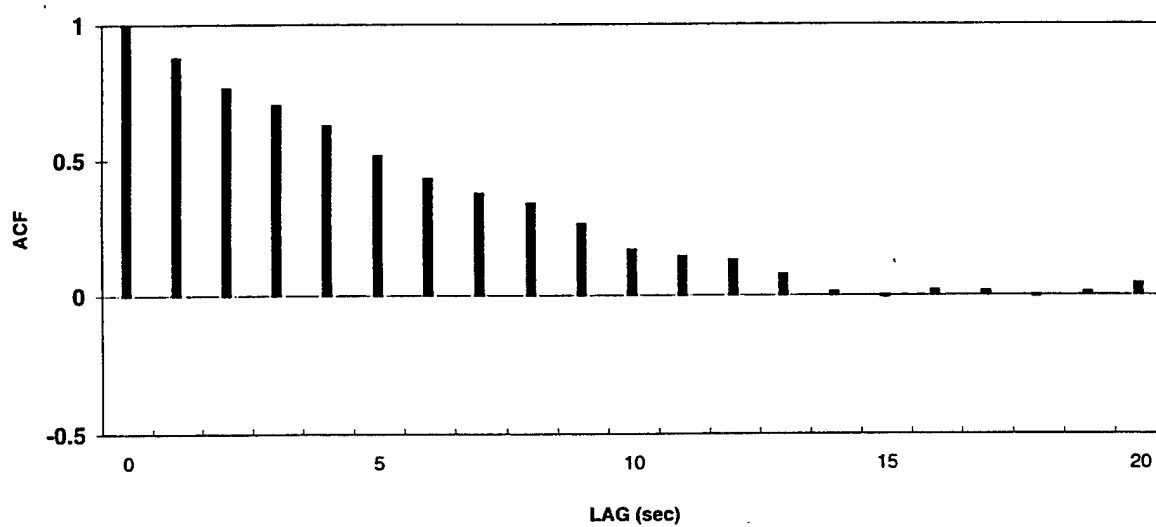


(b)

Figure 31 Time Series of LWC in g/m^3 (Panel A) and Autocorrelation Function (Panel B) for Simulated Path HAL5 through Nova Scotia Stratus Cloud



(a)



(b)

Figure 32 Time Series of LWC in g/m^3 (Panel A) and Autocorrelation Function (Panel B) for Simulated Path HAL2 through Nova Scotia Stratus Cloud

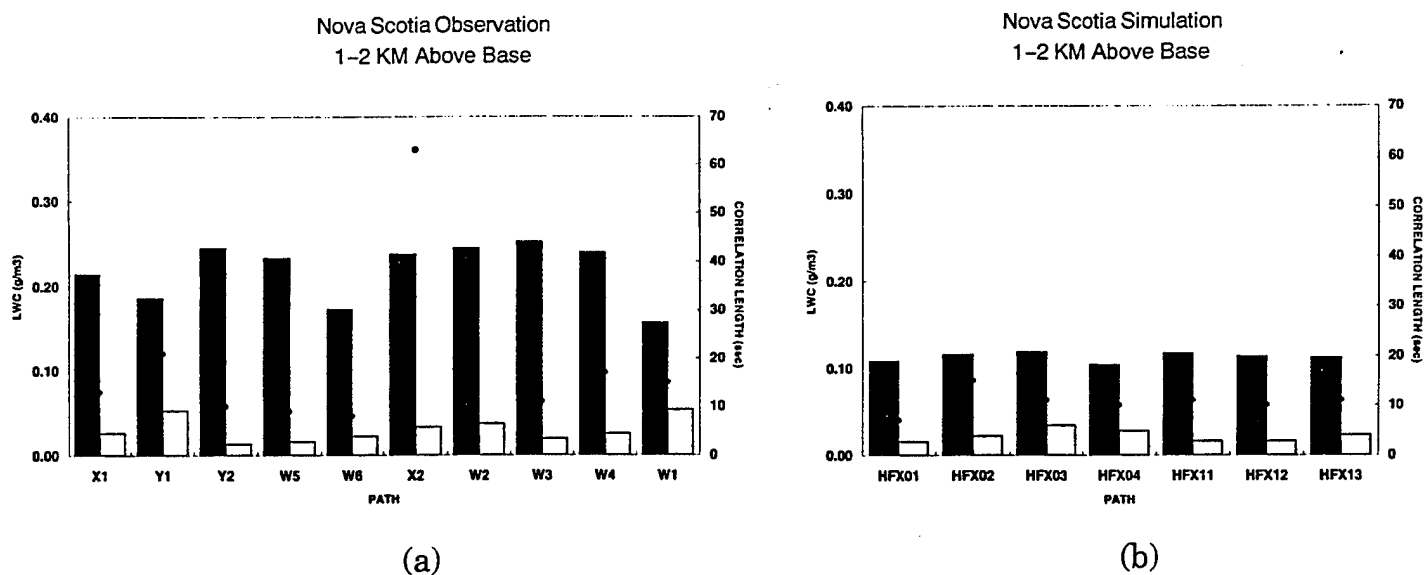
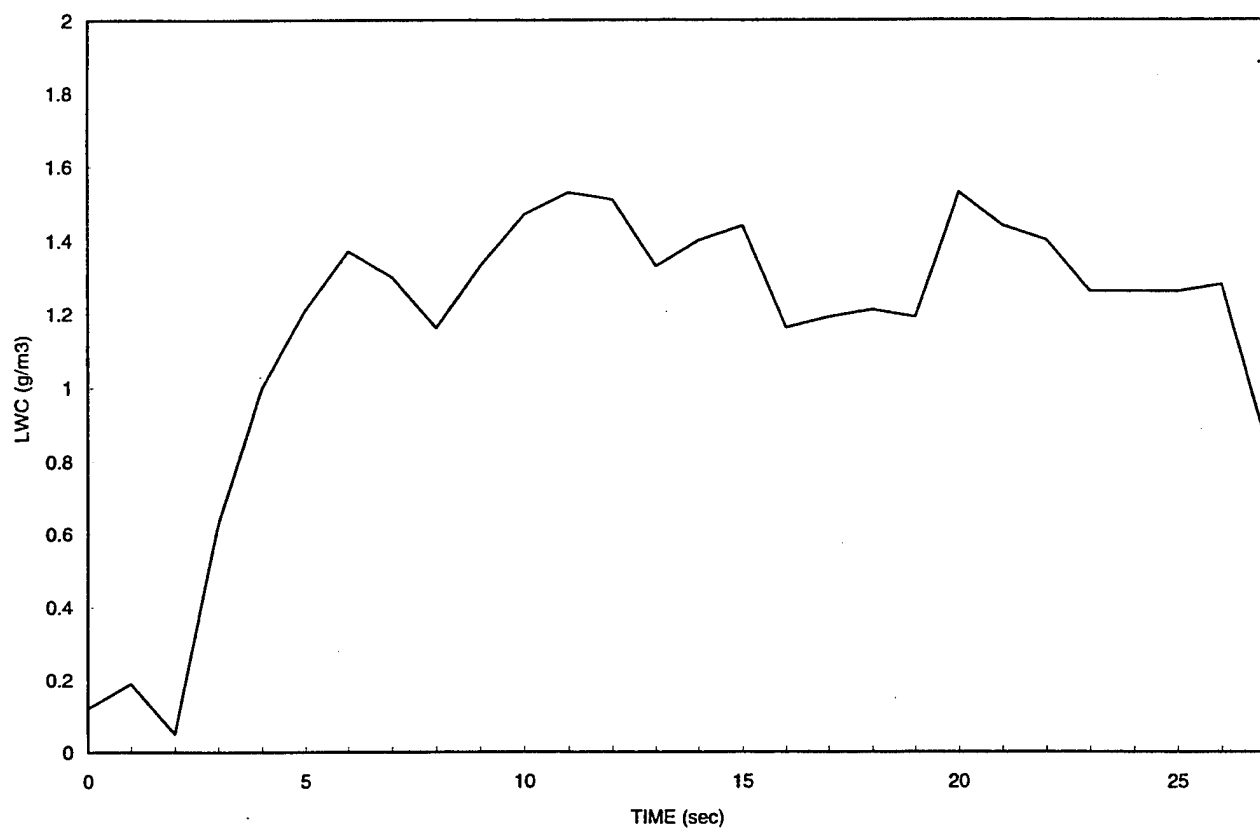


Figure 33 Path Water Content Statistics for Nova Scotia Stratus Cloud. Dark/Light Columns Depict Water Content Mean/Standard Deviation (Expressed in g/m^3). Black dots Represent Correlation Length in Seconds. Panels A Are Statistics for Observed Paths at Indicated Heights Above Cloud Base. Panels B are Statistics for Simulated Paths.

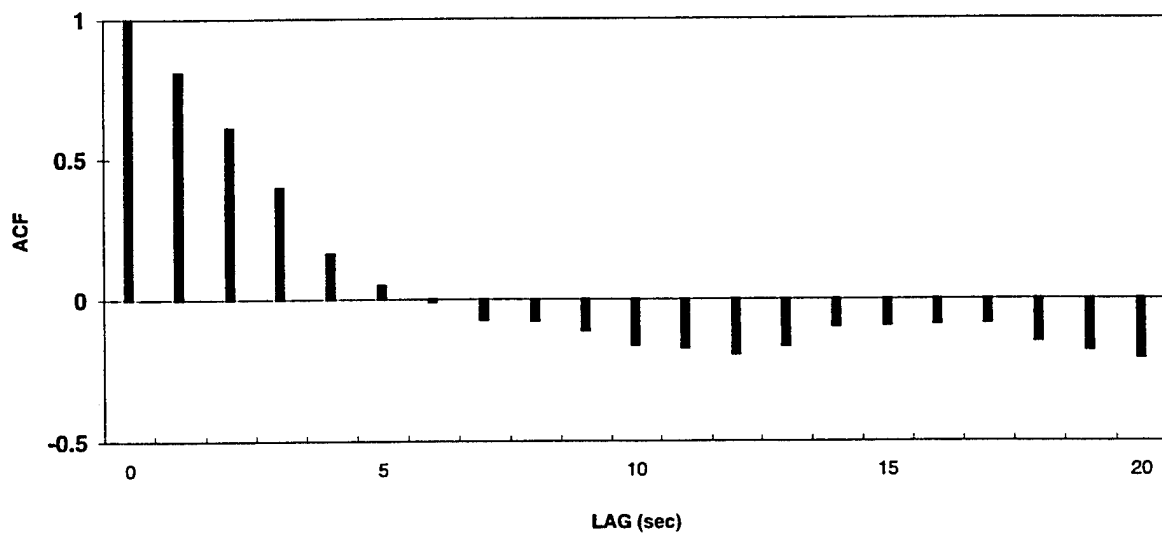
conditions that day. In particular, they provide vertical profiles of temperature, moisture, and winds; information on cloud base and top heights; and several photographs of the observed clouds.

This supplementary information allowed the accurate initialization of the CSSM necessary to remove the uncertainty introduced by estimated soundings. The photographic evidence provides a valuable validation tool for use with the LWC observations.

Figure 34 and Figure 35 show LWC time series and corresponding autocorrelation functions for two of the observed paths used in the validation study. Table 20 shows the LWC statistics calculated for each of the paths used in the validation.

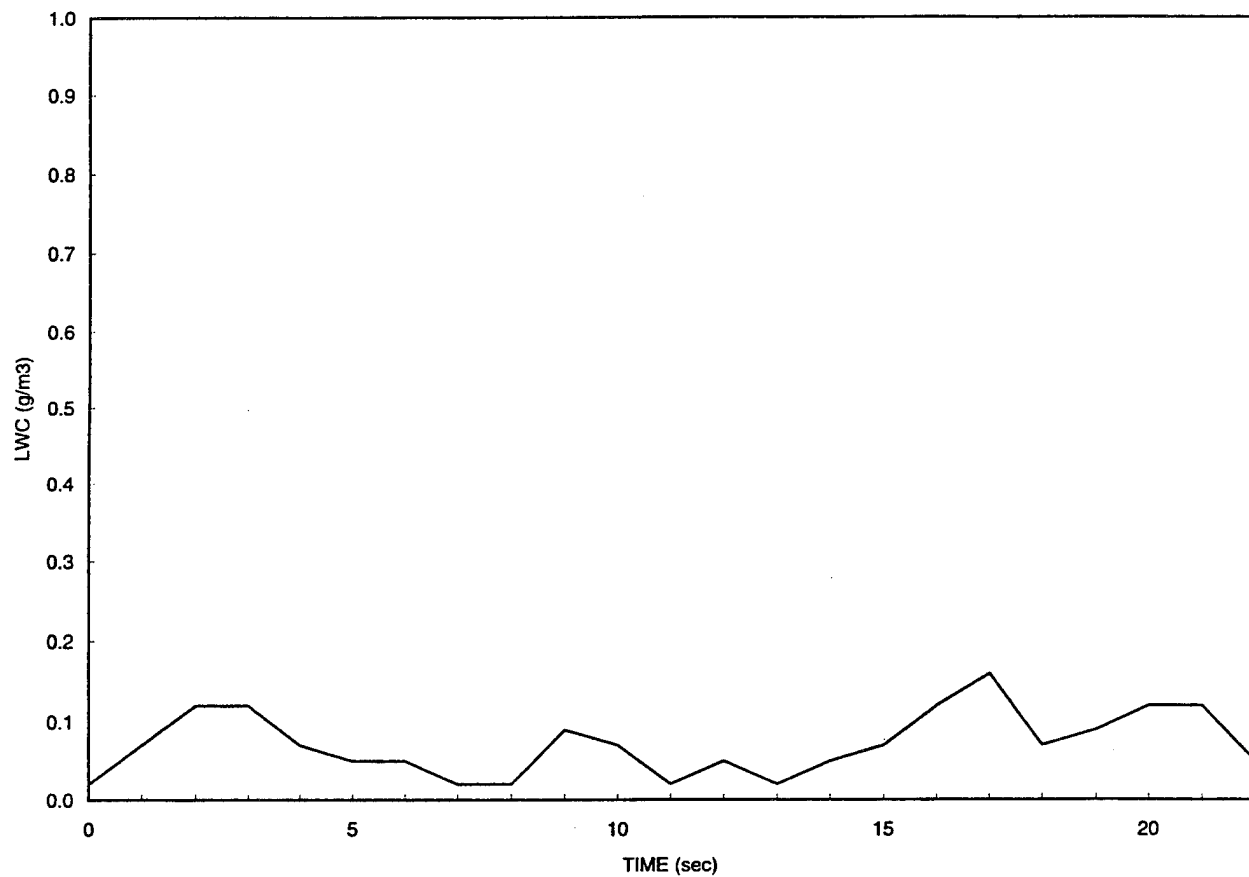


(a)

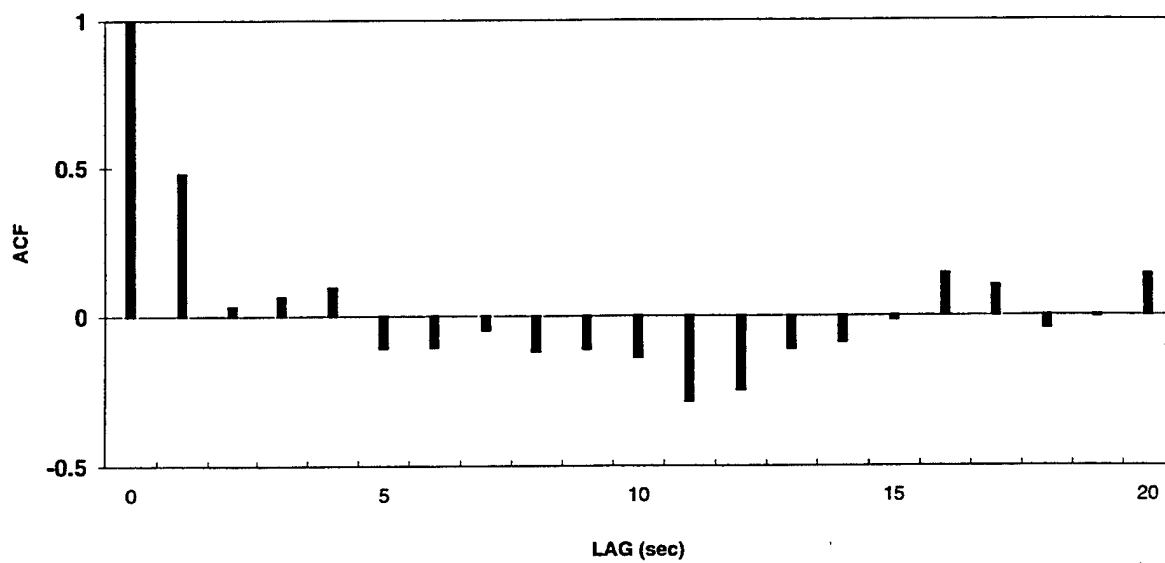


(b)

Figure 34 Time Series of LWC in g/m^3 (Panel A) and Autocorrelation Function (Panel B) for Observed Path P4 through Montana Cumulus Cloud



(a)



(b)

Figure 35 Time Series of LWC in g/m^3 (Panel A) and Autocorrelation Function (Panel B) for Observed Path P1 through Montana Cumulus Cloud

Table 20 LWC Statistics for Observed Paths Used in Cumulus Validation

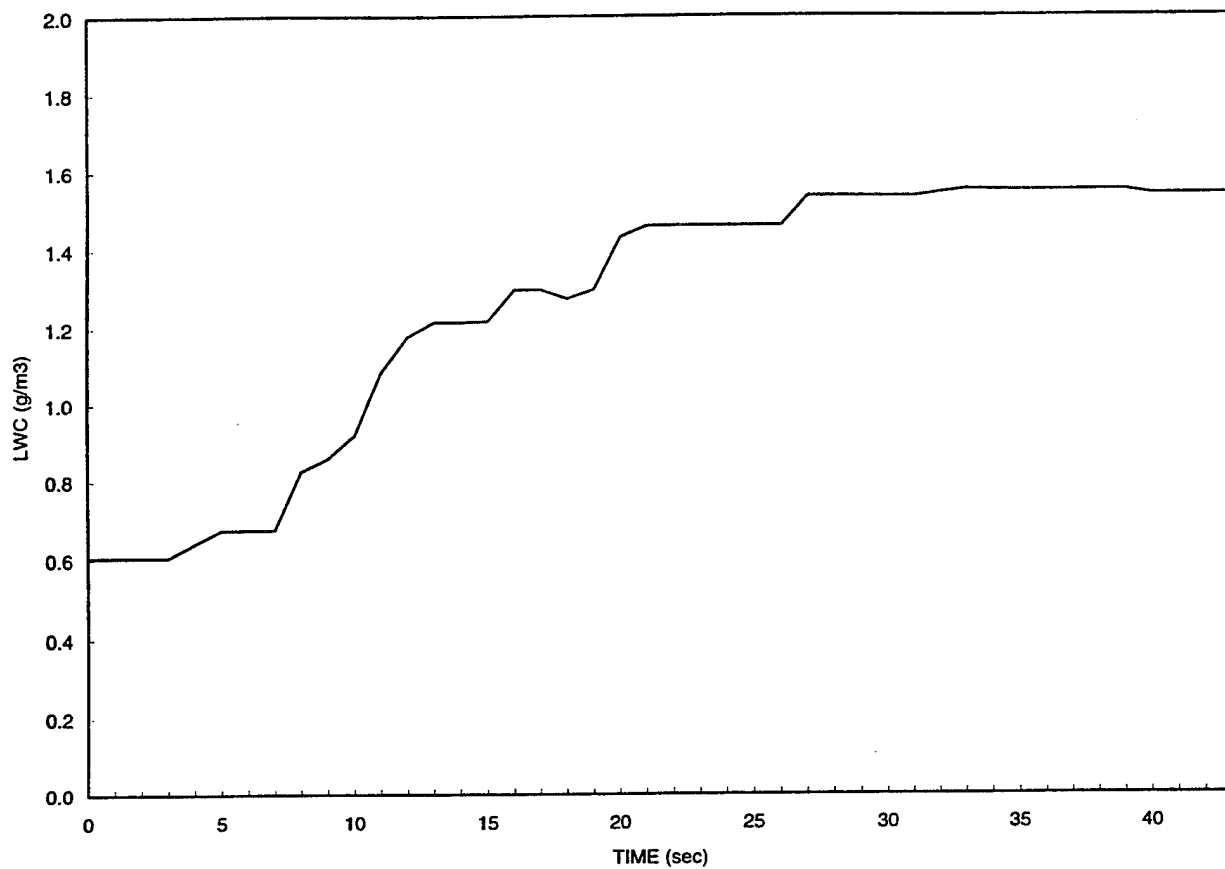
DATASET	SERIES	MIN (g/m ³)	MAX (g/m ³)	MEAN (g/m ³)	STDEV (g/m ³)	CORR LENGTH (sec)
P	1	0.02	0.16	0.068	0.040	5
	2	0.02	0.63	0.284	0.169	10
	3	0.05	1.12	0.546	0.256	3
	4	0.05	1.53	1.110	0.447	6
	5	0.05	2.44	1.264	0.862	6
	6	0.02	2.56	1.478	0.768	5
	7	0.12	1.81	0.800	0.469	10
	8	0.02	1.16	0.455	0.314	5
	9	0.05	1.84	0.560	0.506	4
	10	0.02	0.81	0.261	0.238	4

For the validation effort we initialized the CSSM with the sounding taken from S&C (See Montana profile in Table 14). Several LWC paths were extracted from the simulated cloud field at heights above simulated cloud base corresponding to the observed paths' heights above cloud base. Figure 36 and Figure 37 show two representative LWC time series and associated autocorrelation functions from the simulation.

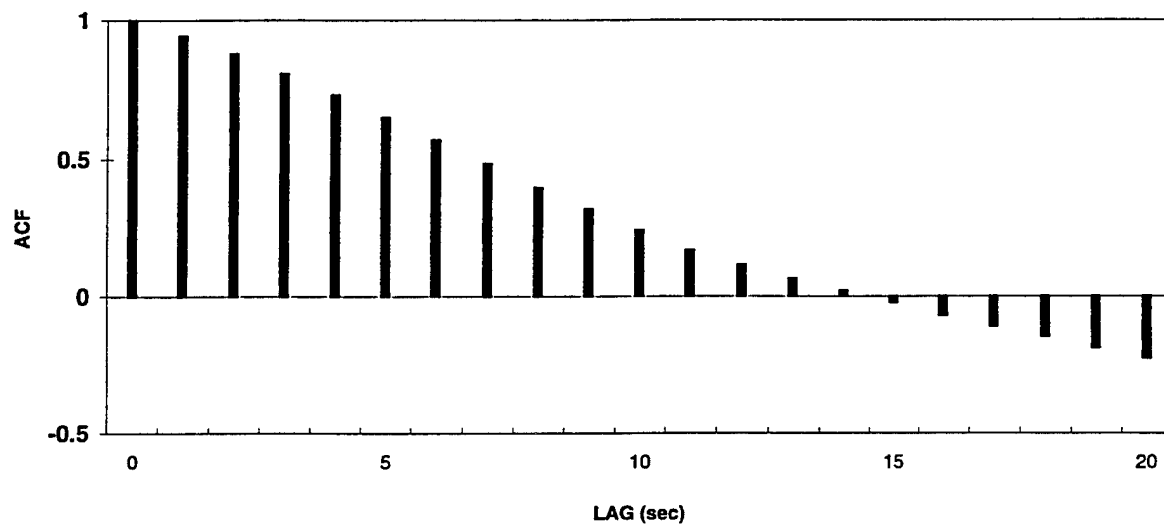
Table 21 shows the LWC statistics calculated for each of the simulated paths used in the validation. Figure 38 graphically compares the statistics for the simulated cumulus paths with those for the observed paths.

Table 21 LWC Statistics for Simulated Paths Used in Cumulus Validation

PATH	MIN (g/m ³)	MAX (g/m ³)	MEAN (g/m ³)	STDEV (g/m ³)	CORR LENGTH (sec)
MONV01	0.008	0.418	0.21	0.093	32
MONV02	0.028	0.56	0.32	0.106	7
MONV11	0.046	0.504	0.274	0.107	31
MONV03	0.236	0.683	0.478	0.088	12
MONV04	0.313	0.661	0.476	0.081	4
MONV05	0.248	0.627	0.441	0.082	18
MONV12	0.206	0.728	0.424	0.145	27
MONV13	0	1.282	0.885	0.318	19
MONV14	0.542	1.334	0.885	0.313	17
MONV06	0.605	1.554	1.254	0.346	15
MONV07	0.551	1.559	1.21	0.372	14
MONV08	0.551	1.559	1.222	0.384	15
MONV15	0.358	1.266	0.635	0.274	14
MONV16	0.353	1.15	0.733	0.279	16
MONV09	0.64	1.518	1.128	0.326	17
MONV17	0.658	1.268	1.089	0.179	13

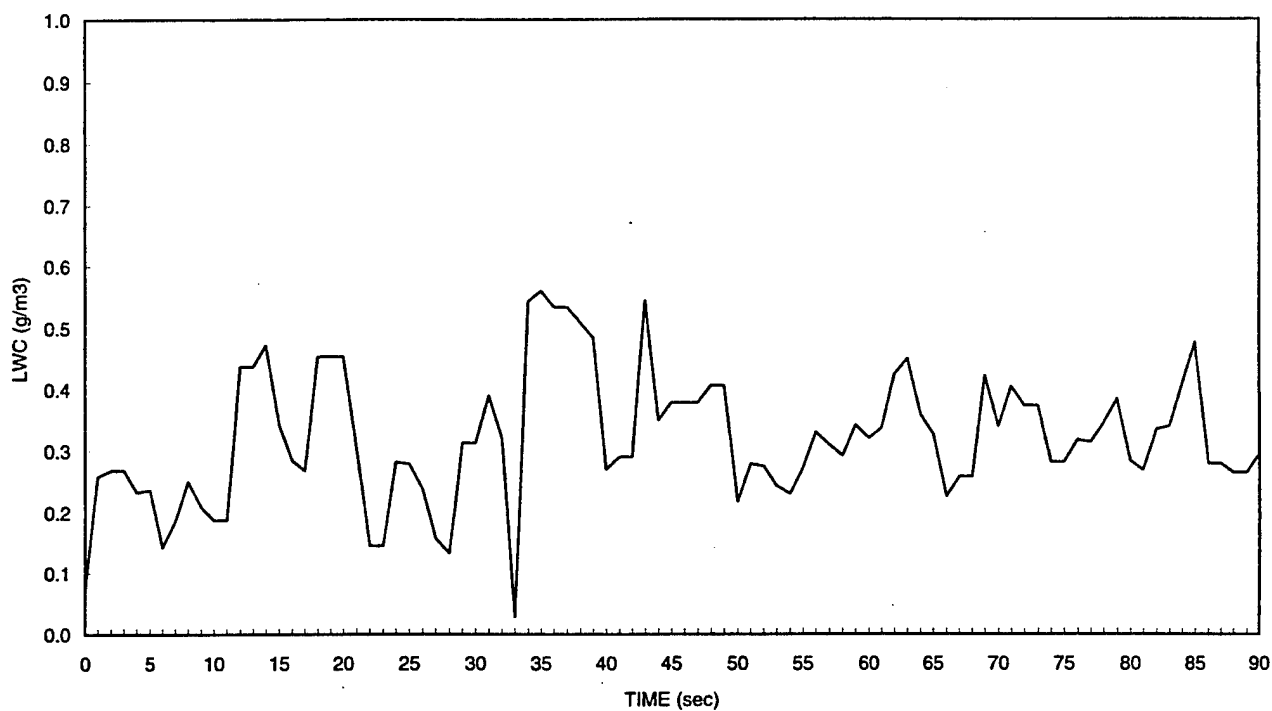


(a)

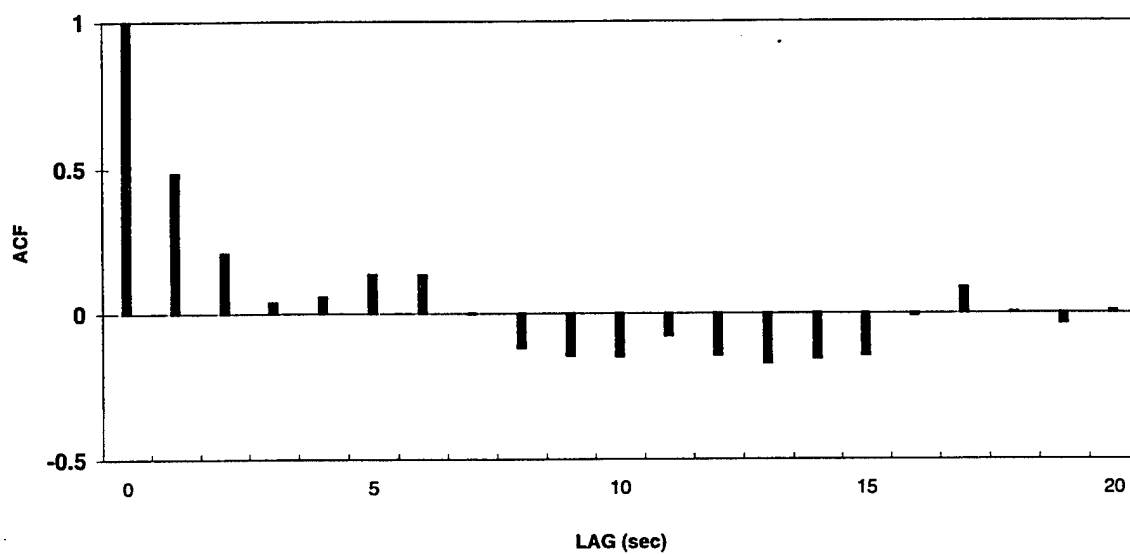


(b)

Figure 36 Time Series of LWC in g/m^3 (Panel A) and Autocorrelation Function (Panel B) for Simulated Path MONV06 through Simulated Montana Cumulus Cloud



(a)



(b)

Figure 37 Time Series of LWC in g/m^3 (Panel A) and Autocorrelation Function (Panel B) for Simulated Path MONV02 through Simulated Montana Cumulus Cloud

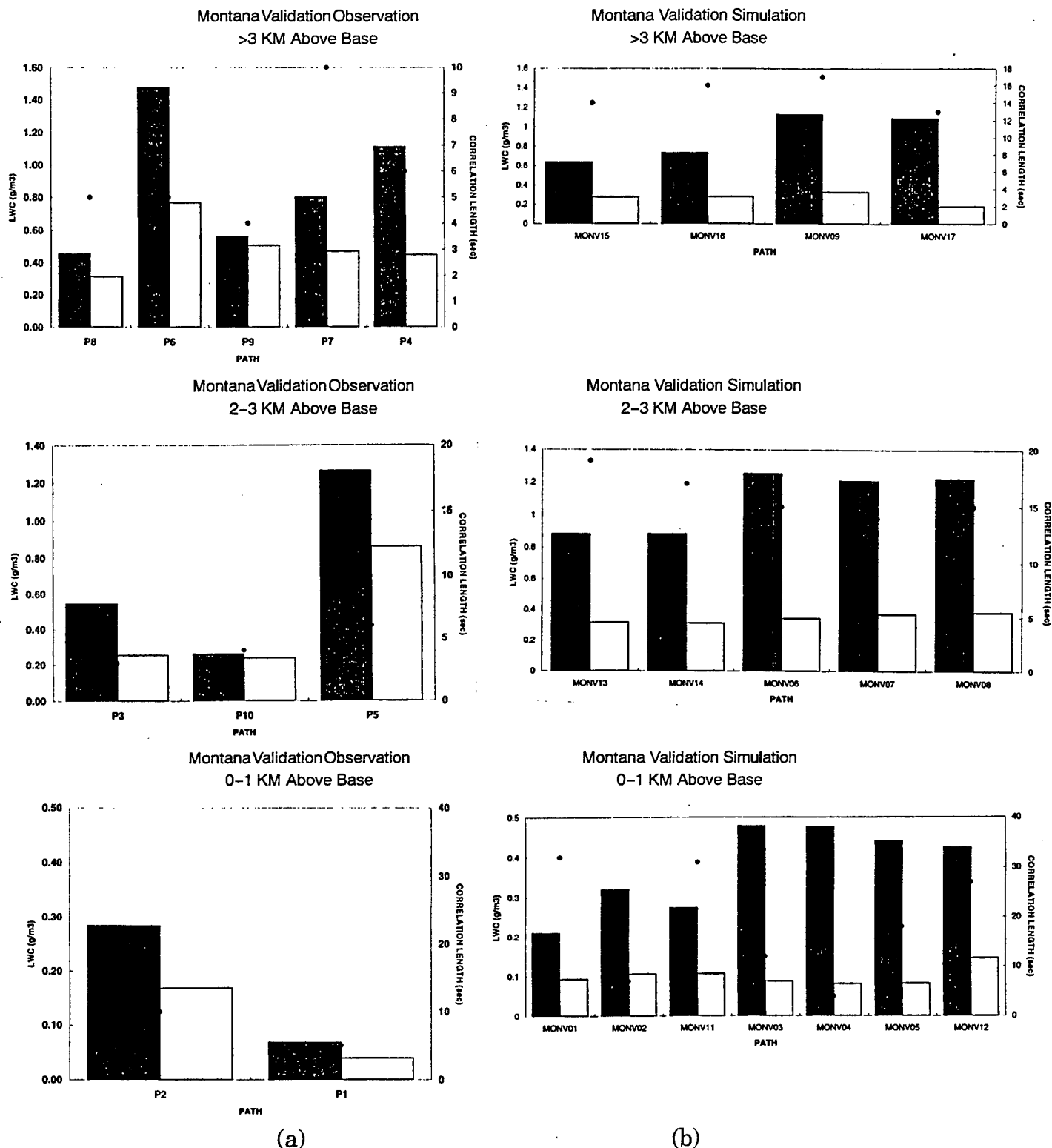


Figure 38 Path Water Content Statistics for Montana Validation Case Cumulus Clouds. Dark/Light Columns Depict Water Content Mean/Standard Deviation (Expressed in g/m^3). Black dots Represent Correlation Length in Seconds. Panels A Are Statistics for Observed Paths at Indicated Heights Above Cloud Base. Panels B are Statistics for Simulated Paths.

The comparison of statistics shows generally good agreement between the simulation and the observations. As expected because of the more accurate initialization, the validation simulation agrees more closely with the observations than the tuning results.

The generally short path lengths in the observations made validation of the simulated variability difficult. In general, the simulated paths' correlation lengths were much longer than those found in the observations. This is attributable, in part, to the short observational path lengths. The simulated paths' LWC standard deviations were generally very close to those found in the observations. Comparison of the observed time series and corresponding autocorrelation functions (see Figs. 34 through 37) with the simulated time series and autocorrelation functions for similar heights above cloud base shows similar features.

The mean path LWC magnitudes for the simulations were generally higher than those found in the observations for paths from 0 to 2 km above cloud base. Mean LWC values for paths 2 km and more above cloud base showed excellent agreement with the observations.

The documentation of the cloud structure provided by S&C provides an opportunity to validate the cumulus model's ability to simulate other features in addition to cloud LWC. The simulated cloud base height was located at 1.7 km MSL. This compares favorably to the cloud base height of 1.9 to 2.5 km MSL estimated by S&C from several sources. The maximum simulated cloud top height was 8.2 km MSL. This compares favorably with S&C's estimated cloud top heights of 6.0 — 9.5 km MSL. S&C's simulation produced maximum cloud top heights of 7.9 km MSL.

As a final check on the validity of the cumulus model, we compared a scene generated from the simulated cloud field with the Quick-Look visualization tool (Figure 39) to the photographs shown in S&C. The simulated scene captured the essential features of the observed cloud structure very well.

2.3.4 Conclusion

The results of the limited validation study described above show that the CSSM faithfully simulates the observed magnitude and variability of cloud LWC. Given the stochastic nature of the CSSM, the simulated LWC distributions agree quite well with those seen in the observations. The results from the parameter estimation and validation simulations show that while the model accurately captures the variability of observed LWC fields in most cases, the magnitude of the simulated LWC fields can vary significantly from that seen in the observations.

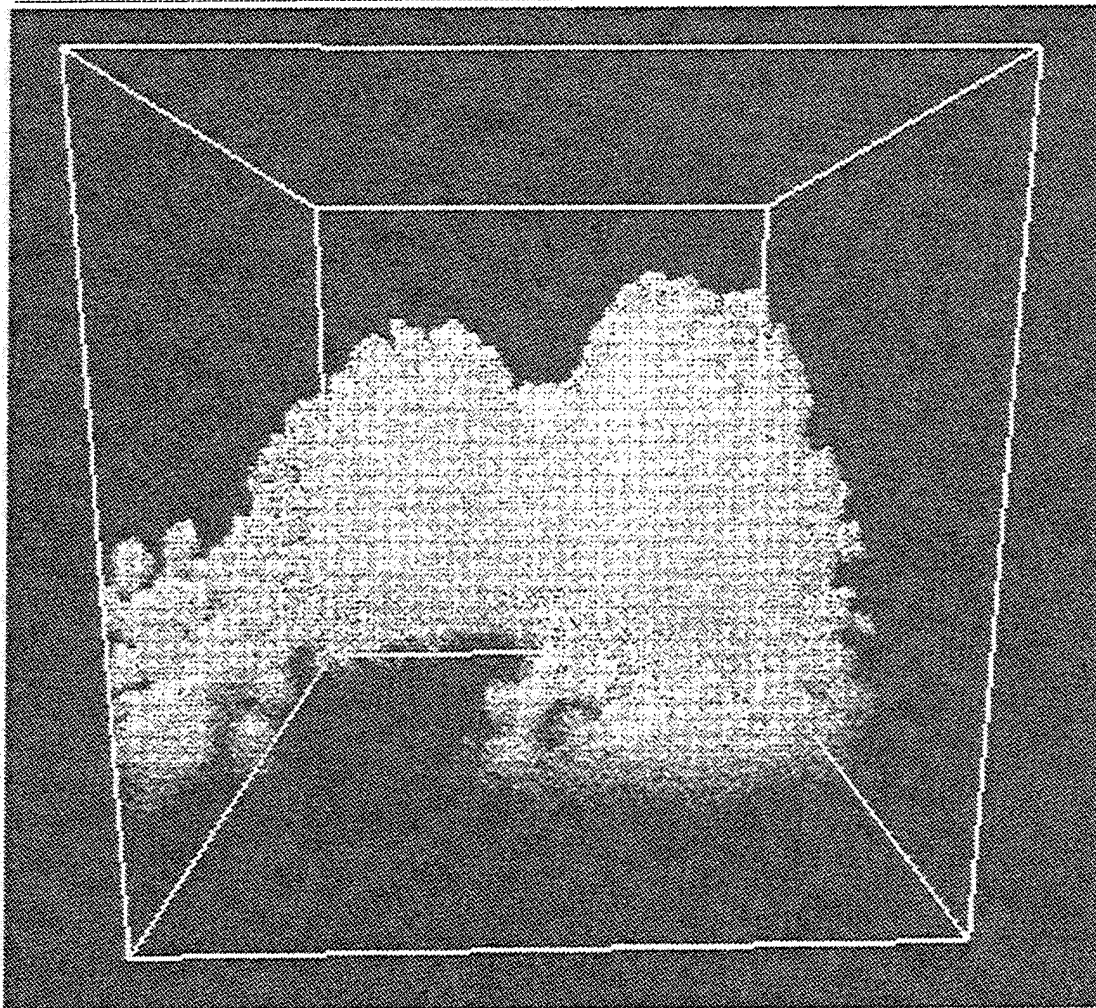


Figure 39 Validation Simulation Cloud Scene

This validation study addresses the validity of the CSSM's cloud LWC simulations. Many CSSM users are interested in the effects of clouds on radiometric sensors and weapons systems. A more effective, but difficult, validation of the CSSM would be one that compares radiometric scenes at various wavelengths generated from CSSM output with observed radiometric scenes. Such a validation would require the use of a fully-developed method to map cloud water fields to radiometric scenes (such as Fast-Map) or a full radiometric model.

3. CLOUD SCENE VISUALIZATION

3.1 QUICK-LOOK CLOUDVIEWER

The cloudviewer is a visualization tool to examine water content files generated by the CSSM. It has been developed for the Silicon Graphics Indigo family of workstations. The cloudviewer provides visualizations of cloud model output using relatively simple volume rendering techniques. The rendered cloud may be rotated, zoomed in or out, or displayed over a background image. Additionally, several rendering parameters may be adjusted. The details of selecting these features via the program's graphical user interface are described in the accompanying User's Guide (Ref. 2).

The cloudviewer uses the SGI graphics libraries to render a cloud field by randomly placing a number of small "points" within each output volume gridpoint (voxel). The resulting visualization contains a three-dimensional view of a CSSM-produced cloud field against a sky blue background, using perspective viewing geometry. The technique produces a "speckled" cloud field which can be quite realistic in appearance for some cloud types and not for others. By varying some simple parameters used in the rendering, it is possible to "fine tune" the rendering to best represent the character of the input cloud type(s).

The cloudviewer program renders typical model domains (10×10 km, 100 meter resolution) in real-time on most SGI workstations (including the standard Indy machine). For larger domains or slower CPUs, the user may have to wait for the scene to regenerate after rotating the cloud origin, zooming in or out, or modifying rendering parameters.

The maximum number of points rendered per voxel is specified by the user. The actual number of points rendered in each voxel is a function of the water content in the voxel. Likewise, the opacity of the point particles is a function of the water content in each voxel. The color, or brightness, of the points is determined using one of two shading algorithms. Both of these shading algorithms are described below.

Depth Shading

This is the simpler of the two shading algorithms. This technique determines the color of the points at each voxel based on the vertical position of the voxel within the overall cloud domain. The lowest levels of the cloud layer are darker than the highest levels.

The minimum brightness value (0–255) used in the lowest vertical levels within the cloud field is specified by the user through the graphical user interface. A default value of 200 is used to start.

The color (i.e., brightness) of each vertical level within the cloud field is given by the following:

$$\text{brightness} = (255 - \text{brightness}_{\min}) * z / \text{zlevels} + \text{brightness}_{\min}$$

where brightness_{\min} is the minimum gray level. (lower values = darker clouds)

z is the height of the voxel within the cloud domain

zlevels is the total number of z levels in the cloud domain.

The depth shading technique works best for stratiform and cirriform cloud types. Note that this algorithm simply colors the cloud levels with respect to the overall size of the input data field. Therefore, for cloud fields containing more than one layer, the bottom layer will be darker than the upper layer(s).

Gradient Shading

The gradient shading method attempts to account for surface shading effects when determining brightness within the cloud field. This method works best for cumuliform cloud types by emphasizing the curvature and bumpiness in the cloud structure.

In a first computational pass, the vector gradient of water content is computed at each gridpoint. We calculate and the central finite difference gradient in the x , y , and z directions at each voxel. A normal to the gradient vector is then computed as the “surface” normal vector. A surface normal vector is computed for every gridpoint (both on the cloud surface and inside). The brightness at each voxel is then determined using the following graphical lighting model (Ref. 25)

$$\text{Brightness} = I_a * K_a + I_p * K_d * (N \cdot L)$$

where

I_a is the ambient light intensity (or brightness)

I_p is the diffuse light intensity

K_a is the cloud ambient coefficient

K_d is the cloud diffuse reflectivity

N is the normal to the “surface” gradient at each voxel

L is the illumination vector.

The cloudviewer assumes a constant illumination vector in the cloud scene. Both K_a and K_d are set to 1.0 in the program. I_a is defined to be $\text{brightness}_{\min}/255$, so that darker scenes (those with a lower value for the minimum brightness level) have a corresponding lower ambient light intensity, and brighter scenes (those with a higher value for the minimum brightness level) have overall higher ambient lighting.

The cloudviewer allows the user to move around the cloud scene by rotating the cloud field and zooming in or out of the scene. In addition, the cloudviewer provides the tools to take snapshots of the resulting visualizations, store the snapshots and redisplay them using SGI tools. Information on how to run the cloudviewer program is detailed in Ref. 2.

3.2 "FAST-MAP" FOR WATER CLOUDS

3.2.1 Approach

The "Fast-Map" approach is a tool developed to speed the creation of visible and infrared (IR) images of 3-D water clouds, such as stratus and cumulus, by providing physics-based optical, radiative and graphical quantities for rendering. The Fast-Map approach was developed under the AMV program to provide graphical quantities for the infrared visualization of stratus clouds only. The Fast-Map Extension for Water Clouds task, funded through and performed under Contract Number F19628-91-C-0117 (see Chapter 1), added the capability to support visualization of other water clouds (such as cumulus and stratocumulus) in visible as well as IR wavelengths.

The approach is based on the conversion of water content output from the CSSM into graphical quantities such as transparency, absorptivity, and diffusivity, through a series of analytic processes. The Fast-Map approach is shown schematically in Figure 40; the steps in the figure are as follows:

- Develop a spatially variable particle size distribution, $n(r,x,y,z)$, where r is the particle radius and (x,y,z) is the location inside the cloud
- Using the $n(r,x,y,z)$ information, calculate extinction optical depth (σ) and single-scatter albedo (ω_0), including wavelength dependence
- Construct tables of radiative properties using a radiative transfer model code and parameterizations from scientific literature to map optical properties to radiative properties
- Develop the wavelength-dependent mapping between radiative properties and graphical quantities.

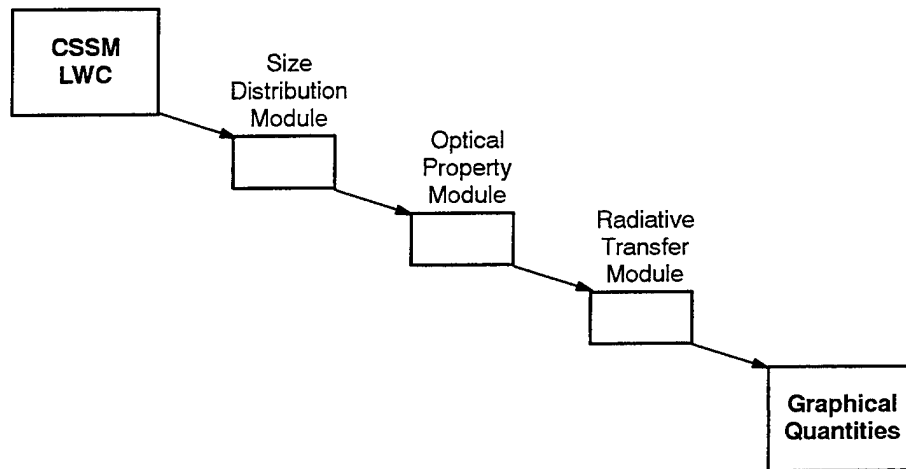


Figure 40 Schematic Representation of Data Flow through Fast-Map Driver

The approach defined by these steps is independent of cloud type; the implementation is not. The spatial variation of a typical particle size distribution must be developed for cumuliform and stratiform water clouds. Translation of water content and $n(r,x,y,z)$ into (σ, ω_0) is performed for IR and visible wavelengths and water clouds only. Parameterizations exist for broadband wavelengths for water clouds. For those cases where parameterizations are not available, they must either be developed or a scheme to minimize the number of computations devised.

The mapping of radiative properties to graphical quantities is performed for visible and infrared wavelengths. The heart of the Fast-Map approach is the construction of a database of 2-D tables relating cloud water content to cloud type, particle size, optical properties, radiative properties, and graphical quantities. Look-up tables are utilized, with links between the key entries of each table. Sample cumuliform and stratiform clouds, with derived tables of microphysical, optical, radiative, and graphical quantities were produced as deliverables.

3.2.2 Theoretical Discussion

3.2.2.1 Particle Size Distribution

Any particle size distribution can be broken into discrete size bins, as the example in Figure 41 indicates. The conversion of number density into optical properties and the derivation of radiative properties are simplified by selecting a number of narrow size bins to form a discrete representation. The number density at CSSM grid location (l,j,k) over a size range r_i to r_{i+1} is given by

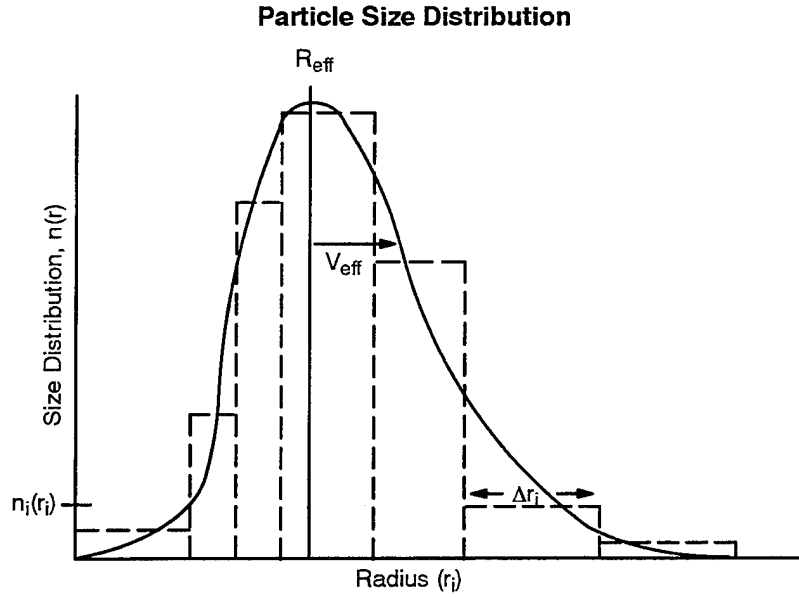


Figure 41 Typical Modified Gamma Particle Size Distribution Broken into Discrete Size Bins

$$n_i(l, j, k) = \int_{r_i}^{r_{i+1}} n(r) dr, \quad (3-1)$$

where $n(r)$ is defined by observations or an assumed size distribution. Two typical functions used to describe particle size distributions are the modified gamma distribution (as per Ref. 3),

$$n(r) = ar^\alpha e^{-br^\gamma}, \quad (3-2)$$

where a , b , α , and γ , are parameters defining the size distribution ($\gamma=1$ is typically true). By definition, $n(r) = dN/dr$ is the analytic function for the variation of number density with particle size. Nominal values for the parameters are provided in Table 22 (as per Ref. 4). The log-normal size distribution is also commonly used, e.g.

$$n(r) = \sum_{i=1}^2 \frac{N_i}{r\sigma_i \pi \ln(10) \sqrt{2}} \exp \left[-\frac{(\log r - \log r_i)^2}{2\sigma_i^2} \right], \quad (3-3)$$

where $n(r)$ is the cumulative number density of particles of radius r , N_i is the total number for the i^{th} mode, r_i is the mode radius, σ_i is the standard deviation.

The particle number density for a specific size bin can be determined once the form of the analytic function is determined (or a set of observations provided). The resultant equations for the two distributions provided have the same general mathematical form,

$$n_i(l, j, k) = C_0 \int_{r_i}^{r_i+1} r^y e^{x(r)} dr, \quad (3-4)$$

where C_0 is a constant, y is a constant (positive or negative) and $x(r)$ can have a complex form. This general mathematical expression implies a modified exponential distribution, such as the curve drawn in Figure 41. Single- and multi-modal distributions are supported by the discrete sampling approach.

Once the number density of the particles in each size bin is determined in general, we can determine the fraction of particles in any particular size bin, $f_i = n_i(l, j, k) / N(r)$. The use of f_i instead of $n_i(l, j, k)$ allows a simplified method for scaling the total number density and the number density in each bin, while retaining the functional form of the analytic expression. For the proof-of-concept Fast-Map software delivered, water clouds are assumed to have a modified gamma size distribution with parameters (a, b, α) as indicated by cloud types in Table 22).

**Table 22 Parameters for Fog and Cloud Size Distribution Models
Used in LOWTRAN & FASCODE (From Ref. 4)**

CLOUD TYPE	α	b	a	$N_0(\text{cm}^{-3})$	$\omega(\text{g-m}^{-3})$	$R_N(\mu\text{m})$	$R_M(\mu\text{m})$	$\text{Ext}^*(\text{km}^{-1}, \lambda=0.55\mu\text{m})$
Heavy Advection Fog	3	0.3	0.027	20	0.37	10.0	20.0	28.74
Moderate Radiation Fog	6	3.0	607.5	20	0.02	2.0	3.0	8.672
Cumulus	3	0.5	2.604	250	1.00	6.0	12.0	130.8
Stratus	2	0.6	27.0	250	0.29	3.33	8.33	55.18
Status/Strato- Cumulus	2	0.75	52.734	250	0.15	2.67	6.67	35.65
Alto-Stratus	5	1.111	6.268	400	0.41	4.5	7.2	91.04
Nimbo-Stratus	2	0.425	7.676	200	0.65	4.7	11.76	87.08
Cirrus	6	0.09375	2.21×10^{-12}	0.025	0.06405	64.0	96.0	1.011
Thin Cirrus	6	1.5	0.011865	0.5	3.128×10^{-4}	4.0	6.0	0.0831

*Nominal values are shown for the number density, (N_0), the liquid water (or ice) content (ω), and the visible extinction (Ext); they can be specified by the user. R_N and R_M denote the mode radii for the number and mass distribution respectively.

3.2.2.2 Spatial Variability

The spatial variation of particle size is important to accurately model the behavior of clouds in terms of physical, optical, and radiative properties. Variation of particle size with height (z) is the first-order approach we have chosen. Variation of particle size with horizontal location (x,y) will be considered at a later date.

We assume that $n(r,z) = n(r)G(z)$ is true, i.e., that the variation of the number density of the cloud particles with particle size is independent from the variation with height. This assumption is not generally true: particle size and spatial location are related. Particle size varies spatially due to entrainment and mixing processes, which produce bimodal particle size distributions near the topmost edges of stratiform clouds and the sides of cumuliform clouds. However, a reasonable first-generation approach is to ignore these effects. The separation of $n(r,z)$ leads to an expression for the fraction of particles in a size bin, $f_i = G(z)(n_i(l,j,k) / N(r))$.

The first-generation software delivered adjusts the modified gamma size distribution linearly with height above cloud base. We first assume that z is an arbitrary height above cloud base and that Δz_c is the cloud thickness. Next, we assume that the number density at the cloud top $n(z_t)$ is a linear function of the number density at cloud base, $n(z_b)$, or $n(z_t) = \epsilon n(z_b)$. Since we have already assumed that $n(r,z) = n(r)G(z)$ and we know that $n(r,0) = n(z_b)$, the mathematical expression for $G(z)$ is $G(z) = 1 + (\epsilon - 1)((z - z_b) / \Delta z_c)$.

3.2.2.3 Local Number Density

For each cloud type represented in Table 22, the particle size information is represented by statistical averages derived from observations and analysis. We assume that the relationship between local average number density and liquid water content is identical to that between the average number density and liquid water content for the cloud mass, e.g.

$$n_0(l,j,k) = \left(\frac{LWC(l,j,k)}{LWC_0} \right) N_0 = \left(\frac{LWC(l,j,k)}{\overline{LWC}} \right) \overline{N} \quad (3-5)$$

where

$LWC(l,j,k)$	= output of CSSM at grid location (l,j,k), or "local" liquid water content
\overline{LWC}	= average LWC
LWC_0	= Shettle LWC (average)
N_0	= Shettle number density (average) (see Table 22)
\overline{N}	= average number density

Note that $n_i = f_i n_0$. For each grid location (l,j,k) , the number density (n_i) in each particle size bin is derived from the local liquid water content at (l,j,k) and the average liquid water content for that cloud type, or

$$n_i = f_i LWC(l,j,k) \left(\frac{N_0}{LWC_0} \right) \quad (3-6)$$

Equation (3-6) is the algorithm implemented in the Fast-Map size distribution module. Using n_0 constrains n_i to agree with the Table 22 parameterization. Otherwise, an independent measurement of n_0 is required and validation of the relation between average number density and liquid water content must be determined. Figure 42 illustrates the use of a discretized particle size distribution to convert the water content grid into an equivalent number density grid.

A key step in the Fast-Map process is the summarization of the local number densities from a 3-D grid into a 2-D tabular form. Only the minimum and maximum number densities are recorded for each particle size bin, reducing a large number of multi-dimensional matrix information (grid-points) to fewer than 100 values. Once the 2-D number density tables are computed, the next step in the Fast-Map process is the computation of optical properties as addressed in the next sections.

3.2.2.4 Extinction Optical Depth

For each particle size bin r_i , $\sigma_{\text{scatter}_i}$ is the scattering coefficient and $\sigma_{\text{extinction}_i}$ is the extinction coefficient. Optical depth (δ_i) is related to these coefficients by the path length

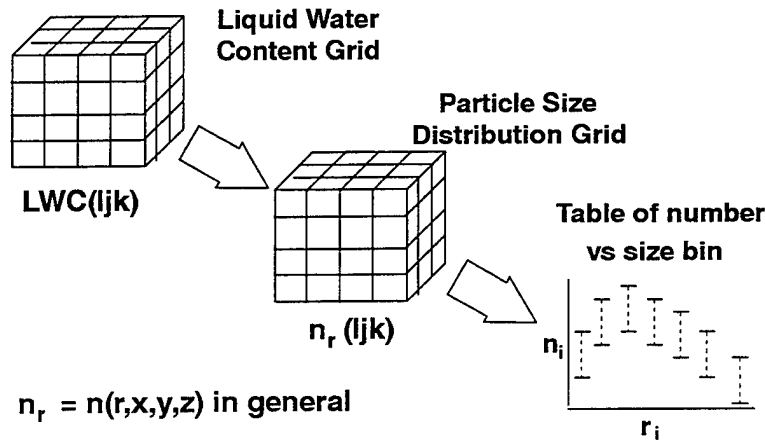


Figure 42 Translation of the 3-D Cloud Water Content Grid into a 2-D Table of Number Densities for Discrete Size Bins

through the volume of interest, ΔL_i . The expression for extinction optical depth is simply $\delta_i = \Delta L_i \sigma_{\text{extinction}_i}$. Single-scatter albedo (see next section) relates the extinction and scattering coefficients to the equivalent optical depths.

Computing extinction optical depth for each particle size bin and each local grid point is a straightforward process, particularly if the particles are uniform in size. We have used a set of look up tables computed for wavelengths between 0.25 μm and 14 μm . These look up tables were computed using a Mie code (Ref. 5) and the portion of the modified gamma distribution that falls within the fixed set of particle size bins chosen for the proof-of-concept Fast-Map code. Using the Mie code and the actual variation of particle number density provides a more accurate estimate of the extinction coefficients.

Since extinction optical depth scales linearly with number density, the minimum and maximum optical depths for each particle size bin are readily computed for each grid location. We only save the minimum and maximum values, as the extinction optical depth δ_i for size bin r_i and grid point (i,j,k) can be computed by linear interpolation.

3.2.2.5 Asymmetry Factor

The asymmetry factor (g) is defined as

$$g = \int_{-1}^1 P(\mu) d\mu \quad (3-7)$$

where $\mu = \cos\theta$, θ is the scattering angle, and $P(\mu)$ is the scattering phase function. For a set of size bins that describe a size distribution, we assume that $P(\mu) = \bar{P}(\mu)$, where

$$\bar{P}(\mu) = \frac{\int P(\mu) dr}{\int dr} \quad (3-8)$$

In the discrete form,

$$\bar{P}(\mu) = \frac{\sum_i P_i(\mu) \Delta r_i}{\sum_i \Delta r_i} \quad (3-9)$$

where $P_i(\mu)$ is the scattering phase function for particles in the size range r_i to $r_{i+1}(\Delta r_i)$. The weighting of scattering phase functions for each size range produces a weighted phase function for the entire size distribution. Use of a weighted phase function leads to the derivation of a weighted asymmetry factor, \bar{g} . Substitution gives

$$\bar{g} = \int_{-1}^{+1} \left[\frac{\sum_i P_i(\mu) \Delta r_i}{\sum_i \Delta r_i} \right] d\mu \quad (3-10)$$

Changing the order of integration gives

$$\bar{g} = \frac{\sum_i \left[\int_{-1}^{+1} P_i(\mu) d\mu \right] \Delta r_i}{\sum_i \Delta r_i}; \quad (3-11)$$

however, since $g_i = \int_{-1}^{+1} P_i(\mu) d\mu$,

$$\bar{g} = \frac{\sum_i g_i \Delta r_i}{\sum_i \Delta r_i} \quad (3-12)$$

The total weighted asymmetry factor is \bar{g} , and g_i is a constant for each particle size bin.

3.2.2.6 Single-scatter Albedo

For each particle size bin r_i , $\sigma_{\text{scatter}_i}$ is the scattering coefficient and $\sigma_{\text{extinction}_i}$ is the extinction coefficient. By definition,

$$\omega_{0i} = \frac{\sigma_{\text{scatter}_i}}{\sigma_{\text{extinction}_i}} \quad (3-13)$$

The value of ω_{0i} is independent of the number density n_i for any specific size bin. The individual single-scatter albedoes are computed in this fashion. However, the weighted single-scatter albedo for a size distribution depends on n_i . This weighting is required when a 3-D grid of ω_0 is derived from the 2-D tables to produce an output product.

The total scattering and extinction coefficients for a discrete size distribution are given by

$$\begin{aligned}\sigma_{scatter} &= \sum_i \sigma_{scatter_i} \\ \sigma_{extinction} &= \sum_i \sigma_{extinction_i}\end{aligned}\tag{3-14}$$

This leads to the size distribution weighted single-scatter albedo algorithm implemented:

$$\omega_0 = \frac{\sigma_{scatter}}{\sigma_{extinction}}\tag{3-15}$$

Using the discrete form of the equations provided in the last three sections, one can translate (n_i, r_i) into (g_i, r_i) , (ω_{0i}, r_i) and (δ_i, r_i) . Once the number density table is derived, translation into optical and radiative properties can proceed as schematically illustrated in Figure 43 since g_i and ω_i are constant for each r_i . The next section addresses the most mathematically complex portion of the Fast-Map algorithm, the derivation of radiative properties from optical properties.

3.2.2.7 Radiative Properties

The purpose of the radiative transfer (RT) module is to transform optical properties $(\omega_{0i}, g_i, \delta_i)$ into radiative properties: transmittance (τ_i), emittance (ϵ_i), reflectance (ρ_i) and absorptance (α_i). For the purposes of the proof-of-concept Fast-Map software, we treat reflectance as hemispheric reflectance, or the integral of the bi-directional reflectance function. Later versions will provide parameterizations based on scattering angles. The following subsections describe the reciprocal nature of the problem (the “trick” per se) and the implementation method.

3.2.2.7.1 Reciprocal Approach to General Problem

The problem of computing the radiative properties for a cloud volume element with given optical properties is actually an equivalence (or reciprocity) problem. Consider two volume elements with identical optical (or microphysical) properties, as shown in Figure 44.

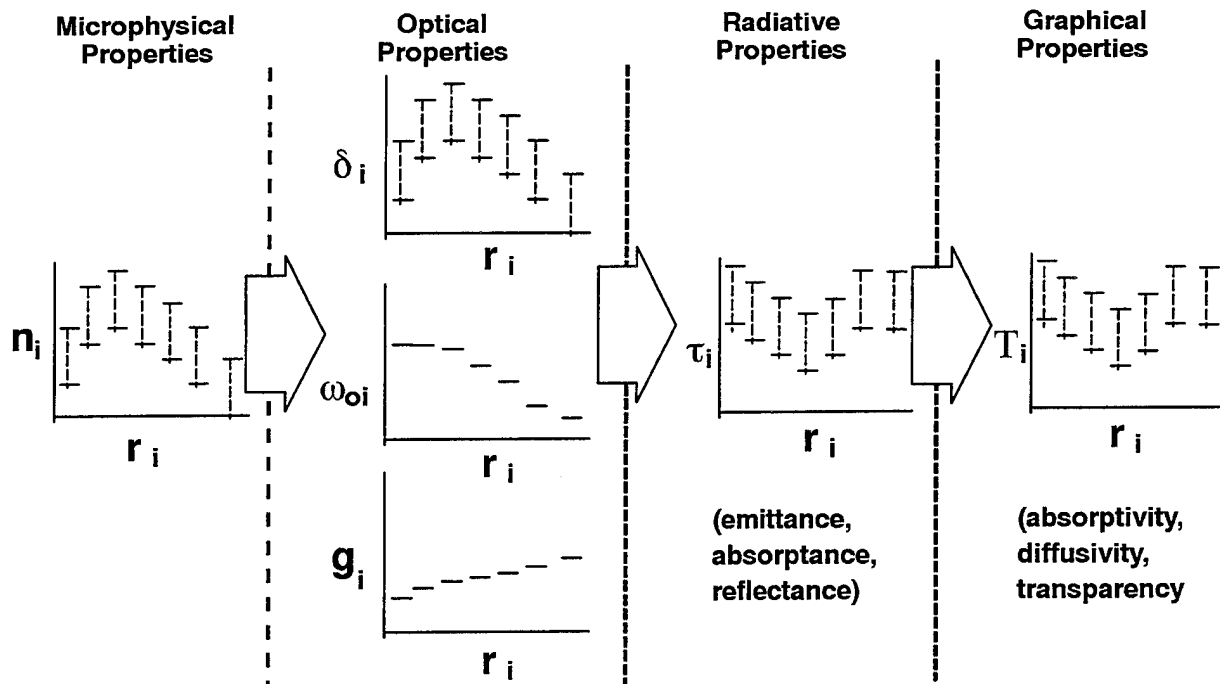


Figure 43 Transformtaion of 2-D Table of Microphysical Properties into Tables of Optical, Radiative, and Graphical Properties.

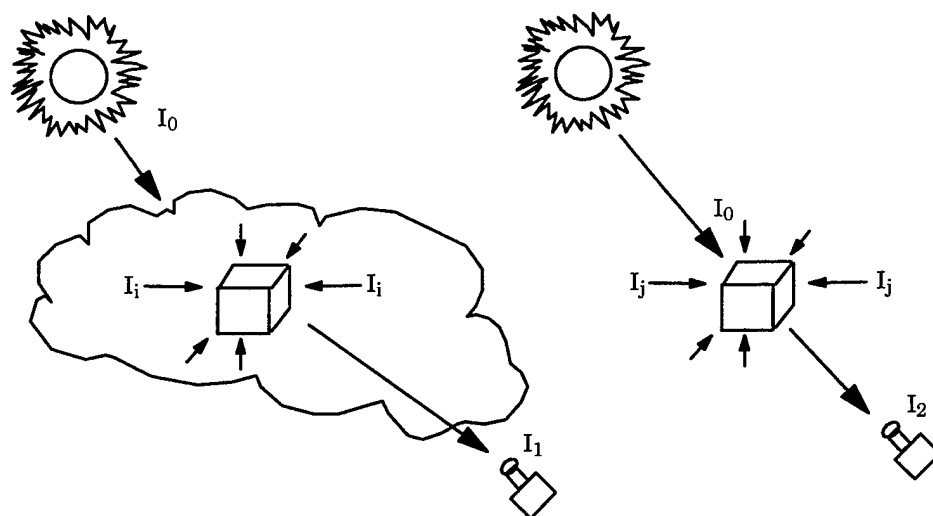


Figure 44 Radiative, Optical, and Microphysical Properties of Volumes are Identical in These Two Equivalent Scenarios. The Intensities Incident on the Volume Elements and Sensors are Different, but the $(\tau, \epsilon, \rho, \alpha)$ are the same.

The incident intensities are different in each case, as is the intensity of the radiation reaching the observer. However, the transmittance, emittance, reflectance, and absorptance of the molecules in the volume element are identical in each case. Therefore, since we can easily compute the intensities incident at the observer to determine $(\tau_i, \epsilon_i, \rho_i, \alpha_i)$ for a cloud volume element in free space, we've solved the problem of a volume element inside a cloud by reciprocity.

3.2.2.7.2 Implementation

There are three optional implementations built into concept of the Fast-Map radiative transfer module. These options, as listed in order of increasing rigor and complexity, are:

1. a parametric method, where $(g_i, \omega_{0i}, \delta_i) \rightarrow (\tau_i, \epsilon_i, \rho_i, \alpha_i)$ is determined by empirical means.
2. the use of look up tables with $(g_i, \omega_{0i}, \delta_i)$ as indices. Tables of $(\tau_i, \epsilon_i, \rho_i, \alpha_i)$ are pre-computed for a broad set of conditions and interpolation methods used to determine the local grid values.
3. the option to call a 1-, 2- or 3-D radiative transfer model and return values of $(\tau_i, \epsilon_i, \rho_i, \alpha_i)$ for the conditions specific to the scene.

All three cases presume that a set of wavelength-dependent values can be computed for each minimum and maximum of the input optical properties tables (recall that g_i and ω_{0i} are constant for each size bin, only δ_i varies).

Due to a lack of adequate parameterizations, the first method was omitted in the first-generation Fast-Map software. The modular nature of the code allowed for software "hooks" to be left in place to support this approach at a later date. The third, or most complex, solution was not implemented as this is the slowest method. The third method will provide the most rigor to the derivation of the radiative properties; however, radiative transfer computations are notorious for their computationally intensive nature. This method should be explored at a later date, particularly the 3-D application for finite cloud objects.

We note that radiative transfer modeling and property interpolation for discrete scattering angles (ϕ, θ) and cloud temperatures is complex. There is a distinct need for trade-off studies and parameterizations.

Consequently, the second method was used for the prototype Fast-Map software delivered. Look up tables were generated for a range of optical properties, using optical depth and single scatter albedo to index variations in transmittance, reflectance, absorptance and emittance.

Due to resource constraints, several simplifying assumptions were made that enabled the software to be completed and still provide a reasonable degree of accuracy. The first assumption was that Kirchoff's relation is valid for the infrared (11 μm) wavelengths considered and that the emittance in the visible was zero. Second, we decided that the calculations would be monochromatic.

Based on the monochromatic assumption, we used the Beer-Lambert relation to relate extinction optical depth to transmittance at the wavelengths considered, e.g. $\tau_i = e^{-\delta_i}$. This is a valid expression for all wavelengths in the spectral regimes of interest. Two wavelength options were provided with the prototype software: a visible wavelength (0.55 μm) and an infrared wavelength (11 μm). These two wavelengths provide a comparison between a cloud object that is almost perfectly scattering ($\omega_0 \cong 1$) and one that is primarily absorbing (ω_0 small). These bounding cases provide a relatively simple means to test and validate the mapping process.

The final step in the computation of the radiative properties in the prototype software is based on conservation of energy. For visible wavelengths, $\rho_i + \tau_i = 1$ when there is no absorptance. Similarly, for infrared wavelengths, $\alpha_i + \tau_i = 1$ when there is no reflectance. This leads to two simple relations for the visible reflectance and the infrared absorptance. Since the cloud single-scatter albedo is not exactly equal to one in the visible, and cloud particles do have a secondary reflectance in the infrared, we have added a simple, scalar parameter ($\eta = \alpha$ or ρ) that specifies these values. Consequently, for visible and infrared wavelengths $\rho_i + \tau_i + \alpha_i = 1$ results. Note that for monochromatic calculations, this is a general result.

3.2.2.7.3 Radiative Property Weighting

Once a 2-D table of radiative properties is obtained, then translation of $(g_i, \omega_{0i}, \delta_i)$ and $(\tau_i, \epsilon_i, \rho_i, \alpha_i)$ for each size bin r_i becomes a matter of correctly scaling the interpolation of the optical and radiative properties. This scaling is indicated schematically in Figure 45.

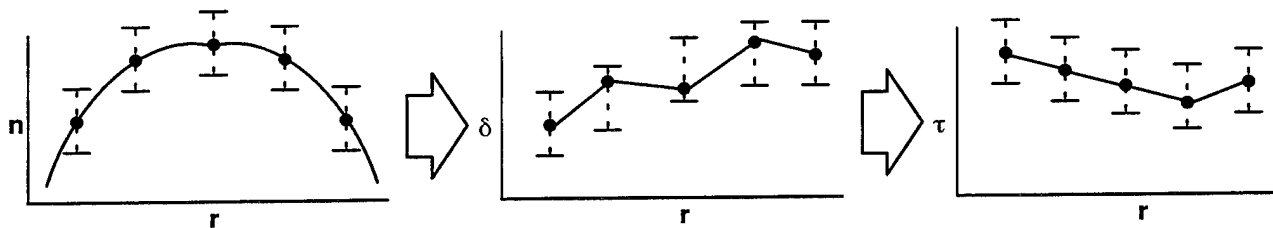


Figure 45 Translation of Number of Density to Optical Depth and Transmittance Through a Particle Size Dependent Interpolation.

Figure 46 indicates the reconstruction process, where weighting of the radiative properties must occur to reconstruct the 3-D grid.

Several steps must be followed to produce weighted output quantities:

1. Compute transmittance, $\tau(l,j,k) = \prod_i \tau_i(l,j,k)$
2. Derive reflectance and absorptance, e.g.,
 - $\rho(l,j,k) = 1 - \prod_i [1 - \rho_i(l,j,k)]$ for the visible
 - $\alpha(l,j,k) = 1 - \prod_i [1 - \alpha_i(l,j,k)]$ for the infrared
3. Emittance is given by $\varepsilon = \alpha$, e.g., Kirchoff's relation is assumed for the IR.

All of these values are optional products of the Fast-Map software, selected by the user.

3.2.2.8 Graphical Quantities

Translation or mapping of radiative properties to graphical quantities is the final step in the Fast-Map process. The normal graphical quantities used by computer image generators expresses the properties of nodes (nodes sum to pixels) in terms of three quantities. One set of these properties is transparency (T), absorptivity (A) and diffusivity (D). The most significant part of the problem is how one maps four radiative properties into three graphical quantities.

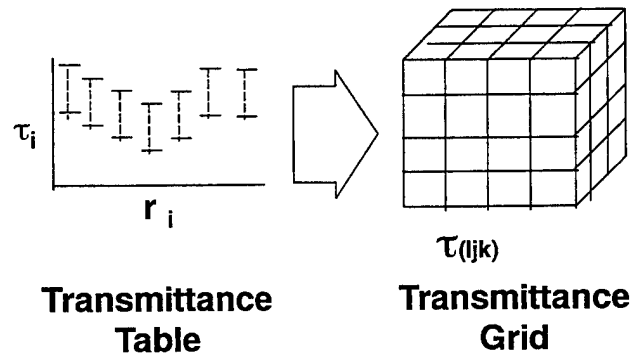


Figure 46 3-D Grid Reconstruction from 2-D Table

The translation of $(\tau_i, \epsilon_i, \rho_i, \alpha_i)$ to (T_i, A_i, D_i) has a complex wavelength dependence. As the following list indicates, transmittance is the easiest radiative property to map, while emittance, reflectance and absorptance have a more complex mapping:

1. Simplest: $T_i = \tau_i$, there is no wavelength dependence
2. Harder: $(\epsilon_i, \rho_i, \alpha_i) \rightarrow (\epsilon_i, \rho_i) \rightarrow (A_i, D_i)$ (infrared) and
3. Hardest: $(\epsilon_i, \rho_i, \alpha_i) \rightarrow (A_i, D_i)$ (Near-IR)

Once the mapping is computed for a given set of wavelengths, it can be applied repetitively without further computational overhead. We have utilized the visible and infrared mapping in the prototype Fast-Map software.

In general, the mapping of $(\tau_i, \epsilon_i, \rho_i, \alpha_i)$ to (T_i, A_i, D_i) will be via polynomial approximations such as

$$(A, D) = f(\epsilon) + g(\rho) + h(\alpha)$$

$$\begin{aligned} \text{where } f(\epsilon) &= a_0 + a_1\epsilon + a_2\epsilon^2 \\ g(\rho) &= b_0 + b_1\rho + b_2\rho^2 \\ h(\alpha) &= c_0 + c_1\alpha + c_2\alpha^2 \end{aligned}$$

The (a_i, b_i, c_i) matrix will have a wavelength dependence, but will be constant for a given set of hardware and software. This is an important consideration as (T, A, D) could be expressed as values between 0–1 or 0–255. The form of (T, A, D) depends on whether the values are meant to represent color, saturation and hue, or other equivalents to transparency, absorptivity and diffusivity. This is a problem based in the addition versus subtraction method of color reproduction. Neither is more correct than the other; they are simply equivalent methods. Consequently, (T, A, D) can have several forms, some additive and others not.

For the purposes of the prototype software, we have mapped 2-D tables of radiative properties into 2-D tables of graphical quantities with values between 0–1. The final step is the reconstruction of the 3-D grid of graphical quantities as output products of the software. We map the atomic radiative properties to their equivalent atomic graphical quantities, then we weight the graphical quantities in a similar manner to the radiative property weighting described in Section 3.2.2.7.2.

The weighted graphical quantities are determined in the following fashion:

For the visible,

1. transparency is $T(l,j,k) = \prod_i T_i(l,j,k)$
2. absorptivity is $A(l,j,k) = [1 - \prod_i \{1 - \rho(i,j,k)\}] \cdot \eta$
3. diffusivity is $D(l,j,k) = [1 - \prod_i \{1 - \rho(i,j,k)\}] \cdot (1 - \eta)$,

where η is the scalar absorptance (see Section 3.2.2.7.2) and i indicates size bin.

For the infrared,

1. transparency is $T(l,j,k) = \prod_i T_i(l,j,k)$
2. absorptivity is $A(l,j,k) = [1 - \prod_i \{1 - \rho(i,j,k)\}] \cdot (1 - \eta)$
3. diffusivity is $D(l,j,k) = [1 - \prod_i \{1 - \rho(i,j,k)\}]$,

where η is the scalar reflectance (see Section 3.2.2.7.2) and i indicates size bin.

For the infrared, diffusivity is equivalent to the sum of the emittance and the reflectance. For the visible, diffusivity is equivalent to the hemispheric reflectance. For all wavelengths, the diffusivity term is the most difficult to map. This term contains the specular and diffuse components of the bi-directional reflectances and the thermal structure that specifies the amount of Planck radiation emitted. Future developments of Fast-Map will, by necessity, address these problems.

3.2.3 Summary

Generation of radiometric images occurs by means of some rendering engine or scene generation tool. These applications position illuminating light sources and background objects in place, then interpolate 3-D grids of optical or radiative properties to derive (T,A,D). Ray-tracing through the volume from back to front is the final step in this process. These steps are typically slow due to the use of software, not hardware, to perform the integration. Short-cuts are often used to speed up the time required to render scenes, particularly for real-time applications that operate with ten or more images per second. However, these short-cuts usually require one to disregard some of the physical relationships.

Fast-Map is not designed to generate or render scenes. Instead, it is designed to produce a 3-D grid of graphical quantities (T,A,D) based on the physics of clouds, removing that burden from the software used by a rendering engine. Consequently, by using the graphical information the computer image generator will only have to perform the ray-tracing step. This step is fast, so the time required to render the scene should dramatically decrease. We hope that with further development and improvement in the hardware and software, the Fast-Map application will prove to add significant value to the visualization of atmospheric scenes, particularly those that contain clouds.

3.2.4 Future Work

A number of future efforts have been cited in the previous sections that address a variety of topics. These topics include:

- deriving parameters to define the wavelength dependent mapping of radiative to graphical quantities
- developing radiative transfer parameterizations for wavebands of interest
- developing the description of reflectance to include specular and bi-directional components, defined in terms of the scattering angle
- converting the particle size distribution — wavelength approach for a more general effective size parameter approach (more elegant and powerful)
- extending the Fast-Map prototype to include fog and rain
- extending the Fast-Map prototype to include nonspherical particles, thus allowing rapid, physics-based visualization of cirrus clouds
- implementing the 1-, 2- and 3-D radiative transfer module to determine the trade-off between a full, rigorous solution and rapid visualization
- validating the microphysical, optical and radiative properties computed for typical scenes with actual measurements to bound the accuracy of the method and tune the algorithms
- extending the particle size distribution module to allow user selection of particle size bins, to allow input of actual particle size measurements, and to provide a more sophisticated mechanism for the spatial variation of particle size with location inside the cloud mass (including entrainment and multi-modal distributions)
- supporting sub- and super-sets of the output products to allow consistent representation of the cloud objects at multiple levels of detail (multi-fidelity clouds), of particular interest in battlefield visualization
- to extend the visualization concept to include Fast-Map and a hardware/software package to perform accurate, physics-based scene generation.

These are a variety of topics which all have merit in the development and application of the next-generation Fast-Map software.

Summary

The Cloud Scene Simulation Model, developed with the support of the U.S. Air Force Phillips Laboratory, the Defense Modeling and Simulation Office and the U.S. Army Topographic Engineering Center under the Dynamic Environment and Terrain Modeling in DIS Program, is an efficient and portable tool to generate multi-layer cloud scenes containing stratiform, cirriform, and cumuliform cloud types. Cloud scenes consist of three-dimensional water content and rain rate fields that can be used to characterize the natural atmospheric environment for visualization, sensor test and evaluation, and a host of other simulation applications.

This report describes the science within the CSSM, and outlines the primary procedures called upon to synthesize a high-resolution cloud scene from general atmospheric conditions provided by the user. We have focused on the recent enhancements to the model including a movable output domain, gridded input conditions, terrain-induced wave clouds, stratocumulus cloud streets, interoperable output fields, longer simulation domains, larger simulation domains, etc.

In addition to a discussion of the model, we show some output scenes created with the quick-look cloudviewer tool, developed under this research effort. This tool renders a cloud field as a series of points, where the number and opacity of the points is based on the water content, and the color (or brightness) of the points is based on a shading algorithm. This interactive tool allows the model developer and/or user an opportunity to view the three-dimensional model output in on any of the SGI Indigo family of workstations.

The Fast-Map post-processor is also described. The Fast-Map processor provides the means to generate the graphical quantities needed to rapidly render physics-based visible and infrared images of 3-D water clouds, such as stratus and cumulus clouds. The Fast-Map approach rapidly converts water content values from the CSSM into optical properties, radiative properties, and finally graphical quantities, such as transparency, absorptivity, and diffusivity.

Also included in this report are the results from our analysis effort to extract best estimates for internal model parameters from cloud observations. A description of the water content observations, the parameter estimation process, and a preliminary validation

case are included. Cumulus and stratus cloud types were analyzed under this effort and our results show good agreement between model-produced and observed water content fields. However, more analysis needs to be performed to estimate parameters for all other cloud types and continue to validate the model. Recommendations for continued analysis along with other future model development and research areas are discussed in the following section.

Recommendations

As with the previous version of the CSSM, we have emphasized a modular software design that not only accommodates the maintenance of the code, but also allows for future growth. Below we list a few recommendations for continued validation of CSSM output and suggestions for enhancements and growth.

Develop Enhanced Cirrus Model

The CSSM currently uses a strictly parametric cirrus model. Horizontal cloud distribution and cloud bases and tops are determined by the Rescale and Add algorithm and water content is distributed parametrically between base and top surfaces.

We recommend the incorporation of a more sophisticated cirrus model to address the microphysics and possibly dynamics of cirrus. This effort should include the following steps:

- Evaluate and select new cirrus model compatible with existing architecture
- New model will likely include cirrus generating cells, particle size distributions, and advection and cascade processes
- Tuning and validation commensurate with data availability.

Develop Climatological Preprocessor

The CSSM is currently initialized with input from either a single point meteorological profile and cloud information or gridded data numerical weather prediction model output and gridded cloud information. This input method is cumbersome for users requiring cloud scenes consistent with climatological conditions for a specified location and time. We recommend the development of a preprocessor that will automatically derive CSSM meteorological profile and cloud input information from readily-available climatological databases using input provided through a graphical user interface (GUI). Potential uses for such a capability include simulations, mission planning and rehearsal, and weapons system testing.

Develop CSSM Preprocessor

The current implementation of the CSSM provides a limited capability to ingest gridded terrain information and output from numerical weather prediction models. The model also provides a capability to ingest gridded cloud information. The manipulation of these input files and the generation of the cloud input files is cumbersome and manually intensive. We recommend the development of an automatic preprocessor that consists of four parts:

- Cloud analysis interface to ingest RTNEPH and SERCAA cloud analyses and selected other cloud analyses
- Automated single-sounding analysis to infer cloud base, top and height information from single input soundings
- Terrain database interface to enhance current terrain ingest capability
- Gridded environmental data interface module to easily ingest NORAPS, Air Force Theater Forecast Model and other NWP output into the CSSM.

Develop Fog Model

The current CSSM implementation does not support fog. We recommend the development of a stochastic fog model based on data reported in the literature.

Develop Enhanced Rain Model

The currently implemented rain model provides a very limited capability to simulate precipitation. The current model does not include several important processes:

- The ability for in-cloud precipitation rates to be physically converted into actual precipitation at the surface
- Microphysical processes that affect cloud droplets, such as scavenging, evaporation, and growth
- The effects of advection on the trajectory of the rain shaft as the cloud and precipitable water contents evolve spatially and temporally
- Definition of realistic moisture fluxes to support rainfall of limited duration for a fixed geographic region.

We recommend the development, implementation, and validation of an enhanced rain model that corrects or at least mitigates the weaknesses described above. This effort should attempt to:

- Employ size distribution models to derive autoconversion rates from cloud water to rain water for stratiform and cumuliiform clouds
- Review and implement parametric scavenging and evaporation models for stratiform and cumuliiform clouds

- Expand development of cascade model to allow the use of movable domains and to include advection processes, e.g. the effects on parcel rainrates and rain shaft trajectory
- Evaluate the amount of atmospheric moisture available to support rain rates and precipitation with time
- Compare statistics of model-produced rain amounts to those of observed data.

Radiometric Scene Validation of CSSM Output

The current effort focused on validation of CSSM output through comparisons of model-generated liquid water content paths with those observed by aircraft. While this approach provides a useful measure of the model's validity, it does not address most customers' root concern: Does the CSSM generate cloud scenes in various wavelengths consistent with those observed in nature?

To address this issue we recommend the validation of the CSSM output by comparing 2D radiometric scenes rendered from model output with a radiative transfer model with observed radiometric scenes. This is a large and complicated task that dwarfs the validation effort performed in the current effort. Such an effort would require the use of extensive radiometric scene datasets complemented by coincident meteorological information. Additionally, the effort will require the use of a radiative transfer model or an enhanced version of the Fast-Map tool to produce radiometric scenes from the CSSM output.

Fast-Map Enhancements

The Fast-Map processor developed during this effort was intended as a proof-of-concept. As such, its usefulness in its present form is limited. We believe the approach has great potential to rapidly provide the graphical quantities needed for real-time cloud scene visualization. We recommend enhancing the Fast-Map processor as described in detail in the previous section.

REFERENCES

1. Cianciolo, M.E., and R.G. Rasmussen, Cloud Scene Simulation Modeling – The Enhanced Model, Technical Report, PL-TR-92-2106, April 1992, ADA265958.
2. Cianciolo, M.E., and M.E. Raffensberger, The Cloud Scene Simulation Model – User's Guide, Technical Memorandum, TIM-7169-2, April 1996.
3. Raffensberger, M.E., and E.O. Schmidt, The Fast-Map Processor – User's Guide, Technical Memorandum, TIM-7169-3, April 1996.
4. Saupe, D., 1989: Point Evaluation of Multi-Variable Random Fractals, *Visualisierung in Mathematik and Naturwissenschaft*, H. Jurgens and D. Saupe, Eds., Springer-Verlag, Heidelberg.
5. Lovejoy, S., 1982: Area-Perimeter Relation for Rain and Cloud Areas, *Science*, 216, 185–187.
6. Cahalan, R.F., and J.H. Joseph, 1989: Fractal Statistics of Cloud Fields, *Monthly Weather Review*, 117, 261–272.
7. Cahalan, R.F., 1991: Landsat Observations of Fractal Cloud Structure in Non-Linear Variability in Geophysics, D. Schertzer and S. Lovejoy, Eds., pp. 281–295.
8. Press, W.H., et al., 1988: *Numerical Recipes in C – The Art of Scientific Computing*, Cambridge University Press, pp. 171–176.
9. Feddes, R.G., 1974: A Synoptic-Scale Model for Simulating Condensed Atmospheric Moisture, USAFETAC-TN-74-4.
10. Fleagle, R.G., and J.A. Businger, 1980: An Introduction to Atmospheric Physics, 2nd Ed., *International Geophysics Series*, Vol. 25, pp. 75–76.
11. Feteris, P. J., A.S. Lisa, C.J. Bowley, M.G. Fowler, and J.C. Barnes, 1976: Investigation of Mesoscale Cloud Features Viewed by LANDSAT, Final Technical Report, January 1975 – January 1976, Contract NAS5-20804, Environmental Research & Technology, Inc., Concord MA, 111 pp.
12. Kuettner, J. P., 1959: The Band Structure of the Atmosphere, *Tellus*, 11, No. 3, pp. 267–294.
13. Tattelman, P., and P.T. Willis, 1985: Model vertical profiles of extreme rainfall rate, liquid water content, and drop-size distribution, AFGL-TR-85-0200, 34 pp., ADA164424.
14. Mueller, E.A., and A. L. Sims, 1967: Raindrop Distributions at Island Beach, New Jersey. Illinois State Water Survey, ECOM-02071-RR2, 108 pp.
15. Mueller, E.A., and A.L. Sims, 1967: Raindrop Distributions at Franklin, North Carolina. Illinois State Water Survey, ECOM-02071-RR3, 157pp.

16. Mueller, E.A., and A.L. Sims, 1967: Raindrop Distributions at Woody Island, Alaska. Illinois State Water Survey, ECOM-02071-4, 93pp.
17. Mueller, E.A., 1962: Raindrop Distributions at Miami, Florida. Illinois State Water Survey, Research Report No. 9B, 281 pp.
18. Seliga, T.A., K. Aydin, and H. Direskeneli, 1986: Disdrometer Measurements during an Intense Rainfall Event in Central Illinois: Implications for Differential Reflectivity Radar Observations. *Journal of Climate and Applied Meteorology*, 25: 835-846.
19. Heymsfield, A.J., 1977: Precipitation Development in Stratiform Ice Clouds: A Microphysical and Dynamical Study. *J. Atmos. Sci.*, 34: 367-381.
20. Marshall, J.S., and M.W. Palmer, 1948: Relation of raindrop size to intensity. *J. Meteor.*, 5, 165-166.
21. Knight, C.A., W.D. Hall, and P.M. Roskowski, 1983: Visual cloud histories related to first radar echo formation in northeast Colorado cumulus, *J. Cli App. Met.*, 22, 1022-1040.
22. Kummerow, C., I.M. Hakkarinen, H.F. Pierce, and J.A. Weinman, 1991: Determination of Precipitation profiles from airborne passive microwave radiometric measurements, *J. Atmos. Ocn. Tech.*, 8, 148-158.
23. Hauser, D., and P. Amayenc, 1983: Exponential size distributions of raindrops and vertical air motions deduced from vertically pointing doppler radar data using a new method, *J. Cli. App. Met.*, 22, 407-418.
24. Smolarkiewicz, P.K., and T.L. Clark, Numerical Simulation of the Evolution of a Three-Dimensional Field of Cumulus Clouds. Part I: Model Description, Comparison with Observations and Sensitivity Studies, *J. Atmos. Res.*, 42, 502-522.
25. Foley, J.D., and A. Van Dam, *Fundamentals of Interactive Computer Graphics*, Addison-Wesley, Inc., 1982.
26. Hansen, J.E., and L.D. Travis, 1974: Light Scattering in Planetary Atmospheres, *Space Sci. Rev.*, 16, 527-610.
27. Shettle, E.P., 1989: Models of Aerosols, Clouds and Precipitation for Atmospheric Propagation Studies, *Proceedings of the AGARD 45th Symposium of the Electromagnetic Wave Propagation Panel on Atmospheric Propagation in the UV, IR, and mm-Wave Region and Related Systems Aspects*, Copenhagen, Denmark, 9-13 October, 1989.
28. Wiscombe, W.J., 1979: Mie Scattering Calculations: Advances in technique and fast, vector-speed computer codes, NCAR/TN-140 + STR, National Center for Atmospheric Research, Boulder, Colorado.